Assembly and phospho-regulatory mechanisms of the budding yeast outer kinetochore KMN complex

Noah N. Turner[1,2,3], Ziguo Zhang[1], Jing Yang[1], Kyle W. Muir[1,2], Stephen H. McLaughlin[1], Tomos Morgan[1] and David Barford[1,3]

[1]MRC Laboratory of Molecular Biology, Francis Crick Avenue, Cambridge, CB2 0QH, UK.

[2]Present address: Noah N. Turner: John Innes Centre, Norwich, UK; Kyle W. Muir: Institute of Cell Biology, University of Edinburgh, Edinburgh, EH9 3BF, UK.

[3]Corresponding authors: noah.turner@jic.ac.uk, dbarford@mrc-lmb.cam.ac.uk

Running title: Cryo-EM structure of the budding yeast KMN complex

40 word summary: Kinetochore-localised KMN complexes mediate chromosome segregation by attaching chromosomes to spindle microtubules. Cryo-EM, biochemical and genetic experiments reveal conserved underlying mechanisms of complex assembly, auto-inhibition and phospho-regulation that ensure precise control of KMN assembly onto centromeres to enable genome division.

Abstract

During mitosis and meiosis kinetochores mediate interactions between chromosomes and spindle microtubules. Kinetochores are multi-megadalton protein complexes essential for chromosome segregation in all eukaryotes, however recent structural, functional, and evolutionary studies have revealed divergent mechanisms of kinetochore assembly. In this study, we use cryo-EM to understand the structural mechanisms by which the budding yeast microtubule-binding outer kinetochore KMN complex assembles, and how its interactions with the centromere-binding inner kinetochore are regulated. The ten-subunit KMN complex comprises three subcomplexes: Knl1c, Mis12c^{Mtw1c} and Ndc80c. We show that α-helical motifs in the C-termini of the Mis12c^{Mtw1c} subunits Dsn1, Mis12^{Mtw1} and Nnf1 bind Knl1c and Ndc80c. At the opposite end of the Mis12c^{Mtw1c} stalk, an N-terminal auto-inhibitory segment of Dsn1 (Dsn1^{AI}) folds into two α-helices that engage the Mis12c^{Mtw1c} head 1 domain, thereby occluding binding sites for the inner kinetochore subunits CENP-C^{Mif2} and CENP-U^{Ame1}, reducing their affinity for Mis12c^{Mtw1}. Our structure reveals how Aurora B^{Ipl1}

phosphorylation of Dsn1^{AI} would release this auto-inhibition to substantially strengthen pre-existing connections between the inner and outer kinetochore.

Introduction

Kinetochores are large nucleoprotein complexes that mediate faithful chromosome segregation during cell division (Ariyoshi and Fukagawa, 2023; McAinsh and Marston, 2022; Musacchio and Desai, 2017). Kinetochores assemble at centromeres to create an essential load-bearing linkage between chromosomes and microtubules of the mitotic spindle (Akiyoshi et al., 2010; Lang et al., 2018). The point centromeres of budding yeast *Saccharomyces cerevisiae* comprise genetically defined ~118 bp *CEN* sequences with three centromere DNA elements (CDEI to III) (Clarke and Carbon, 1980; Clarke and Carbon, 1983; Fitzgerald-Hayes et al., 1982; Hyman and Sorger, 1995). The *CEN* sequence and CENP-A^{Cse4} nucleosome provide a foundation upon which the rest of the kinetochore assembles (Lang et al., 2018). The CENP-C^{Mif2} protein mediates specific interactions between the CENP-A nucleosome and the inner kinetochore constitutive centromere associated network (CCAN) complex, and also interacts with the outer kinetochore KMN complex (Ariyoshi et al., 2021; Dimitrova et al., 2016; Hornung et al., 2014; Kato et al., 2013; Przewloka et al., 2011; Screpanti et al., 2011; Xiao et al., 2017; Yan et al., 2019). CCAN complexes entrap centromeric DNA within topological chambers (Dendooven et al., 2023; Yatskevich et al., 2022).

The KMN complex bridges the inner kinetochore with the microtubule (Cheeseman et al., 2006; Deluca et al., 2006). Mis12c/Mis12c^{Mtw1c} (human/budding yeast) interacts with Knl1c and Ndc80c to assemble the KMN complex (Figures 1A and S1A) and mediates recruitment of the entire complex to kinetochores (Dimitrova et al., 2016; Ghodgaonkar-Steger et al., 2020; Petrovic et al., 2014; Petrovic et al., 2010; Polley et al., 2024; Yatskevich et al., 2024). Ndc80c also associates with CENP-T independently of Mis12c^{Mtw1c} and Knl1c (Malvezzi et al., 2013; Nishino et al., 2013). Mis12c engages Knl1c and Ndc80c at the apex of a central α-helical stalk (Petrovic et al., 2014). The base of the stalk bifurcates to form the head 1 and head 2 domains that mediate interactions with the inner kinetochore (Akiyoshi et al., 2013; Dimitrova et al., 2016; Emanuele et al., 2008; Kim and Yu, 2015; Petrovic et al., 2016; Rago et al., 2015; Walstein et al., 2021). Head 1 interacts with N-terminal motifs of CENP-C^{Mif2} and CENP-U^{Ame1} in budding yeast, and CENP-C^{Mif2} and CENP-T in vertebrates (Dimitrova et al., 2016; Hornung et al., 2014; Huis In 'T Veld et al., 2016; Killinger et al., 2020; Petrovic

et al., 2016). The mutually exclusive binding of inner kinetochore subunits to Mis12c^{Mtw1c} (Huis In 'T Veld et al., 2016; Killinger et al., 2020) recruits multiple copies of KMN to the inner kinetochore (Cieslinski et al., 2023; Dhatchinamoorthy et al., 2017; Joglekar et al., 2006; Johnston et al., 2010). These interactions are auto-inhibited by a region within the intrinsically disordered N-terminus of the Mis12c^{Mtw1c} subunit Dsn1 in a manner that is relieved by Aurora B^{Ipl1} phosphorylation at mitotic kinetochores (Dimitrova et al., 2016; Petrovic et al., 2016; Polley et al., 2024; Takenoshita et al., 2024; Walstein et al., 2021; Yatskevich et al., 2024).

Ndc80c interacts with microtubules through N-terminal domains of its constituent Ndc80 and Nuf2 subunits (Alushin et al., 2012; Alushin et al., 2010; Ciferri et al., 2008; Lampert et al., 2013; Muir et al., 2023; Wei et al., 2007), augmented through interactions with the unrelated Astrin/SKAP and Ska complexes in human and the Dam1 complex in budding yeast (Helgeson et al., 2018; Huis In 'T Veld et al., 2019; Kern et al., 2017; Lampert et al., 2010; Muir et al., 2023; Tien et al., 2010; Van Hooff et al., 2017). The Ndc80 and Nuf2 microtubule-binding calponin homology (CH) domains are at the opposite end of the 570 Å-long Ndc80 complex to RWD domains in the C-termini of the Spc24 and Spc25 subunits (Spc24^{RWD}:Spc25^{RWD}) that interact with Mis12c^{Mtw1c} (Wang et al., 2008; Wei et al., 2006; Wei et al., 2005). The long Ndc80c is formed by the end on interactions of the Ndc80:Nuf2 and Spc24:Spc25 coiled-coils (Ciferri et al., 2005; Valverde et al., 2016). Kinetochore-associated Knl1c contributes to spindle assembly checkpoint (SAC) and error correction (EC) signalling, reviewed in (Fischer, 2023; McAinsh and Kops, 2023).

Although the general mechanisms of KMN complex assembly and regulation are conserved from budding yeast to human, specific details of how Mis12c^{Mtw1c} interacts with both Ndc80c and Knl1c differ (Figure 1F, G). The Spc24:Spc25 RWD domains of Ndc80c interact with α-helical motifs in C-terminal extensions of the rod-like stalk domain of human Mis12c and budding yeast Mis12c^{Mtw1c}. These include a conserved C-terminal α-helix in the Dsn1 subunit (Dimitrova et al., 2016; Polley et al., 2024; Yatskevich et al., 2024), and, additionally in humans, an α-helix in the Mis12c subunit Nsl1 (Polley et al., 2024; Yatskevich et al., 2024). No equivalent motif exists in budding yeast Nsl1 (Dimitrova et al., 2016). Instead, an α-helix in the budding yeast Mis12^{Mtw1} binds to the Spc24 and Spc25 RWD domains cooperatively with the Dsn1 α-helix (Ghodgaonkar-Steger et al., 2020). In humans, motifs at the C-terminus of Nsl1 mediate binding of Mis12c to the tandem RWD domains of the

human Knl1c subunit Knl1 (Kiyomitsu et al., 2007; Petrovic et al., 2016; Petrovic et al., 2014; Polley et al., 2024; Yatskevich et al., 2024). The orthologous budding yeast protein Knl1^{Spc105} also uses tandem RWD domains to interact with Mis12c^{Mtw1c} (Maskell et al., 2010), although the regions of Mis12c^{Mtw1c} that interact with yeast Knl1c are largely uncharacterised. Likewise, due to sequence differences between human and budding yeast Dsn1, the structural basis of Mis12c^{Mtw1c} auto-inhibition by an N-terminal region of Dsn1, and its relief by Aurora B^{Ipl1} phosphorylation (Akiyoshi et al., 2013; Kim and Yu, 2015; Yang et al., 2008) is unclear. To understand these differences, we determined cryo-EM structures of the *S. cerevisiae* KMN complex. The structure reveals that interactions between the three KMN sub-complexes are organised by α-helical motifs in the C-termini of the Mis12c^{Mtw1c} subunits Dsn1, Mis12^{Mtw1} and Nnf1, which engage interfaces on Knl1c and Ndc80c. Our work shows that a combination of conserved and plastic interfaces, divergent at the sequence and subunit level, underpin a comparable KMN complex architecture between point and regional centromeres. Furthermore, we show that Aurora B^{Ipl1} overcomes auto-inhibition of human Mis12c and budding yeast Mis12c^{Mtw1c} through similar structural mechanisms.

Results

Structural features of the budding yeast KMN complex

To determine the cryo-EM structure of the *S. cerevisiae* KMN complex, we purified Ndc80c and a Knl1c:Mis12c^{Mtw1c} complex (K^{HB-RWD}M) from insect cells (Figure S1A, B). K^{HB-RWD}M comprised a truncated Knl1^{Spc105} subunit (Knl1$^{Spc105_HB-RWD}$) that incorporated its helical bundle (HB) and tandem RWD domains but had a deleted N-terminal disordered region (retaining residues 445-917). Protein band intensities on SDS-PAGE gels (Figure S1B) indicated that the purified K^{HB-RWD}M contained one subunit of each of Knl1$^{Spc105_HB-RWD}$ and ZWINT^{Kre28}, a stoichiometry consistent with the number of Knl1^{Spc105} and ZWINT^{Kre28} proteins at kinetochores in cells defined using fluorescence microscopy (Roy et al., 2022).

We pursued numerous strategies to reconstitute and stabilise KMN on cryo-EM grids, with the best results obtained using the GraFix methodology (Kastner et al., 2008). The KMN complex (Figure 1A) was reconstituted by incubating K^{HB-RWD}M and Ndc80c (Figure S1C, D) at an equimolar ratio. K^{HB-RWD}MN complex formation was indicated by the co-migration in a glycerol gradient of its ten subunits, separate from K^{HB-RWD}M and Ndc80c (Figure S1E). The reconstituted K^{HB-RWD}MN (henceforth KMN) was crosslinked and purified using a 10-30% glycerol gradient with 0.0-0.2% glutaraldehyde (Figure S1F). We collected a large cryo-

127 EM dataset on this sample. Cryo-electron micrographs and 2D class averages revealed
128 elongated particles (Figure S2A, B) that corresponded closely with the previously observed
129 structures of isolated Mis12c^{Mtw1c}, Mis12c and Ndc80c, the entire human KMN complex, and
130 negative-staining EM of the budding yeast KMN complex (Ciferri et al., 2008; Dudziak et al.,
131 2025; Hornung et al., 2011; Maskell et al., 2010; Petrovic et al., 2014; Petrovic et al., 2010;
132 Polley et al., 2024; Wang et al., 2008; Wei et al., 2005; Yatskevich et al., 2024). We
133 determined medium-resolution cryo-EM maps of a KMN junction complex that contained the
134 stalk and head 1 domains of Mis12c^{Mtw1c}, and the RWD domains of Knl1c and Ndc80c
135 (Figures S2D-F and Table S1).

136 Overall, the *S. cerevisiae* KMN junction complex architecture (Figure 1B, C and Video S1)
137 (schematic in Figure 1F) resembles the human KMN complex (Polley et al., 2024; Yatskevich
138 et al., 2024) (Figure 1E, G). The Mis12c^{Mtw1c} structure is dominated by an α-helical bundle
139 assembled from its four subunits that form a central stalk. This stalk domain comprises three
140 coiled-coil (CC) regions (CC1, CC2 and CC3) (Dimitrova et al., 2016). Similar to human
141 KMN, the Knl1c and Spc24:Spc25 RWD domains are bound at the apex of the Mis12c^{Mtw1c}
142 stalk, and although in close proximity, are not in direct contact. The Mis12c^{Mtw1c} head 1
143 domain, comprising a short four α-helical bundle formed from the Mis12^{Mtw1} and Nnf1
144 subunits, is attached to the base of the stalk through loops, docking against Dsn1 and Nsl1 of
145 the CC1 region (Figure 1B, C). In the composite cryo-EM map of the *S. cerevisiae* KMN
146 junction complex, no density was observed for portions of Ndc80c comprising the
147 Spc24:Spc25 coiled-coils and the entire Ndc80:Nuf2 subcomplex. Likewise, for Knl1c, all
148 regions preceding the C-terminal RWD domains of Knl1^{Spc105} and ZWINT^{Kre28} were not
149 visible. Disorder of both the Ndc80c and Knl1c subcomplexes in *S. cerevisiae* KMN,
150 indicative of their conformational flexibility, was also observed in the human KMN structure
151 (Polley et al., 2024; Yatskevich et al., 2024).

152 Our structure of *S. cerevisiae* KMN also revealed important differences with the human KMN
153 complex, specifically in how Mis12c^{Mtw1c} interacts with both Knl1c and Ndc80c, and a C-
154 terminal RWD domain in ZWINT^{Kre28} (ZWINT^{Kre28_RWD}) that is absent from the human
155 ortholog (Figure 1C-G). An RWD domain in *S. cerevisiae* ZWINT^{Kre28} had previously been
156 predicted through phylogenetic analyses and AF2 models (Polley et al., 2024; Tromer et al.,
157 2019). In *S. cerevisiae* KMN, ZWINT^{Kre28_RWD} interacts with the N-terminal RWD domain of
158 Knl1^{Spc105}, a role played by the ZWINT C-terminal α-helix in human Knl1 (Yatskevich et al.,
159 2024). Lastly, in this reconstruction of the *S. cerevisiae* KMN junction complex, cryo-EM

density for the Mis12c^{Mtw1c} head 2 domain is not visible due to the subtraction of head 2 cryo-EM density for cryo-EM data processing.

Interactions of Mis12c^{Mtw1c} with Knl1c and Ndc80c and comparison with human KMN

Mis12c^{Mtw1c} contacts Knl1c through the Dsn1:Nnf1 CC3 coiled-coil and a peptidic extension of Mis12^{Mtw1}

The Dsn1, Mis12^{Mtw1} and Nnf1 subunits mediate Mis12c^{Mtw1c} interactions at two contact sites on Knl1c. First, conserved aliphatic residues in Dsn1 and the C-terminal α-helix of Nnf1 (Nnf1$^{Cterm\text{-}helix}$) (Figure 2C), part of Mis12c^{Mtw1c} CC3, engage a hydrophobic patch on the C-terminal RWD domain of Knl1^{Spc105} (Knl1$^{Spc105_RWD\text{-}C}$) (interface (1)) (Figures 1C, F and 2A-C and 3A, C and Video S1). In general, this *S. cerevisiae* Mis12c^{Mtw1c} – Knl1c interface resembles its counterpart in human KMN (Figure 2E, F) (Polley et al., 2024; Yatskevich et al., 2024).

At the second Mis12c^{Mtw1c} – Knl1c contact site, which differs from human KMN (Polley et al., 2024; Yatskevich et al., 2024), the extreme C-terminal α-helix of Mis12^{Mtw1} (residues 282-289: Mis12$^{Mtw1_Cterm\text{-}helix}$) engages a channel formed at the interface of the Knl1^{Spc105} RWD-N domain (Knl1$^{Spc105_RWD\text{-}N}$) and an α-helix of ZWINT^{Kre28} (ZWINT$^{Kre28_\alpha1\text{-}helix}$) (interface (2)) (Figures 1C, F and 2A, B, D-F and 3B, C). The ZWINT$^{Kre28_\alpha1\text{-}helix}$ combines with Knl1$^{Spc105_RWD\text{-}N}$ to create a hydrophobic channel that is ideally suited to bind the mixed hydrophobic and acidic Mis12$^{Mtw1_Cterm\text{-}helix}$ (Figure 2D). Immediately preceding Mis12$^{Mtw1_Cterm\text{-}helix}$, a β-strand from Mis12^{Mtw1} augments the β-sheet of Knl1$^{Spc105_RWD\text{-}N}$ (Figure 2B). Consistent with the observation that the ZWINT^{Kre28_RWD} domain is not essential for *S. cerevisiae* viability (Dudziak et al., 2025), our structure shows that although ZWINT^{Kre28_RWD} may indirectly stabilise ZWINT$^{Kre28_\alpha1\text{-}helix}$ through its contact with Knl1^{Spc105} (Figure 2B), ZWINT^{Kre28_RWD} does not contribute directly to contacting Mis12c^{Mtw1c} subunits. In human KMN, ZWINT lacks an RWD domain, and Mis12 does not contact Knl1c. Instead, the C-terminus of Nsl1 contacts the Knl1$^{RWD\text{-}N}$:ZWINT interface and a shallow groove on Knl1$^{RWD\text{-}N}$ (Petrovic et al., 2014; Polley et al., 2024; Yatskevich et al., 2024) (Figures 1G, 2F). Our experimental structure of the Mis12^{Mtw1} – Knl1c interface agrees with AF2 predictions of the Knl1c:Mis12c^{Mtw1c} complex (Figure 3C-E), supporting our assignment of cryo-EM densities to Mis12$^{Mtw1_Cterm\text{-}helix}$ and Nnf1$^{Cterm\text{-}helix}$ (Figure 3A, B).

190 Consistent with our structure, deletion of residues comprising and surrounding
191 Mis12$^{Mtw1_Cterm\text{-}helix}$ mildly reduced levels of Knl1^{Spc105} and ZWINT^{Kre28} that co-purified with
192 Mis12c^{Mtw1c} isolated from yeast (Ghodgaonkar-Steger et al., 2020). Indeed, we found that
193 deletion of either Mis12$^{Mtw1_Cterm\text{-}helix}$ or Nnf1$^{Cterm\text{-}helix}$ reduced the co-purification of
194 Mis12c^{Mtw1c} with Knl1c from insect cells (Figure 3F). These deletions did not affect the
195 stability nor assembly of Mis12c^{Mtw1c} (Figure S3A, B) nor its interaction with Ndc80c (Figure
196 S3C, D), suggesting that the specific functions of Mis12$^{Mtw1_Cterm\text{-}helix}$ and Nnf1$^{Cterm\text{-}helix}$ are to
197 mediate the interaction between Mis12c^{Mtw1c} and Knl1c.

198 To investigate the function of Mis12$^{Mtw1_Cterm\text{-}helix}$ and Nnf1$^{Cterm\text{-}helix}$ *in vivo* we used the auxin
199 inducible degron (AID) system (Tanaka et al., 2015) to deplete the endogenous *MTW1* and
200 *NNF1* gene products and tested whether mutant *mtw1* and *nnf1* proteins with their C-terminal
201 α-helices deleted (*mtw1*$^{\Delta C}$ and *nnf1*$^{\Delta C}$, respectively) rescued depletion of the endogenous
202 gene product. Western blotting confirmed that the mAID$_3$-FLAG$_5$ tagged gene products of the
203 endogenous MTW1 and NNF1 loci were depleted after addition of IAA (Figure S1G, H), and
204 that the rescue alleles were expressed from the exogenous loci (Figure S1I, J).

205 Consistent with the essentiality of Mis12^{Mtw1} and Nnf1 (Euskirchen, 2002), strains with an
206 empty cassette incorporated at the exogenous locus were unable to grow on plates containing
207 IAA (Figure S3E). The expression of wild type *MTW1* and *NNF1* rescue alleles rescued this
208 lethality (Figure S3E). The mutant *mtw1*$^{\Delta C}$ and *nnf1*$^{\Delta C}$ alleles also rescued lethality caused by
209 depletion of endogenous *MTW1* and *NNF1* at 30°C (Figure S3E). These data are consistent
210 with our *in vitro* results that deletion of either Mis12$^{Mtw1_Cterm\text{-}helix}$ or Nnf1$^{Cterm\text{-}helix}$ helices
211 alone reduces, but does not abolish, co-purification of Mis12c^{Mtw1c} with Knl1c (Figure 3F).
212 We were unable to test the consequence to cell growth of deleting Mis12$^{Mtw1_Cterm\text{-}helix}$ and
213 Nnf1$^{Cterm\text{-}helix}$ simultaneously because strains combining both *mtw1*$^{\Delta C}$ and *nnf1*$^{\Delta C}$ alleles with
214 AID-tagged *MTW1* and *NNF1* could not be isolated, suggestive of lethality.

215 *Mis12c*^{Mtw1c} *contacts Ndc80c through the Dsn1:Nsl1 CC3 coiled-coil and peptidic extensions*
216 *of Dsn1 and Mis12*^{Mtw1}

217 In the *S. cerevisiae* KMN junction complex, Mis12c^{Mtw1c} engages Ndc80c through multiple
218 contacts involving the RWD domains of Spc24 and Spc25 (Spc24^{RWD} and Spc25^{RWD}). These
219 interactions comprise the CC3 region of the Mis12c^{Mtw1c} stalk, and peptidic C-terminal
220 extensions of Dsn1 and Mis12^{Mtw1} (Figures 1C, F, 4 and 5A, B and Video S1). First, as
221 similarly observed in human KMN (Polley et al., 2024; Yatskevich et al., 2024), the

222 hydrophobic patch of the Spc24^{RWD} β-sheet interacts with hydrophobic residues of Dsn1 and
223 Nsl1 in CC3 (interface 3) (Figures 1C, F and 4B, C, E, F and 5A). Second, differing from
224 human KMN, an α-helical segment of Mis12^{Mtw1} (Mis12$^{Mtw1_Spc24\text{-}helix}$) buttresses Spc24^{RWD}
225 and the Spc24:Spc25 coiled-coil (interface 4) (Figures 1C, F and 4B, D-F and 5B), before
226 Mis12^{Mtw1} crosses to contact Knl1c through Mis12$^{Mtw1_Cterm\text{-}helix}$ (Figure 1C, F). The
227 interaction of Mis12$^{Mtw1_Spc24\text{-}helix}$ residues Tyr236 and Arg240 with Spc24^{RWD} and Spc25^{RWD}
228 is supported by well-resolved cryo-EM density (Figure 5B). These interactions likely
229 rationalise why Asp substitution of Mis12^{Mtw1} residues Arg233 and Tyr236 reduced levels of
230 Spc24:Spc25 associated with Mis12c^{Mtw1c} in an *in vitro* assay, and sensitises yeast to benomyl
231 (Ghodgaonkar-Steger et al., 2020). In human KMN, *S. cerevisiae* Mis12$^{Mtw1_Spc24\text{-}helix}$ is
232 functionally replaced by a short α-helix of Nsl1 (Nsl1$^{Spc24\text{-}helix}$) that buttresses Spc24^{RWD} and
233 the Spc24:Spc25 coiled-coil, before Nsl1 also crosses to contact Knl1c (Nsl1^{Cterm}) (Polley et
234 al., 2024; Yatskevich et al., 2024) (Figure 1F, G).

235 Thirdly, in another interaction that is conserved with human KMN (Polley et al., 2024;
236 Yatskevich et al., 2024) the C-terminal Dsn1 α-helix (residues 560-574: Dsn1$^{Cterm\text{-}helix}$) docks
237 into a deep channel at the interface of Spc24^{RWD} and Spc25^{RWD} (interface 4: Figures 1C, F
238 and 4B, D-F and 5B). However, the budding yeast KMN complex differs from human in that
239 the Mis12$^{Mtw1_Spc24\text{-}helix}$ stabilises this interaction. The four-turn Mis12$^{Mtw1_Spc24\text{-}helix}$ bridges
240 both Dsn1$^{Cterm\text{-}helix}$ and Spc24^{RWD} through interactions with Val244 and Leu245 of
241 Mis12$^{Mtw1_Spc24\text{-}helix}$ (Figure 4D and 5B). The shorter human Nsl1$^{Spc24\text{-}helix}$ does not extend to
242 contact the Dsn1$^{Cterm\text{-}helix}$ (Polley et al., 2024; Yatskevich et al., 2024). This interaction of
243 budding yeast Dsn1$^{Cterm\text{-}helix}$ with Mis12$^{Mtw1_Spc24\text{-}helix}$ might be the basis by which Dsn1$^{Cterm\text{-}}$
244 ^{helix} and Mis12$^{Mtw1_Spc24\text{-}helix}$ bind to Spc24:Spc25 cooperatively. This interface could also
245 explain how Asp substitutions of Mis12^{Mtw1} Val244, together with Leu248, a residue not
246 resolved in our structure, strongly impaired binding of Spc24:Spc25 and Mis12c^{Mtw1c} *in vitro*,
247 and confers benomyl sensitivity *in vivo* (Ghodgaonkar-Steger et al., 2020).

248 Lastly, our structure of Mis12$^{Mtw1_Spc24\text{-}helix}$ and Dsn1$^{Cterm\text{-}helix}$ bound to Spc24^{RWD}:Spc25^{RWD}
249 agrees with a crystal structure of the Spc24^{RWD}:Spc25^{RWD}:Dsn1$^{Cterm\text{-}helix}$ complex (Figure 5C)
250 (Dimitrova et al., 2016), and an AF2 prediction of Mis12c^{Mtw1c} with Spc24 and Spc25 (Figure
251 5D, E).

252 <u>Mechanism of Mis12c^{Mtw1c} auto-inhibition and activation by Aurora B^{Ipl1} kinase</u>

253 *An auto-inhibitory segment of Dsn1 engages the head 1 domain of Mis12c^{Mtw1c}*

The Dsn1 N-terminal intrinsically disordered region (N-IDR), situated immediately N-terminal of head 2, auto-inhibits the interaction of Mis12c^{Mtw1c} with the inner kinetochore (Dimitrova et al., 2016; Petrovic et al., 2016; Walstein et al., 2021; Yatskevich et al., 2024), whereas Aurora B^{Ipl1} phosphorylation of this region strengthens inner and outer kinetochore interactions (Akiyoshi et al., 2013; Kim and Yu, 2015; Yang et al., 2008). Due to signal subtraction of the Mis12c^{Mtw1c} head 2 domain during cryo-EM processing, our model of the KMN junction complex did not reveal the structural basis of Mis12c^{Mtw1c} auto-inhibition. However, we observed cryo-EM density on the surface of head 1 not accounted for in our model (Figure S2Dii). We reasoned this density might correspond to either a region of head 2, and/or a region of Dsn1$^{N\text{-}IDR}$ involved in auto-inhibition (Dimitrova et al., 2016). To investigate these possibilities, we performed focussed 3D classification of the non-signal subtracted KMN particles using a mask encompassing the base of the Mis12c^{Mtw1c} stalk, head 1 and putative head 2 domain (Figure S4A). Using this approach, we obtained a subset of particles that resulted in 3D reconstructions with defined cryo-EM density for the Mis12c^{Mtw1c} head 1 and head 2 domains (Figure S4 and Table S1).

The small number of particles (18,160) exhibiting head 2 associated with head 1 limited the global resolution of the reconstruction to 6.5 Å (Figure S4B), with a local resolution of 6.0 Å in regions of the map closest to the head 1 central region (Figure S4C). The overall conformations of the head 1 and Mis12c^{Mtw1c} stalk domains are unchanged compared to the composite cryo-EM map of the KMN junction complex (Figure S5A, B). To interpret the putative head 2 density (Figure S5A), we used an AF2 prediction of *S. cerevisiae* Spc24:Spc25:Mis12c^{Mtw1c} (Figure S5C, D). This accounted for the helical bundle of head 2 docked onto head 1, but not an additional α-helical-like density contacting head 1, nor continuous density between CC1 of the Mis12c^{Mtw1c} stalk and the head 2 domain (Figure S5A, B). Using crosslinking mass spectrometry (CL-MS) on the K$^{HB\text{-}RWD}$M complex, we identified crosslinks between residues in head 1 and head 2, in agreement with the docked configuration of head 2 (Figure 6A).

The AF2 model of *S. cerevisiae* Mis12c^{Mtw1c} (*Sc*Mis12c^{Mtw1c}) was not consistent with the conformation of head 2 in the *Sc*Mis12c^{Mtw1c} cryo-EM map with improved head 2 density (Figure S5E, F). By contrast, an AF2 prediction of Mis12c^{Mtw1c} from the related budding yeast *Kluyveromyces lactis* (*Kl*Mis12c^{Mtw1c}) better recapitulated the contacts between head 1 and 2 observed in the density map. In the *Kl*Mis12c^{Mtw1c} model the head 2 domain is confidently predicted to contact head 1 (Figure S5G, H) and matched our docking of *S.*

287 *cerevisiae* head 2 into cryo-EM density (Figure S5B, G). With this prediction of
288 *Kl*Mis12c^{Mtw1c}, we built a model of *Sc*Mis12c^{Mtw1c} which yielded an excellent fit into the
289 density map (Figure 6B, C). This model rationalises all cryo-EM density including that which
290 could not be assigned using AF2 predictions of *Sc*Mis12c^{Mtw1c} head 2 (grey density in Figure
291 S5A). A linker within Nsl1 connecting CC1 and head 2 docks into the continuous density
292 between CC1 and head 2 (Figure 6B, C), consistent with observed CL-MS crosslinks
293 between the Nsl1 linker and CC1 residues Dsn1^{K436}, Nsl1^{K105} and Nsl1^{Y106} (Figure 6D).
294 Within the N-IDR of *K. lactis* Dsn1, residues 201-230 (*Kl*Dsn1$^{201-230}$) are predicted to fold as
295 two α-helices joined by a short linker (Figure S5G, H). Indeed, this region of *Kl*Dsn1
296 mediates association of the *Kl*Mis12c^{Mtw1c} head 1 and head 2 domains *in vitro* and auto-
297 inhibits the interaction of *Kl*Mis12c^{Mtw1c} with *Kl*CENP-C^{Mif2} and *Kl*CENP-U^{Ame1} (Dimitrova
298 et al., 2016). This region of Dsn1 is referred to as the Dsn1 auto-inhibitory segment (Dsn1^{AI}).
299 Based on the sequence similarity of *Sc*Dsn1$^{228-257}$ and *Kl*Dsn1$^{201-230}$ (Figure 6F), we built
300 Dsn1^{AI} of *Sc*Mis12c^{Mtw1c} into the α-helical-like density as *Sc*Dsn1$^{229-255}$ (Figure 6B, C) using
301 the *Kl*Mis12^{Mtw1c} AF2 model. This assignment is supported by a CL-MS crosslink between
302 *Sc*Mis12^{Mtw1} Glu84 in head 1 and *Sc*Dsn1$^{229-255}$ Ser240 (Figure 6E). Importantly, *Sc*Dsn1^{229-}
303 ^{255} incorporates the Aurora B^{Ipl1} consensus sites Ser240 and Ser250 whose replacement with
304 Asp enhanced the association of *Sc*Dsn1 with inner kinetochore proteins (Akiyoshi et al.,
305 2013). In agreement with this, phospho-mimetic mutants of the equivalent residues in
306 *Kl*Dsn1$^{201-230}$ (Ser213 and Ser223) substantially increased the affinity of *Kl*Mis12c^{Mtw1c} for
307 N-terminal fragments of CENP-C^{Mif2} and CENP-U^{Ame1} (Dimitrova et al., 2016).

308 Consistent with our structure, an isothermal titration calorimetry (ITC) experiment showed
309 that a peptide of Dsn1 residues 228-254 (Dsn1$^{228-254}$) bound to K^{HB-RWD}M with the entire
310 Dsn1^{N-IDR} (residues 1-257) deleted (K^{HB-RWD}M$^{Dsn1\Delta257}$) with a K_D of 1.3 μM (Figure 6Gi). By
311 contrast, the Dsn1$^{228-254}$ peptide did not bind to K^{HB-RWD}M with both the Dsn1^{N-IDR} and head
312 1 deleted (K^{HB-RWD}M$^{Dsn1\Delta257_\Delta head1}$) (Figure 6Gii). Dsn1$^{229-255}$ is basic and projects Lys238,
313 Arg245 and Arg248 towards a cluster of negatively-charged residues in head 1 (Figure 6E).
314 That the Dsn1$^{228-254}$ peptide-binding site corresponds to the site on head 1 associated with the
315 α-helical-like density was also consistent with a threefold-increased K_D for its association
316 with the K^{HB-RWD}M$^{Dsn1\Delta257_Mis12-3A}$ mutant, which has a disrupted negatively-charged patch on
317 head 1 (Ala substitutions of Mis12^{Mtw1} Glu69, Glu73 and Asp77) (Figure 6E, Giii).

318 *Phosphoregulation of CENP-C^{Mif2} and CENP-U^{Ame1} binding to Mis12c^{Mtw1c}*

319 *K. lactis* Dsn1 residues, equivalent to those of *S. cerevisiae* Dsn1 that form the negatively-
320 charged patch of head 1 (Figure 6E), were implicated in binding the N-termini of CENP-C^{Mif2}
321 and CENP-U^{Ame1} (Dimitrova et al., 2016; Killinger et al., 2020). To understand the
322 mechanism of Mis12c^{Mtw1c} auto-inhibition, we superimposed the crystal structure of the
323 *Kl*Mis12c^{Mtw1c} head 1 bound to CENP-C^{Mif2} (Dimitrova et al., 2016) onto our model of the
324 KMN junction complex (Figure 7A). This indicated that Dsn1^{AI} (Dsn1$^{229-255}$) overlaps with
325 CENP-C^{Mif2} bound to head 1, supporting a mechanism for Mis12c^{Mtw1c} auto-inhibition in
326 which Dsn1^{AI} partially occludes the binding site of CENP-C^{Mif2}.

327 Phosphomimetic mutants of Aurora B^{Ipl1} consensus sites in *Sc*Dsn1$^{229-255}$ and *Kl*Dsn1$^{201-230}$
328 relieve Mis12c^{Mtw1c} auto-inhibition and increased CENP-C^{Mif2} and CENP-U^{Ame1} affinity for
329 the complex (Dimitrova et al., 2016; Lang et al., 2018). *Sc*Dsn1^{S250}, an Aurora B^{Ipl1} kinase
330 substrate (Maskell et al., 2010; Westermann et al., 2003), projects towards the negatively-
331 charged patch of Mis12c^{Mtw1c} head 1 (Figure 6E). Phosphorylation of *Sc*Dsn1^{S250}, and the
332 equivalent residue in *Kl*Dsn1 (Ser223), would cause electrostatic repulsion between the
333 phosphoserine and this negatively-charged patch, and likely clash with Dsn1 residues of head
334 2. This might relieve Mis12c^{Mtw1c} auto-inhibition by reducing the binding affinity of Dsn1^{AI}
335 for head 1, releasing it from the CENP-C^{Mif2} binding site. *Sc*Dsn1^{S240} and its equivalent
336 residue, *Kl*Dsn1^{S213}, conform to the Aurora B^{Ipl1} substrate consensus sequence. Although not
337 reported to be phosphorylated by Aurora B^{Ipl1}, *Sc*Dsn1^{S240} is phosphorylated *in vivo* (Lanz et
338 al., 2021). *Sc*Dsn1^{S240} projects away from head 1 (Figure 6E), however phosphorylation of
339 *Sc*Dsn1^{S240} and *Kl*Dsn1^{S213} could establish intramolecular interactions with positively
340 charged residues *Sc*Dsn1^{R237} and *Sc*Dsn1^{R247} (conserved in *K. lactis*, Figure 6F) to relieve
341 Mis12c^{Mtw1c} auto-inhibition by destabilising the Dsn1^{AI} α-helices. Consistent with these
342 proposals, an ITC experiment demonstrated that an *S. cerevisiae* Dsn1$^{228-254}$ peptide with
343 phosphomimetic mutations at the Dsn1^{S240} and Dsn1^{S250} Aurora B^{Ipl1} sites bound to K^{HB-}
344 ^{RWD}M$^{Dsn1\Delta257}$ with a K_D of 6.0 μM (Figure 6Giv), a five-fold lower affinity than the wildtype
345 peptide (Figure 6Gi).

346 To test the model that Dsn1^{AI} auto-inhibits *Sc*Mis12c^{Mtw1c}, we used analytical SEC to assess
347 binding of an N-terminal fragment of CENP-C^{Mif2} comprising residues 1-63 (CENP-C$^{Mif2_1-}$
348 ^{63}) to K^{HB-RWD}M complexes containing Dsn1 N-terminal truncations. CENP-C$^{Mif2_1-63}$ did not
349 bind K^{HB-RWD}M containing full length Dsn1 (Figure 7B, Cii) but did interact with K^{HB-}
350 ^{RWD}M$^{Dsn1\Delta257}$ (Figure 7B, Ciii), similar to previous reports for *Kl*Mis12c^{Mtw1c} (Dimitrova et
351 al., 2016). This indicated that the region mediating Mis12c^{Mtw1c} auto-inhibition is within

352 Dsn1$^{N\text{-}IDR}$. CENP-C$^{Mif2_1\text{-}63}$ did not bind K$^{HB\text{-}RWD}$M$^{Dsn1\Delta226}$ which lacked the N-terminal 226
353 amino acids of Dsn1 (Figure 7B, Civ), demonstrating that residues 227-257 of Dsn1,
354 corresponding to Dsn1^{AI}, are sufficient to confer Mis12c^{Mtw1c} auto-inhibition. Aurora B^{Ipl1}
355 Dsn1^{S240E} and Dsn1^{S250E} phosphomimetic mutants within Dsn1^{AI} in either full-length Dsn1
356 (Figure 7B, Cv) or Dsn1$^{\Delta1\text{-}226}$ (Figure 7B, Cvi) were sufficient to abolish Mis12c^{Mtw1c} auto-
357 inhibition. Together, these results indicate that Dsn1^{AI} auto-inhibits Mis12c^{Mtw1c} by binding to
358 head 1, and that either Aurora B^{Ipl1} phosphorylation of Ser240 and Ser250 or deletion of the
359 N-terminal 257 amino acids of Dsn1 relieves Mis12c^{Mtw1c} auto-inhibition.

360 We further investigated the effect of Dsn1^{AI} on the interaction between K$^{HB\text{-}RWD}$M (which has
361 wild-type unphosphorylated Dsn1^{AI}) and a peptide modelled on the N-terminal 38 residues of
362 CENP-C^{Mif2} (CENP-C$^{Mif2_1\text{-}38}$). Using ITC, we did not detect an interaction between CENP-
363 C$^{Mif2_1\text{-}38}$ and K$^{HB\text{-}RWD}$M (Figure 7Di). In contrast, CENP-C$^{Mif2_1\text{-}38}$ associated with K$^{HB\text{-}}$
364 ^{RWD}M^{2E} (incorporating Dsn1^{S240E} and Dsn1^{S250E} phosphomimetic mutants) with a K_D of 0.98
365 μM (Figure 7Dii), an affinity similar to CENP-C$^{Mif2_1\text{-}41}$ binding to *Kl*Mis12c^{Mtw1c} with
366 phosphomimetic mutations of Dsn1^{AI} (K_D of 1.75 μM) (Dimitrova et al., 2016). These data
367 are consistent with Aurora B^{Ipl1} phosphorylation of Dsn1 overcoming auto-inhibition of
368 Mis12c^{Mtw1c} stimulating its association with CENP-C^{Mif2}.

369 Budding yeast Mis12c^{Mtw1c} binds an N-terminal segment of CENP-U^{Ame1}, however there are
370 conflicting data concerning whether Mis12c^{Mtw1c} auto-inhibition affects this interaction
371 (Dimitrova et al., 2016; Hornung et al., 2014). A complex of *S. cerevisiae* CENP-U^{Ame1} and
372 CENP-Q^{Okp1} (CENP-QU) binds to *Sc*Mis12c^{Mtw1c} with wildtype Dsn1^{AI} when both are at
373 micromolar concentrations, as assessed by analytic SEC (Hornung et al., 2014). However,
374 another study using fluorescence polarisation showed that, at lower concentrations (50 nM),
375 the N-terminal 25 amino acids of *K. lactis* CENP-U^{Ame1} did not interact with *Kl*Mis12c^{Mtw1c}
376 containing an intact Dsn1^{AI} (Dimitrova et al., 2016). To investigate these apparent
377 discrepancies and to understand how Dsn1^{AI} regulates Mis12c^{Mtw1c} – CENP-U^{Ame1}
378 interactions, we superimposed an AF2 structure prediction of *S. cerevisiae* Mis12c^{Mtw1c} bound
379 to CENP-U^{Ame1} (Figures 8A and 9C, D) onto our model of the KMN junction complex
380 (Figure 8B). The AF2-predicted structure of CENP-U^{Ame1} residues 1-33 (CENP-U$^{Ame1_1\text{-}33}$)
381 bound to head 1 clashed with Dsn1^{AI} (Figure 8B) more extensively than CENP-C^{Mif2} bound
382 to the Mis12c^{Mtw1c} head 1 domain (Figure 7A). The mode of CENP-U^{Ame1} binding to head 1,
383 involving a basic α-helix lying along the acidic patch of head 1, is strikingly similar to how
384 Dsn1^{AI} interacts with head 1 (Figures 6C, 8B,C and 9C). This suggests that Dsn1^{AI} also

385 inhibits the interaction between Mis12c^{Mtw1c} and CENP-U^{Ame1} by occluding the CENP-
386 U^{Ame1}-binding site on head 1. The AF2 model predicts that CENP-U^{Ame1} binds to a site on
387 head 1 that is mainly distinct from the CENP-C^{Mif2}-binding site (Dimitrova et al., 2016), but
388 that both ligands nevertheless share a small common binding surface (Figure 8D). This may
389 explain why CENP-C^{Mif2} and CENP-U^{Ame1} associate with Mis12c^{Mtw1c} mutually exclusively
390 (Killinger et al., 2020).

391 Although analytical SEC showed that CENP-QU bound to K^{HB-RWD}M with full-length wild-
392 type Dsn1 with partial dissociation (Figure 8E, F), consistent with previous results (Hornung
393 et al., 2014), in an ITC experiment using 16 μM K^{HB-RWD}M, we did not detect K^{HB-RWD}M
394 binding to 400 μM CENP-U$^{Ame1_1-33}$ (residues 1-33 residues of CENP-U^{Ame1}) (Figure 8Gi).
395 Consistent with the model that Aurora B^{Ipl1} kinase phosphorylation of Dsn1 strengthens
396 CENP-U binding to KMN, KM^{2E} with Dsn1^{S240E} and Dsn1^{S250E} phosphomimetic mutations,
397 bound CENP-U$^{Ame1_1-33}$ with a K_D of 0.24 μM (Figure 8Gii). This binding affinity is six-fold
398 higher than that observed for residues 1-25 of *K. lactis* CENP-U$^{Ame1_1-25}$ to *Kl*Mis12c^{Mtw1c}
399 containing phosphomimetic mutations (K_D of 1.48 μM) (Dimitrova et al., 2016), an increase
400 likely explained by the predicted interactions of CENP-U^{Ame1} residues 27-33 with
401 Mis12c^{Mtw1c} head 1 (Figure 8A). In agreement with this, substituting Ala residues in CENP-
402 U$^{Ame1_1-33}$ to disrupt interactions of CENP-U^{Ame1} residues 27-33 with KM^{2E} reduced CENP-
403 U$^{Ame1_1-33-Mut}$ binding affinity to a K_D of 1.31 μM (Figure 8Giii). The increased affinity of
404 CENP-U$^{Ame1_1-33}$ for KM^{2E} relative to CENP-C$^{Mif2_1-38}$, may explain the binding of CENP-
405 QU and not CENP-C$^{Mif2_1-63}$ to K^{HB-RWD}M as assessed by SEC (Figures 7C and 8E, F).

406 Human Mis12c binds CENP-C more tightly than its budding yeast counterpart, with non-
407 phosphorylated Mis12c also capable of binding CENP-C (Petrovic et al., 2016; Yatskevich et
408 al., 2024). One explanation for this difference is an N-terminal 13-residue extension in human
409 CENP-C that interacts with Mis12c head 1 (Petrovic et al., 2016), reminiscent of how
410 *Sc*CENP-U^{Ame1} is predicted to bind *Sc*Mis12c^{Mtw1} (Figure 9C, E).

411 <u>Model for Aurora B^{Ipl1}-dependent activation mediated by conformational changes of head 2</u>

412 Relative to our cryo-EM structure, head 2 in the AF2 *Sc*Mis12c^{Mtw1c} model is rotated ~90°
413 and displaced from head 1, with Dsn1^{AI} adopting an extended conformation (Figures 6C and
414 S5E). The separated configuration of head 1 and head 2 in the AF2 *Sc*Mis12c^{Mtw1c} model is
415 reminiscent of crystal structures of human Mis12c bound to CENP-C (Petrovic et al., 2016)
416 and *Kl*Mis12c^{Mtw1c} from which the auto-inhibitory segment was absent (Dimitrova et al.,

2016) (Figure 9E, F). Additionally, the orientation of head 2 in the *Kl*Mis12c^{Mtw1c} crystal structure closely matches that of the AF2 *Sc*Mis12c^{Mtw1c} model (Figures 9F and S5E, F). This suggests that the AF2 *Sc*Mis12c^{Mtw1c} model represents a plausible prediction of the Aurora B^{Ipl1}-phosphorylated, activated state of *Sc*Mis12c^{Mtw1c}. Consistent with this proposal, binding sites for CENP-C^{Mif2} and CENP-U^{Ame1} on head 1 are also not occluded by Dsn1^{AI} in this conformation (Figure 9A, C and Video S2). Dsn1^{AI}-mediated auto-inhibition of *Sc*Mis12c^{Mtw1c} resembles mechanisms proposed for human Mis12c in which Dsn1^{AI} bridges the two head domains, and together with head 2, occludes the inner kinetochore-binding sites on head 1 (Figure 9G) (Yatskevich et al., 2024).

Model of the entire *S. cerevisiae* KMN complex

We were unable to identify particles in our cryo-EM datasets that contained signal for the predicted Knl1c helical bundle domain (Figures S1A, and 10A, C), nor for the Spc24:Spc25 coiled-coils and Ndc80:Nuf2 subunits (Figures S1A, and 10A, B). AF2 generated a structure prediction for the Knl1c helical bundle (residues 492 to 632 of Knl1^{Spc105} and 7 to 194 of ZWINT^{Kre28}) with high confidence (Figure 10A, C). This helical bundle is connected to the Knl1c RWD domains by two segments in Knl1^{Spc105} and ZWINT^{Kre28} ('linker 1' and 'linker 2') that were predicted to adopt extended conformations with lower pLDDT scores (Figure 10A, C). Flexibility of linker 2 would explain why we were unable to resolve Knl1c domains beyond the RWD domains. An equivalent linker does not interrupt the coiled-coil of human Knl1c, possibly explaining why its cryo-EM density was visible (Yatskevich et al., 2024). We also performed AF2 structure predictions of Ndc80c. We observed a bent conformation that brings the Ndc80c microtubule binding elements (Ndc80c CH domains and Ndc80 N-tail) into proximity with an intermediate section of the Ndc80:Nuf2 coiled-coil (Figure 10A, B). Although isolated Ndc80c has been observed to exhibit modest bending by negative stain electron microscopy (Wang et al., 2008), such a highly bent conformation is unlikely to be adopted in the presence of microtubules or Dam1c rings (Aravamudhan et al., 2014; Muir et al., 2023). In the structure predicted by AF2, the Spc24:Spc25 coiled-coils are connected to their respective RWD domains by a linker ('Spc24:Spc25 linker') (Figure 10B). We expect that we were unable to resolve domains beyond the Spc24:Spc25 linker in our cryo-EM analysis because it flexibly tethers the Ndc80c coiled-coils and microtubule binding elements to the KMN junction. FRET measurements performed in the absence of both microtubules and Dam1c showed that Ndc80c bending is dynamic, and that more tightly bent Ndc80c conformations than those predicted by AF2 are possible (Scarborough et al., 2019). However,

these tightly bent conformations are adopted with low propensity in complex with Mis12c^{Mtw1c} (Scarborough et al., 2019).

We generated a model of the *S. cerevisiae* KMN complex by superimposing the AF2 predictions of Knl1c and Ndc80c onto their corresponding RWD domains in the KMN junction complex structure (Figure 10A). The close proximity of the Knl1c helical bundle to the Spc24:Spc25 coiled-coils in the hypothetical model is consistent with previous CL-MS analysis of the budding yeast KMN complex (Ghodgaonkar-Steger et al., 2020), although the exact positions of the domains are probably not correct. The Knl1c helical bundle is also close to the Ndc80c microtubule binding elements.

Discussion

Our cryo-EM structure and biochemical data of the *S. cerevisiae* KMN junction complex revealed both similarities and differences in how budding yeast Mis12c^{Mtw1c} and human Mis12c interact with Knl1c and Ndc80c, and the mechanism of Aurora B^{Ipl1}-mediated regulation of KMN assembly onto the inner kinetochore. For both species, Mis12c^{Mtw1c}/Mis12c interacts with Knl1c and Ndc80c through two distinct interaction modes. In a conserved mode of interaction, the coiled-coil (CC3) α-helices of the Mis12c^{Mtw1c}/Mis12c stalk creates a rigid interface for docking with Knl1c and Ndc80c (Figure 1F, G). Specifically, Dsn1:Nsl1 contact Ndc80c, whereas Dsn1:Nnf1 contact Knl1c. The other mode of interaction is mediated by C-terminal extensions of Mis12c^{Mtw1c}/Mis12c subunits that interact with sites on Knl1c and Ndc80c. Conserved in both human and budding yeast KMN is the interaction of Dsn1$^{Cterm\text{-}helix}$ at the interface of the Spc24:Spc25 RWD domains of Ndc80c (Figure 1F, G), a site that also binds the Ndc80c-binding α-helix of CENP-T (Malvezzi et al., 2013; Nishino et al., 2013). The most striking difference between budding yeast and human KMN is the contrasting functions of the Mis12^{Mtw1} and Nsl1 subunits to contact Knl1c and Ndc80c. In human KMN, an α-helix of Nsl1 (Nsl1$^{Spc24\text{-}helix}$) contacts the Ndc80c Spc24:Spc25 RWD domains (Figure 1G). Nsl1 then engages Knl1c at Knl1$^{RWD\text{-}N}$, and at the Knl1$^{RWD\text{-}N}$:ZWINT interface. In budding yeast these functions are substituted by Mis12^{Mtw1}. Mis12$^{Mtw1_Spc24\text{-}helix}$ contacts the Spc24:Spc25 RWD domains, which also stabilises the Dsn1$^{Cterm\text{-}helix}$:Spc24^{RWD}:Spc25^{RWD} interaction (Figure 1F). The Mis12^{Mtw1} chain then interacts with the Knl1$^{Spc105_RWD\text{-}N}$:Kre28^{ZWINT} interface of Knl1c.

Our hypothetical model of the entire *S. cerevisiae* KMN complex including the flexible tethering of other Knl1c and Ndc80c domains to the RWD domains of the KMN junction could have functional consequences for spindle assembly checkpoint (SAC) signalling (Fig. 10). Experiments in humans and budding yeast are consistent with a model in which SAC signalling is activated at kinetochores that are not attached to microtubules (Rieder et al., 1995; Wells and Murray, 1996), and that therefore do not incorporate Dam1c rings (Li et al., 2002; Tanaka et al., 2007; Tanaka et al., 2005). Under these conditions, Ndc80c might adopt a conformation in which its microtubule binding elements localise near the Knl1c helical bundle domain and the N-terminal disordered region of Knl1^{Spc105}. This may facilitate Mps1, bound proximal to the Ndc80c CH domains (Parnell et al., 2024; Pleuger et al., 2024; Zahm and Harrison, 2024), in phosphorylating MELT motifs in the Knl1^{Spc105} N-terminal disordered region to stimulate SAC signalling.

We determined a lower-resolution cryo-EM reconstruction of the KMN junction complex in which head 2 of Mis12c^{Mtw1c} was resolved. The auto-inhibitory region Dsn1^{AI} suppressed binding of Mis12c^{Mtw1c} to the N-terminal segments of both CENP-C^{Mif2} and CENP-U^{Ame1}. Phosphomimetic mutations of Aurora B^{Ipl1} sites within a peptide modelled on Dsn1^{AI} reduced its affinity for the K^{HB-RWD}M$^{Dsn1\Delta257}$ complex. Additionally, the same phosphomimetic mutations in Dsn1^{AI} activated K^{HB-RWD}M binding of both CENP-C^{Mif2} and CENP-U^{Ame1}. These results suggest that the intra-molecular association of Dsn1^{AI} with Mis12c^{Mtw1c} head 1 is responsible for Mis12c^{Mtw1c} auto-inhibition, and that Aurora B^{Ipl1} phosphorylation of serine residues within this region relieves Mis12c^{Mtw1c} auto-inhibition by reducing the binding affinity of Dsn1^{AI} for head 1. Cryo-EM structures and AF2 models suggest that this is because the Dsn1^{AI} and CENP-U^{Ame1} would sterically clash if both bound to head 1 (Figure 8C). Such a steric clash does not occur between CENP-C^{Mif2} and Dsn1^{AI}; instead, the two elements compete for contacts with the same amino side chains within head 1 (Figure 7A). The higher affinity of CENP-U^{Ame1} for KMN relative to CENP-C^{Mif2}, as evidenced by our ITC data, and the binding of CENP-QU, but not CENP-C$^{Mif2_1-63}$, to unphosphorylated K^{HB-RWD}M on SEC (this study and Hornung et al., 2014), has implications for understanding observations that CENP-U^{Ame1} is essential for yeast viability (Hornung et al., 2014; Schmitzberger et al., 2017), whereas the N-terminus of CENP-C^{Mif2} is dispensable (Hornung et al., 2014). Aurora B^{Ipl1} localisation to CCAN is necessary for the correction of erroneous kinetochore microtubule attachments (Fischböck-Halwachs et al., 2019; García-Rodríguez et al., 2019; Li et al., 2023). Our findings therefore suggest a mechanism by which attachments

513 of mitotic chromosomes to spindle microtubules, mediated by the connection of KMN
514 complexes to centromere-bound CCAN through either CENP-C^{Mif2} or CENP-U^{Ame1}, are
515 strengthened at kinetochores that are able to correct errors in these attachments.

516 Our work has revealed that the mechanisms mediating assembly and auto-inhibition of the
517 KMN complex are conserved at the structural level in humans and budding yeast.
518 Furthermore, we showed that Aurora B^{Ipl1}-mediated phosphorylation overcomes auto-
519 inhibition of human Mis12c and budding yeast Mis12c^{Mtw1c} through similar structural
520 mechanisms. In humans, Aurora B regulation of Mis12c auto-inhibition probably restricts
521 KMN complex recruitment to mitotic kinetochores that are competent to correct erroneous
522 kinetochore-microtubule attachments through error correction signalling (Yatskevich et al.,
523 2024). This and a previous study (Hornung et al., 2014) revealed that in budding yeast the
524 inner kinetochore subunit CENP-U^{Ame1} binds to unphosphorylated Mis12c^{Mtw1c}. In contrast to
525 humans, the KMN complex is attached to the centromere throughout almost the entire cell
526 cycle in budding yeast, with only transient disassembly of kinetochores during S-phase
527 (Kitamura et al., 2007). Furthermore, Aurora B^{Ipl1} is recruited to kinetochores from G1 to
528 metaphase, being depleted from centromeres under tension at metaphase and relocalising to
529 the spindle midzone (Buvelot et al., 2003; Campbell and Desai, 2013; Edgerton et al., 2023;
530 Nerusheva et al., 2014; Shimogawa et al., 2009). Consequently, relief of Mis12c^{Mtw1c} auto-
531 inhibition from G1-phase to metaphase through phosphorylation by Aurora B^{Ipl1} most likely
532 strengthens pre-existing connections between the inner and outer kinetochore, allowing
533 bioriented kinetochores to withstand the pulling and pushing forces exerted by spindle
534 microtubules. However, the diminished, but not abolished, affinity of both CENP-U^{Ame1} for
535 unphosphorylated Mis12c^{Mtw1c} is possibly still able to support kinetochore-microtubule
536 attachment during anaphase after Aurora B^{Ipl1} has localised away from kinetochores.

537 **Materials and methods**

538 Cloning of *S. cerevisiae* CENP-C^{Mif2} and *S. cerevisiae* KMN complex proteins

539 Genes encoding *S. cerevisiae* Ndc80, Nuf2, Spc24, Spc25, Dsn1, Mis12^{Mtw1}, Nnf1, Nsl1,
540 residues 1-444 of Knl1^{Spc105}, and ZWINT^{Kre28} were each amplified by Polymerase chain
541 reaction (PCR) from *S. cerevisiae* strain S288c genomic DNA (Zhang et al., 2016). Genes
542 encoding Ndc80 and Nuf2 were cloned into the same *pU1* plasmid (Zhang et al., 2016).
543 Genes encoding Spc24 and Spc25 were cloned into the same *pF1* plasmid (Zhang et al.,
544 2016). Genes encoding Knl1^{Spc105} residues 445-917 (Knl1$^{Spc105_HB\text{-}RWD}$) and ZWINT^{Kre28} were

545 cloned into the same modified *pF1* plasmid. Genes encoding Knl1^{Spc105} residues 710–917
546 (Knl1^{Spc105_RWD}) and ZWINT^{Kre28} residues 268-385 (ZWINT^{Kre28_RWD}) were cloned into the
547 same modified *pF1* plasmid. TEV and HRV-3C cleavable twin-strep-tag II (TS) tags were
548 introduced into the C-termini of Nuf2 and ZWINT^{Kre28}, respectively, and a tandem tag
549 comprising maltose binding protein (MBP) fused to monomeric enhanced green fluorescent
550 protein (mEGFP) was introduced into the N-terminus of Knl1^{Spc105_RWD}. Genes encoding
551 Dsn1, Mis12^{Mtw1}, Nsl1, and Nnf1 were cloned into the same modified *pF1* plasmid for
552 coexpression with Knl1^{Spc105} and ZWINT^{Kre28}. For expression of Mis12c^{Mtw1c} and
553 Mis12c^{Mtw1c} mutants, Dsn1 and Nsl1 were cloned into the same modified *pF1* plasmid and
554 twin-strep-tag II was introduced into the N-terminus of Dsn1. This plasmid was used to
555 generate a virus for coexpression with a second virus generated from a another modified *pF1*
556 plasmid containing a Mis12^{Mtw1}- Nnf1 pair. Constructs for Dsn1$^{\Delta 1\text{-}226}$, Dsn1$^{\Delta 1\text{-}226,S240E,S250E}$,
557 Dsn1$^{\Delta 1\text{-}257}$, Dsn1^{S240E,S250E}, Mis12^{Mtw1_E69A,E73A,E77A}, Mis12$^{Mtw1_\Delta 272\text{-}C}$, and Nnf1$^{\Delta 180\text{-}C}$ were
558 created using primers supplied from Merck and the KLD reaction kit supplied by New
559 England Biolabs and cloned into plasmids containing all other Mtw1c subunits for
560 coexpression with Knl1$^{Spc105_HB\text{-}RWD}$ and ZWINT^{Kre28}. Constructs for Mis12$^{Mtw1_\Delta 272\text{-}C}$ and
561 Nnf1$^{\Delta_180\text{-}C}$ were additionally cloned into the plasmid containing the Mis12^{Mtw1}-Nnf1 pair and
562 expressed together with a virus made from the plasmid containing a Dsn1-Nsl1 pair. To
563 express Knl1c:Mis12c^{Mtw1c} with the Mis12c head 1 domain deleted, constructs for
564 Mis12$^{Mtw1_\Delta 1–106}$ and Nnf1$^{\Delta 1\text{-}104}$ were cloned with Dsn1$^{\Delta 1\text{-}257}$ and wildtype Nsl1 into the same
565 modified *pF1* plasmid and coexpressed with Knl1^{Spc105} and ZWINT^{Kre28}. To express
566 Knl1c:Mis12c^{Mtw1c} with mutated Dsn1, constructs for Mis12^{Mtw1}, Nnf1, Nsl1, and mutant
567 Dsn1 were cloned into the same modified *pF1* plasmid and coexpressed with Knl1^{Spc105} and
568 ZWINT^{Kre28}.

569 The gene encoding *S. cerevisiae* CENP-C^{Mif2} residues 1-63 (CENP-C$^{Mif2_1\text{-}63}$) was amplified
570 from *S. cerevisiae* strain S288c genomic DNA and cloned into a pET28 plasmid carrying a
571 Kanamycin selectable marker. A 6xHis-SUMO- tag was introduced into the N-terminus of the
572 protein. A construct to express protein for surface plasmon resonance (SPR) was assembled
573 by introducing a 6xHis-SUMO- tag was introduced into the N-terminus of the protein and a
574 glycine-serine-glycine linker followed by a twin-strep-tag II (TS) tag into the C-terminus of
575 the protein.

576 To construct plasmids for yeast strain construction, the promoter, coding regions, and
577 terminator regions defined previously for the *MTW1* and *NNF1* genes in the yeast genome
578 (Euskirchen, 2002) were amplified from *S. cerevisiae* strain S288c genomic DNA. The
579 *MTW1* fragments were cloned into a modified *pRS304* plasmid (Frigola et al., 2013) and a
580 HA_3 tag was introduced into the N-terminus of the protein in a single step using NEBuilder
581 HiFi DNA assembly reaction kit supplied by New England Biolabs. The *NNF1* fragments
582 were cloned into a modified *pRS305* plasmid (Frigola et al., 2013) and a $V5_3$ tag was
583 introduced into the N-terminus of the protein in a single step using NEBuilder HiFi DNA
584 assembly reaction kit. A *pRS304* series plasmid and a *pRS305* series plasmid encoding HA_3-
585 $Mis12^{Mtw1_\Delta 272\text{-}C}$ and $V5_3$- $Nnf1^{\Delta 180\text{-}C}$ were constructed from the plasmids described above
586 using PCR with primers supplied by Merck followed by processing with the KLD reaction kit
587 supplied by New England Biolabs.

588 <u>Expression and purification of KMN subcomplexes, and CENP-$C^{Mif2_1\text{-}63}$ and CENP-QU</u>
589 <u>complexes</u>

590 Baculoviruses for expression of KMN subcomplexes were generated from the plasmids
591 described above using methods described previously (Zhang et al., 2016). Ndc80c was
592 expressed from two baculoviruses encoding a Ndc80-Nuf2 gene pair and a Spc24-Spc25 gene
593 pair in High-5 insect cells. Six-subunit Knl1c:$Mis12c^{Mtw1c}$ complexes were expressed from
594 two baculoviruses encoding a $Knl1^{Spc105_HB\text{-}RWD}$-$ZWINT^{Kre28}$ gene pair and a Dsn1- Nsl1-
595 $Mis12^{Mtw1}$- Nnf1 gene quartet in High-5 insect cells. Isolated $Mis12c^{Mtw1c}$ was expressed
596 from two baculoviruses encoding $Mis12^{Mtw1}$- Nnf1 and Dsn1-Nsl1 gene pairs. The Sf9 and
597 High-5 insect cell lines used for baculovirus generation and protein complex expression were
598 not tested for mycoplasma contamination or authenticated. 2 L roller bottles containing 500
599 mL suspension cultures of High-5 cells were typically infected with 2.5% vol/vol of P3 Sf9
600 suspension cell culture, and the High-5 expression cultures were subsequently harvested 42–
601 70 h after infection when the cell viability had dropped to 75–85%.

602 All purification steps were carried out at 4 ˚C or on ice. Cells expressing Ndc80c,
603 Knl1c:$Mis12c^{Mtw1c}$, or $Mis12c^{Mtw1c}$ were lysed by sonication in lysis buffer (50 mM Tris.HCl
604 pH 8.5, 8 mM benzamidine, 1 mM EDTA, 1 mM TCEP, 0.2 mM PMSF, cOmplete EDTA-
605 free protease inhibitor tablets) containing benzonase and either 300 mM NaCl and 7.5%
606 glycerol (Ndc80c), 250 mM NaCl and 7.5% glycerol ($Mis12c^{Mtw1c}$), or 200 mM NaCl and 5%
607 glycerol (Knl1c:$Mis12c^{Mtw1c}$). Lysates were cleared by ultracentrifugation at 38,000 x *g* for

608 one h and loaded onto Strep-Tactin superflow plus cartridges (Qiagen). Immobilised
609 complexes were washed with lysis buffer after adjusting to pH 8.0. Immobilised
610 Knl1c:Mis12c^{Mtw1c} complexes were subjected to further washes with a buffer containing ATP
611 (50 mM Tris.HCl pH 8.0, 175 mM KCl, 10 mM $MgCl_2$, 2.5 mM ATP sodium salt, 1 mM
612 TCEP, 2.5% glycerol) followed by a buffer containing 50 mM Tris.HCl pH 8.0, 200 mM
613 NaCl, 2.5% glycerol. Bound complexes were then eluted using a buffer containing 50 mM
614 Tris.HCl pH 8.0, 2.5 mM d-desthiobiotin, 1 mM TCEP, and either 100 mM NaCl (Ndc80c,
615 Mis12c^{Mtw1c}, and Knl1c:Mis12c^{Mtw1c} used for SPR) or 200 mM NaCl (Knl1c:Mis12c^{Mtw1c} for
616 all applications other than SPR). Knl1c:Mis12c^{Mtw1c} used for SPR was incubated overnight
617 with TEV protease whilst rolling at 4 ˚C to remove the C-terminal twin-strep-tag II sequences
618 from Kre28.

619 Knl1c:Mis12c^{Mtw1c} used for SPR and Ndc80c were further purified by loading the TEV
620 protease cleavage reaction and Strep-Tactin eluate, respectively, onto a Resource Q anion
621 exchange column (Cytiva). Bound complexes were eluted with buffer containing 50 mM
622 Tris.HCl pH 8.0, 1 mM TCEP, 2.5% glycerol and a gradient from 100 mM to 1000 mM NaCl
623 over 15-20 column volumes. Peak fractions were pooled, and salt concentration in pooled
624 Knl1c:Mtw1c protein was reduced to 150 mM prior to incubation for 30 min whilst rolling at
625 4 ˚C. Pooled protein was further purified using a Superose 6 10/300 increase GL column
626 (Cytiva) equilibrated in KMN buffer (20 mM HEPES pH 7.5, 150 mM NaCl, 1 mM TCEP).
627 Peak Ndc80c fractions were pooled, concentrated, and flash frozen using liquid nitrogen.

628 Mis12c^{Mtw1c} complexes and Knl1c:Mis12c^{Mtw1c} complexes used for all applications other than
629 SPR were further purified by concentrating the Strep-Tactin eluate and applying it to a
630 Superose 6 increase 10/300 GL column equilibrated in KMN buffer. The peak protein
631 complex fractions were concentrated and flash frozen using liquid nitrogen.

632 CENP-C$^{Mif2_1\text{-}63}$ with a N-terminal 6xHis-SUMO- tag was expressed in *E. coli* BL-21
633 CodonPlus RIL cells by induction with 0.5 mM IPTG at a cell culture OD_{600nm} = 0.8 followed
634 by incubation of cells a further 18 h at 18 ˚C with shaking. Cells were harvested by
635 centrifugation and lysed by sonication in lysis buffer (30 mM Tris.HCl pH 8.0, 300 mM
636 NaCl, 1 mM EDTA, 1 mM TCEP, 0.2 mM PMSF) containing benzonase and 10 mM
637 imidazole. The lysate was cleared by ultracentrifugation at 38,000 x *g* in a JA25.50 rotor for
638 1 h, and the clarified lysate was applied to a HisTrap excel column (Cytiva). Immobilised
639 proteins were washed with lysis buffer and were eluted by successive applications of lysis

640 buffer containing 50 mM, 100 mM, 150 mM, 300 mM, and 500 mM imidazole. The eluates
641 obtained after application of 150 mM and 300 mM imidazole were pooled and applied to
642 HiPrep 26/10 desalting columns (Cytiva) that were equilibrated in buffer containing 20 mM
643 HEPES pH 7.5, 300 mM NaCl, 1 mM EDTA, 1 mM TCEP) to reduce the imidazole content.

644 CENP-C$^{Mif2_1\text{-}63}$ with a N-terminal 6xHis-SUMO- tag and a C-terminal twin-strep-tag II (TS)
645 tag (CENP-C$^{Mif2_1\text{-}63}$-TS) was expressed in *E. coli* BL-21 CodonPlus RIL cells by induction
646 with 0.5 mM IPTG at a cell culture OD_{600nm} = 0.7 followed by incubation of cells a further 14
647 h 30 min at 18 ˚C with shaking. Cells were harvested by centrifugation and lysed by
648 sonication in lysis buffer (30 mM Tris.HCl pH 8.0, 300 mM NaCl, 1 mM EDTA, 1 mM
649 TCEP, 0.2 mM PMSF) containing benzonase. The lysate was cleared by ultracentrifugation at
650 48,000 x *g* in a JA25.50 rotor for 45 min, and the clarified lysate was applied to Strep-Tactin
651 superflow plus cartridges (Qiagen). Immobilised proteins were washed with lysis buffer
652 followed by wash buffer 2 (20 mM HEPES pH 7.0, 150 mM NaCl, 1 mM TCEP) and were
653 eluted using wash buffer 2 containing 2.5 mM d-desthiobiotin.

654 The 6xHis-SUMO tag was removed from the CENP-C$^{Mif2_1\text{-}63}$ and CENP-C$^{Mif2_1\text{-}63}$-TS by
655 overnight incubation with recombinant Ulp1 protease carrying a 6xHis tag at 4 ˚C. Cleaved
656 protein was isolated from the protease by a reverse IMAC purification step. After diluting the
657 salt concentration to 100 mM, the reverse IMAC flow through was applied to a Resource S
658 cation exchange column (Cytiva) for further purification. CENP-C$^{Mif2_1\text{-}63}$ was eluted using
659 buffer containing 20 mM HEPES pH 7.5, 300 mM NaCl, 1 mM TCEP. CENP-C$^{Mif2_1\text{-}63}$-TS
660 was eluted using buffer containing 20 mM HEPES pH 7.5, 1 mM TCEP, and a gradient from
661 100 mM to 1000 mM NaCl over 15 column volumes. CENP-C$^{Mif2_1\text{-}63}$ and CENP-C$^{Mif2_1\text{-}63}$-
662 TS were concentrated and further purified by application to a Superdex 75 16/60 column
663 (Cytiva) equilibrated in KMN buffer. Peak CENP-C$^{Mif2_1\text{-}63}$ fractions were pooled,
664 concentrated, and flash frozen using liquid nitrogen.

665 CENP-QU was expressed and purified according to the method described in (Dendooven et
666 al., 2023).

667 <u>Reconstitution and GraFix crosslinking the *S. cerevisiae* KMN complex for cryo-EM</u>

668 The *S. cerevisiae* KMN complex was reconstituted and crosslinked for cryo-EM using a
669 GraFix protocol (Stark, 2010). Two buffers were used to prepare 10–30% continuous glycerol
670 gradients (4 mL total volume) with an additional 0.0–0.2% glutaraldehyde component using a
671 gradient master: buffer A contained 20 mM HEPES pH 7.5, 150 mM NaCl, 10% glycerol, 1

mM TCEP, and buffer B contained 20 mM HEPES pH 7.5, 150 mM NaCl, 30% glycerol, 1 mM TCEP, 0.2% glutaraldehyde. Stocks of Ndc80c and a Knl1c:Mis12c^{Mtw1c} complex that contained Knl1$^{Spc105_HB\text{-}RWD}$ (K$^{HB\text{-}RWD}$M) were thawed on ice, and diluted and mixed at a 4 μM equimolar (1:1) ratio in KMN buffer. The mixture was incubated for 30 min at 4 ˚C to reconstitute the KMN complex.

200 pmol (50 μL volume) of reconstituted K$^{HB\text{-}RWD}$MN complex was applied to each glycerol gradient, and gradients were subsequently subjected to centrifugation at 50,000 rpm in a SW 60 Ti Swinging-Bucket Rotor (Beckman Coulter) for 16 h. Glycerol gradients were manually fractionated into 250 μL fractions, and unreacted glutaraldehyde was quenched by pipetting the fractions over a solution of 1 M Tris.HCl pH 7.5 such that the final concentration of Tris.HCl in each fraction was 20 mM. Fractions encompassing the gradient volume 2.00–2.75 mL were pooled, glycerol content was reduced by application to Zeba spin desalting columns equilibrated in KMN buffer, and the protein complex was concentrated to a final concentration of 0.8 mg/mL.

Cryo-EM grid preparation

Cryo-EM grids were glow discharged in an Edwards S150B glow discharger for 60 s at setting 6, 20–25 Ma, 1.2 kV and 0.2 mBar (0.15 Torr) immediately prior to application of sample. 3 μL of reconstituted and crosslinked K$^{HB\text{-}RWD}$MN complex was applied to freshly glow discharged UltrAuFoil 300 mesh gold R1.2/1.3 grids (Quantifoil Micro Tools). Grids were mounted in a FEI Vitrobot mark III humidity chamber (maintained at 4 ˚C, 100% humidity), blotted with Whatman filter paper I (2 s blotting time, -7 blotting force), and vitrified in liquid ethane.

Cryo-EM data acquisition

Cryo-EM movies were collected on a Thermo Fisher Scientific Titan Krios 1 microscope operating at 300 keV using a Gatan K3 camera equipped with a Gatan energy filter. Movies were collected at x105,000 magnification (pixel size 0.825 Å px^{-1}) with a 1.75 s exposure and 15.6 e^{-}/px/s fluence, providing a total dose of 40 e^{-}/Å^{2}, and were split into 40 frames. A series of movies were collected over a range of defoci from -1.4 μm to -3.0 μm, at an interval of 0.4 μm. Data acquisition was performed using aberration-free image shifts (AFIS) as employed in the Thermo Fisher Scientific 'EPU' automated data acquisition software.

The limited resolution (6.5 Å) of the consensus structure of the KMN junction complex was likely caused by heterogeneity at either end of the Mis12c^{Mtw1c} stalk domain (Figure S2Di) that we were unable to resolve with extensive 2D and 3D classification and 3D variability analyses. To obtain a higher-resolution structure of subdomains, we subtracted the signal arising from the poorly resolved Mis12c^{Mtw1c} head 2 domain (Figure S2Dii) and subjected the subtracted particles to multibody refinement using masks encompassing the two domains forming the apex and base of the Mis12c^{Mtw1c} stalk domain (Figure S2Diii). This yielded reconstructions showing the Knl1c and Spc24:Spc25 RWD domains at the apex of the Mis12c^{Mtw1c} stalk, and head 1 at the base of the Mis12c^{Mtw1c} stalk, at global resolutions of 4.8 Å and 4.9 Å, respectively (Figure S2Diii). The local resolutions of the reconstructions reached 4.2 Å and 4.5 Å in the central regions of the apex and base density maps, respectively (Figure S2E, F), which were sufficient to interpret with an AlphaFold2 (AF2)-predicted model (Jumper et al., 2021). To obtain a composite map of the KMN junction complex, we docked the cryo-EM maps of the apex and base multi-bodies into the consensus cryo-EM map (Figure 1B). This composite map was used to build a model of the *S. cerevisiae* KMN junction complex using AF2 structure predictions and Isolde model refinement, as detailed in Methods (Croll, 2018; Jumper et al., 2021).

Cryo-EM data processing

Alignment of micrograph raw movie frames and correction to a single micrograph image was performed using UCSF MotionCor2 as implemented in RELION (Kimanius et al., 2021; Zheng et al., 2017). The contrast transfer function (CTF) of each motion corrected micrograph was estimated using CTFFIND-4.1 as implemented in RELION (Kimanius et al., 2021; Rohou and Grigorieff, 2015). Manual particle picking of 10 micrographs was used to train a Topaz model that was used to pick the entire dataset of 26,390 micrographs (Bepler et al., 2019) (Figure S2 and Table S1). The particles picked by the first Topaz model were curated by two successive rounds of 2D classification in CryoSPARC (Punjani et al., 2017). 2D classification in CryoSPARC was always performed using batch sizes of 400 and 40 online-em iterations. Particles classified into class averages that resembled KMN were selected and used to train a second Topaz model in RELION that was once again used to pick all 26,390 micrographs.

Particles were separated into six distinct sets, based on the appearance of 2D class averages, using two successive rounds of 2D classification in CryoSPARC. Each set of particles was

used to generate an *ab initio* model in CryoSPARC, yielding one KMN model, one additional protein model, and four decoy noise models. All six *ab initio* models were used as references for a noise decoy classification step using the heterogeneous refinement job type in CryoSPARC. Particles corresponding to the model that resembled the KMN complex were subjected two further successive rounds of 2D classification, yielding 321,078 particles that corresponded to 2D class averages that resembled KMN. This set of particles was further processed in RELION for all subsequent steps. All 3D refinement and 3D classification jobs in RELION used Blush regularization, as implemented in RELION 5.0 (Kimanius et al., 2021; Kimanius et al., 2024).

The particles were used to generate an *ab initio* model, against which they were refined (successive unmasked and masked refinements) to reconstruct a cryo-EM density map with a resolution of 7.5 Å and discontinuous density for the Spc24 and Spc25 RWD domains and the Mis12c^{Mtw1c} head 2 domain.

To better resolve the Spc24 and Spc25 RWD domains, particles were subjected to focussed 3D classification without alignment using a mask encompassing the CC3 region of the Mis12c^{Mtw1c} stalk domain, the Knl1c RWD domains, and the Spc24 and Spc25 RWD domains, and a *T* value of 25. A set of 113,688 particles corresponding to two 3D classes with improved continuity of the Spc24 and Spc25 RWD domain density were refined to reconstruct a cryo-EM density map with a resolution of 6.5 Å and discontinuous density for the Mis12c^{Mtw1c} head 2 domain. Signal corresponding to the Mis12c^{Mtw1c} head 2 domain was subtracted from the particle images, and the subtracted particles were refined to reconstruct a cryo-EM density map with a resolution of 6.0 Å. Two non-overlapping masks were generated for multibody refinement: one encompassed part of the CC2 region of the Mis12c^{Mtw1c} stalk domain, the CC3 region of the Mis12c^{Mtw1c} stalk domain, the Knl1c RWD domains, and the Spc24 and Spc25 RWD domains ('apex mask 1'), whilst the other encompassed the Mis12c^{Mtw1c} head 1 domains, the CC1 region of the Mis12c^{Mtw1c} stalk domain, and the remaining segment of the CC2 region of the Mis12c^{Mtw1c} stalk domain ('base mask 1'). Multibody refinement using these masks yielded two cryo-EM density maps with global resolutions (GS-FSC) of 4.8 Å ('apex body 1') and 4.9 Å ('base body 1'), respectively. The local resolutions of the reconstructions reached 4.2 Å and 4.5 Å in the central regions of the apex and base density maps, respectively (Figure S2E, F), which were sufficient to interpret with an AlphaFold2 (AF2)-predicted model (Jumper et al., 2021). To obtain a composite map of the KMN junction complex, the cryo-EM maps of the apex and base multi-bodies were

767 docked into the consensus cryo-EM map (Figure 1B). This composite map was used to build
768 a model of the *S. cerevisiae* KMN junction complex using AF2 structure predictions and
769 Isolde model refinement (Croll, 2018; Jumper et al., 2021) as detailed below in 'Cryo-EM
770 molecular model building'.

771 To better resolve the Mis12c^{Mtw1c} head 2 domain, particles were subjected to focussed 3D
772 classification without alignment using a mask encompassing the Mis12c^{Mtw1c} head 1 and head
773 2 domains and the CC1 region of the Mis12c^{Mtw1c} stalk domain (Figure S4 and Table S1). A
774 set of 18,160 particles corresponding to a 3D class with continuous density for the
775 Mis12c^{Mtw1c} head 2 domain were refined to reconstruct a cryo-EM density map with a
776 resolution of 7.5 Å that retained discontinuous density for the Spc24 and Spc25 RWD
777 domains. Signal corresponding to the Spc24 and Spc25 RWD domains was subtracted from
778 the particle images, and the subtracted particle images were used to reconstruct a cryo-EM
779 density map with a resolution of 7.2 Å. Two non-overlapping masks were generated for
780 multibody refinement: one encompassed part of the CC2 region of the Mis12c^{Mtw1c} stalk
781 domain, the CC3 region of the Mis12c^{Mtw1c} stalk domain, and the Knl1c RWD domains
782 ('apex mask 2'), whilst the other encompassed the Mis12c^{Mtw1c} head 1 and head 2 domains,
783 the CC1 region of the Mis12c^{Mtw1c} stalk domain, and the remaining segment of the CC2
784 region of the Mis12c^{Mtw1c} stalk domain ('base mask 2'). Multibody refinement using these
785 masks reconstructed a cryo-EM density map for the Mis12c^{Mtw1c} head 1 and head 2 domains
786 and relevant sections of the stalk domain with a global resolution (GS-FSC) of 6.5 Å ('base
787 body 2').

788 <u>Cryo-EM molecular model building</u>

789 AF2 multimer structure predictions of Mis12c^{Mtw1c}:Spc24:Spc25 and Knl1c:Mis12c^{Mtw1c},
790 performed using full-length, wild type proteins apart from Knl1^{Spc105} (from which residues 1-
791 444 were excluded) and Dsn1 (from which residues 1-278 were excluded), were used to build
792 a model for the KMN junction complex. A composite map of the KMN junction complex was
793 obtained by docking 'apex body 1' and 'base body 1' into the cryo-EM density map
794 reconstructed by the preceding refinement and used for model building.

795 The AF2 structure predictions were divided into five regions for model building. 'Region
796 one', corresponding to Spc24 and Spc25 RWD domains interacting with Mis12$^{Mtw1_Spc24\text{-}helix}$
797 and Dsn1$^{Cterm\text{-}helix}$ helical motifs, comprised Spc24$^{143\text{-}213}$, Spc25$^{124\text{-}221}$, Mis12$^{Mtw1_228\text{-}252}$, and
798 Dsn1$^{556\text{-}576}$. 'Region two', corresponding to the RWD domains of ZWINT^{Kre28} and Knl1^{Spc105}

interacting with the Mis12$^{Mtw1_Cterm\text{-}helix}$ and Nnf1$^{Cterm\text{-}helix}$ helical motifs, comprised Knl1$^{Spc105_719\text{-}917}$, ZWINT$^{Kre28_280\text{-}368}$, Mis12$^{Mtw1_274\text{-}289}$, and Nnf1$^{184\text{-}201}$. 'Region three', corresponding to all of the CC3 and most of the CC2 regions of the Mis12c^{Mtw1c} stalk domain, comprised Dsn1$^{483\text{-}547}$, Nnf1$^{139\text{-}180}$, Nsl1$^{143\text{-}216}$, and Mis12$^{Mtw1_132\text{-}222}$. 'Region four', corresponding to the remainder of the CC2 and all of the CC1 regions of the Mis12c^{Mtw1c} stalk domains, comprised Dsn1$^{431\text{-}482}$, Nnf1$^{115\text{-}138}$, Nsl1$^{97\text{-}142}$, and Mis12$^{Mtw1_116\text{-}131}$. 'Region 5', comprising the Mis12c^{Mtw1c} head 1 domain, comprised Nnf1$^{1\text{-}114}$ and Mis12$^{Mtw1_1\text{-}115}$. Isolde, as implemented in Chimera X, was used to remodel and refine these five regions of the AF2 structure predictions into the composite map of the KMN junction complex (Croll, 2018; Goddard et al., 2018).

C-terminal residues of Nnf1, Mis12^{Mtw1}, Dsn1, and Nsl1 in 'region five' and 'region four' were manually reconnected with the N-terminal residue of the corresponding chain in 'region four' and 'region three', respectively, and refined into the density in Coot (Emsley et al., 2010) to yield 'region tff'. The model comprising 'region one', 'region two', and 'region tff' was subsequently refined and remodelled into the composite map using Isolde to yield the final model of the KMN junction complex.

To build the experimental model of the *S. cerevisiae* KMN junction complex with head 2 we docked the KMN junction complex (without head 2) and the AF2 prediction of the *S. cerevisiae* Mtw1^{Mis12} head2 domain (Dsn1 residues 259-353 and Nsl1 residues 1-84), and the AF2 prediction of *Kl*Mtw1^{Mis12c}, into the 6.5 Å KMN junction base body 2 cryo-EM map (Figure S4C and Table S1). The *Kl*Mtw1^{Mis12c} model accounted for nearly all density in the cryo-EM map, whereas for the *S. cerevisiae* model of head 2, some density regions were not assigned, mainly a helical-like density associated with Dsn1 head 1 (Dsn1^{AI}, *Sc* residues 229-255), the Dsn1 CC1-head2 linker (*Sc* residues 354-365) and the Nsl1 CC1-head2 linker (*Sc* residues 85-96) (Figure S5A, B, E). We used the *Kl*Mtw1^{Mis12c} model (Figure S5G, H) to guide complete building of an experimental model of *Sc*Mtw1^{Mis12c} (Figure 6B, C).

Model refinement

Refinement was performed using the Phenix package (Liebschner et al., 2019) (Table S1).

AlphaFold2 structure predictions

Local installations of AlphaFold2 (Jumper et al., 2021) were used for all protein structure predictions in this study. The Colabfold implementation AF2 (Mirdita et al., 2022) of AF2

830 was used for all structure predictions other than for the *Kluyveromyces lactis* Mis12c^{Mtw1c}
831 (*Kl*Mis12c^{Mtw1c}), which used the Colabfold 3 version. Unless otherwise stated, wild-type,
832 full-length protein sequences deposited in Uniprot were used for all protein structure
833 predictions.

834 Isothermal titration calorimetry experiments

835 Dsn1$^{228-254}$ and Dsn1$^{228-254,S240E,S250E}$ peptides were synthesised by Alta BioScience with N-
836 terminal acetylation and C-terminal GSAW extension and amidation. The final sequence of
837 Dsn1$^{228-254}$ was PHYIQRTRERKKSISHSQRGRRLSMLASGSAW; and Dsn1$^{228-254,S240E,S250E}$
838 was PHYIQRTRERKKSISHSQRGRRLEMLASGSAW. All protein complexes and peptides
839 used in a given experiment were dialysed for a minimum of 16 h and/or buffer exchanged by
840 size exclusion chromatography into the same batch of ITC buffer (25 mM HEPES pH 7.5,
841 100 mM NaCl, 1 mM TCEP). All experiments were performed using an Auto-iTC200
842 instrument (Malvern Instruments) at 25 ˚C. In each experiment, 360 µL of protein complex
843 was pipetted into the calorimeter cell. The protein complex loaded into the calorimeter cell
844 contained Knl1c:Mis12c^{Mtw1c} with Knl1$^{Spc105_HB\text{-}RWD}$ and Dsn1$^{\Delta 1\text{-}257}$ and either wildtype
845 Mis12^{Mtw1} (K$^{HB\text{-}RWD}$M$^{Dsn1\Delta 257}$) or Mis12^{Mtw1_E69A,E73A,E77A} mutant (K$^{HB\text{-}RWD}$M$^{Dsn1\Delta 257_Mis12\text{-}}$
846 ^{3A}). Wild-type constructs of all other Knl1c and Mis12c^{Mtw1c} subunits were included. Titration
847 of either the Dsn1$^{228-254}$ or Dsn1$^{228-254,S240E,S250E}$ peptide into the cell was then performed by
848 an additional injection of 0.5 µL, followed by 19 further injections of 2.0 µL each. Heat
849 arising from the initial injection was discarded, and the MicroCal PEAQ-ITC analysis
850 software 1.0.0.1258 (Malvern instruments) was subsequently used to fit the change in the
851 amount of heat released, integrated over the entire titration, to a single-site binding model.
852 Concentrations of the protein complex and peptide used for each experiment are provided in
853 the relevant figure panel. Titrations were performed in duplicate or triplicate and reported K_D
854 and n values were calculated as an average from all replicate results.

855 CENP-U$^{Ame1_1\text{-}33}$ (MDRDTKLAFRLRGSHSRRTDDIDDDVIVFKTPNW-amide), CENP-
856 U$^{Ame1_1\text{-}33\text{-}Mut}$ (MDRDTKLAFRLRGSHSRRTDDIDDAAAVAKAPNW-amide) and CENP-
857 C$^{Mif2_1\text{-}38}$ (MDYMKLGLKSRKTGIDVKQDIPKDEYSMENIDDFFKDD-amide) peptides
858 were synthesized by Alta BioScience. Peptides and proteins (K$^{HB\text{-}RWD}$M and K$^{HB\text{-}RWD}$M^{2E})
859 were dialysed for 16 h at 4 ˚C against a buffer of 25 mM HEPES (pH 7.5), 100 mM NaCl, 0.5
860 mM TCEP. The ITC experiments were performed in triplicate as described above except at 20
861 ˚C.

862 Investigation of the function of Mis12c^{Mtw1c} motifs that form interfaces with Knl1c

863 To test the effect of deleting the Mis12c^{Mtw1c} motifs that form interfaces with Knl1c on
864 Mis12c^{Mtw1c} assembly and interaction with Ndc80c, 4 µM concentration of wildtype
865 Mis12c^{Mtw1c} or one of the three Mtw1c mutants (Mis12c$^{Mtw1c_Mis12\Delta C}$, contained
866 Mis12$^{Mtw1_\Delta 272\text{-}C}$; Mis12c$^{Mtw1c_Nnf1\Delta C}$, contained Nnf1$^{\Delta 180\text{-}C}$; Mis12c$^{Mtw1c_Mis12\Delta C\text{-}Nnf1\Delta C}$:
867 contained Mis12$^{Mtw1_\Delta 272\text{-}C}$ and Nnf1$^{\Delta 180\text{-}C}$) were either individually diluted into KMN buffer,
868 or mixed with 4 µM concentration of wildtype Ndc80c in KMN buffer. Mixtures of Ndc80c
869 and wildtype or mutant Mis12c^{Mtw1c} were incubated on ice for 30 min to reconstitute the
870 complex. 100 µL of individual protein complexes or reconstitution mixtures were loaded onto
871 a Superose 6 3.2/300 size exclusion chromatography column (Cytiva) and 100 µL eluate
872 fractions were collected. Aliquots of each eluate fraction were mixed 1:1 (volume/volume)
873 with 2xLDS-PAGE loading buffer (Thermo Fisher Scientific), supplemented with DTT,
874 boiled for 3 min at 95 ˚C, and analysed by SDS-PAGE.

875 To test the effect of deleting the Mis12c^{Mtw1c} motifs that form interfaces with Knl1c on the
876 interaction between Knl1c and Mis12c^{Mtw1c}, suspension cultures of High-5 insect cells were
877 infected with one of two P3 suspension cultures, or two P3 cultures in combination, that were
878 amplifying one of two sets of viruses. The first virus encoded ZWINT^{Kre28_RWD} fused to a C-
879 terminal twin-strep-tag II and Knl1^{Spc105_RWD} fused to a N-terminal tag comprising tandem
880 maltose binding protein (MBP) and monomeric enhanced green fluorescent protein (mEGFP)
881 tags. The second set of viruses encoded either wildtype Mis12c^{Mtw1c}, or one of the
882 Mis12c$^{Mtw1c_Mis12\Delta C}$, Mis12c$^{Mtw1c_Nnf1\Delta C}$, or Mis12c$^{Mtw1c_Mis12\Delta C\text{-}Nnf1\Delta C}$ mutants. All viruses
883 encoding Mis12c^{Mtw1c} contained genes that expressed Dsn1$^{\Delta 1\text{-}278}$. The insect cell cultures
884 were harvested 48 h after infection, when cell viabilities had dropped to 70-75%.

885 All subsequent steps were performed at 4 ˚C or on ice. Cells were lysed by sonication in a
886 lysis buffer containing 50 mM HEPES pH 8.5, 200 mM NaCl, 8 mM benzamidine, 7.5%
887 glycerol, 1 mM TCEP, 0.5 mM EDTA, 0.2 mM PMSF that was supplemented with cOmplete
888 EDTA-free protease inhibitor tablets and benzonase. The lysate was cleared by
889 ultracentrifugation at 38,000 x *g* for one h in a JA-25.50 rotor. A sample of the cleared
890 supernatant was withdrawn and mixed 1:9 (volume/volume) with lysis buffer, mixed with 10
891 volume equivalents of 2xLDS-PAGE loading buffer (Thermo Fisher Scientific) supplemented
892 with DTT, and boiled for 5 min at 95 ˚C for analysis as an input sample by SDS-PAGE.
893 Cleared supernatants were subsequently filtered and incubated whilst rolling with 0.5 mL of a

894 50% slurry of Strep-Tactin Superflow plus resin (Qiagen) in a wash buffer containing 50 mM
895 HEPES pH 8.0, 200 mM NaCl, 5% glycerol, 0.5 mM EDTA, 1 mM TCEP for 90 min. Resin
896 was collected by centrifugation at 500 x *g* for 3 min and washed with 10 mL of wash buffer.
897 Resin washes were repeated, as above, a further four times. Resin was collected a final time
898 by centrifugation, as above, and bound complexes were eluted with wash buffer containing
899 2.5 mM d-desthiobiotin. The resin was collected by centrifugation, as above, and 10 μL of
900 eluate was withdrawn and mixed with an equal volume of 2xLDS-PAGE loading buffer
901 (Thermo Fisher Scientific) that was supplemented with DTT. This sample of eluate was then
902 boiled for 5 min and analysed by SDS-PAGE.

903 Investigation of Dsn1 N-terminal intrinsically disordered domain function in Mis12c^{Mtw1c}
904 auto-inhibition

905 To test the effect of deleting or mutating regions of the Dsn1 N-terminal disordered domain
906 on Mis12c^{Mtw1c} auto-inhibition, 4 μM concentrations of Knl1c:Mis12c^{Mtw1c} complexes
907 containing Knl1$^{Spc105_HB\text{-}RWD}$ and different Dsn1 constructs were mixed with 4 μM
908 concentrations of either CENP-C$^{Mif2_1\text{-}63}$ or CENP-QU in KMN buffer. Knl1c:Mis12c^{Mtw1c}
909 complexes used contained one of the following Dsn1 constructs: K^{HBRWD}M, contained full-
910 length and wildtype Dsn1; K$^{HB\text{-}RWD}$M^{S240E,S250E}, contained Dsn1^{S240E,250E}; K$^{HB\text{-}RWD}$M$^{Dsn1\Delta226}$,
911 contained Dsn1$^{\Delta1\text{-}226}$; K$^{HB\text{-}RWD}$M$^{Dsn1\Delta257}$, contained Dsn1$^{\Delta1\text{-}257}$; K$^{HB\text{-}RWD}$M$^{Dsn1\Delta226,S240E,S250E}$,
912 contained Dsn1$^{\Delta1\text{-}226,S240E,S250E}$. Protein mixtures were incubated together on ice for 30 min to
913 attempt to reconstitute a protein complex. 100 μL of individual proteins or protein complexes
914 or reconstitution mixtures were loaded onto a Superose 6 3.2/300 size exclusion
915 chromatography column (Cytiva) equilibrated in (20 mM HEPES pH 7.5, 150 mM NaCl, 1
916 mM TCEP) and 100 μL eluate fractions were collected. Aliquots of each indicated eluate
917 fraction was mixed 1:1 (volume/volume) with 2xLDS-PAGE loading buffer supplied by
918 Thermo Fisher Scientific, supplemented with DTT, boiled for 3 min at 95 ˚C, and analysed by
919 SDS-PAGE.

920 Yeast strain construction

921 We constructed *S. cerevisiae* strains encoding the OsTir1 ubiquitin ligase at the URA3 locus
922 and a mAID$_3$-FLAG$_5$ C-terminal tag at either the endogenous NNF1 (encoding *Nnf1*) or
923 MTW1 (encoding *Mis12^{Mtw1}*) loci. Yeast strains constructed for this study are listed in Table
924 S2. To construct strains encoding Mis12^{Mtw1}-mAID$_3$-FLAG$_5$ (*MTW1-mAID$_3$-FLAG$_5$* allele) or
925 Nnf1-mAID$_3$-FLAG$_5$ (*NNF1-mAID$_3$FLAG$_5$* allele), a degron cassette encoding mAID$_3$-

926 $FLAG_5$ and a KanMX gene that provided resistance to G418 were amplified from plasmid
927 pST1933 (Tanaka et al., 2015) through a polymerase chain reaction (PCR) that used Q5
928 polymerase and oligonucleotide primers containing 48 bp 5' extensions with homology to the
929 relevant locus in the yeast genome. BY26972 strain yeast cells (Table S2) from an
930 exponentially growing suspension culture were transformed with the cassette according to the
931 previously detailed LiAc protocol (Gietz and Schiestl, 2007). In brief, cells were harvested by
932 centrifugation, washed thrice with sterile Millipore water (MPW), and incubated with 360 µL
933 transformation buffer (100 mM lithium acetate, 33% PEG 3350, 100 µg salmon sperm DNA)
934 containing the degron cassette. Cells were transformed with the cassette through a 45 min
935 heat shock at 42 ˚C, and allowed to recover by standing in 1 mL of YEPD medium for 3 h at
936 22 ˚C. Transformants were then selected by plating yeast cells on YEPD agar containing 500
937 µg/mL G418 (Sigma, A1720-5G) and grown at 30 ˚C for 3–4 days. Individual colonies were
938 picked and restreaked on fresh YEPD agar containing 500 µg/mL G418 twice, successively.
939 Integration of the cassette was then screened by PCR amplification using Q5 polymerase and
940 two primers directed against the 3' end of the relevant gene and an internal region of the
941 degron cassette. PCR products obtained by this method were sequenced to validate in-frame
942 integration of the DNA sequences encoding the $mAID_3$-$FLAG_5$ tags at the 3' end of the
943 relevant gene.

944 Strains expressing $Mis12^{Mtw1}$-$mAID_3$-$FLAG_5$ or Nnf1-$mAID_3$-$FLAG_5$ and an allele to be
945 tested for its ability to rescue cell death were constructed as follows. Yeast strains expressing
946 $Mis12^{Mtw1}$-$mAID_3$-$FLAG_5$ or $Nnf1^{1}$-$mAID_3$-$FLAG_5$ were transformed, as above, with
947 *pRS304* (encoding *MTW1* alleles) or *pRS305* (encoding *NNF1* alleles) plasmids that were
948 cleaved with a restriction enzyme in a single site within the *LEU2* (*pRS304* plasmids) or
949 *TRP1* (*pRS305* plasmids) selection marker. The plasmids contained the following alleles
950 encoding the listed gene products: *MTW1*, full-length and wildtype $Mis12^{Mtw1}$; $mtw1^{\Delta C}$,
951 $Mis12^{Mtw1_\Delta 272\text{-}C}$, *NNF1*, full-length and wildtype Nnf1; $nnf1^{\Delta C}$, $Nnf1^{\Delta 180\text{-}C}$. Transformants
952 were selected for by plating yeast cells on leucine dropout (*MTW1* or $mtw1^{\Delta C}$ transformants)
953 or tryptophan dropout (*NNF1* or $nnf1^{\Delta C}$ transformants) agar media containing 500 µg/mL
954 G418. Integration of the cassette at the *LEU2* or *TRP1* locus was screened using two PCR
955 reactions that amplified across the 5' and 3' recombination junctions. The first PCR used a
956 pair of oligonucleotide primers targeted against a region of the genome 5' of *LEU2* or *TRP1*
957 and against an internal region of the integrated cassette, and the second PCR used a pair of
958 primers targeted against a region of the genome 3' of *LEU2* or *TRP1* and against another

959 internal region of the cassette. Positive transformants were stored in 50% glycerol at -80 °C
960 for later use.

961 All strains grew well on YEPD plates in the absence of IAA, showing that the incorporation
962 of the $mAID_3$-$FLAG_5$ tag at the endogenous MTW1 and NNF1 loci, and rescue alleles at the
963 exogenous loci, did not adversely affect cell growth (Figure S3E).

964 Auxin depletion assays

965 10 mL suspension cultures of each yeast strain were grown overnight at 30 °C. The optical
966 density at 600 nm of each suspension culture was measured in triplicate, yeast cells were
967 subsequently diluted to OD_{600nm} = 0.1, and then serially diluted 1:9 (volume/volume) over 4
968 further dilutions. 4 µL of each dilution was then applied to agar plates containing either
969 YEPD medium, or YEPD medium and 0.5 mM indole-3-acetic acid (IAA). Cells were grown
970 at 30 °C for 3 days and imaged.

971 Western blotting

972 To validate expression levels of the gene products of the *MTW1* ($Mis12^{Mtw1}$) and *NNF1*
973 (Nnf1) alleles integrated at ectopic sites, 40 mL of each cell culture was grown in YEPD until
974 the culture reached an OD_{600nm} between 0.7 and 2.0. At this point, $1x10^7$ (*MTW1-mAID$_3$-*
975 *FLAG$_5$* strains) or $1.4x10^7$ (*NNF1-mAID$_3$-FLAG$_5$* strains) cells were withdrawn from the
976 culture and processed for western blotting as described below.

977 Depletion of *MTW1-mAID$_3$-FLAG$_5$* and *NNF1-mAID$_3$-FLAG$_5$* gene products by addition of
978 IAA was monitored and validated by growing 40 mL suspension cultures of each strain in
979 YEPD medium until the culture attained an OD_{600nm} of between 0.7 and 2.0. This was
980 followed by addition of either IAA to a final concentration of 0.5 mM, or of an equal volume
981 of phosphate buffered saline (PBS) as a negative control. A volume of suspension culture
982 containing $1x10^7$ *MTW1-mAID$_3$-FLAG$_5$* strains) or $1.4x10^7$ (*NNF1-mAID$_3$-FLAG$_5$*) cells was
983 then withdrawn from each culture at the indicated time points and processed for western
984 blotting as described below.

985 All subsequent steps were performed at 22 °C, unless otherwise indicated. Yeast cells were
986 collected by centrifugation at 3,000 x *g* for 3 min, resuspended in 1 mL of sterile Millipore
987 water (MPW), and pelleted by centrifugation at 12,000 x *g* for 1 min. Whole cell extracts
988 were then prepared by incubation of the cell pellets in 50 µL of 0.2 M NaOH for 5 min,
989 centrifugation for 1 min at 12,000 x *g*, a wash of the cell pellet with 1 mL of MPW, and a

990 final collection of the pellet by centrifugation as above. Pellets were then boiled for 3 min at
991 95 °C in 50 μL of 1xLDS-PAGE loading buffer supplemented with DTT. The pellet was
992 collected by centrifugation, and 10 μL of each supernatant was applied to an SDS-PAGE gel
993 to separate proteins through application of a constant 210 V for 45 min. Proteins were
994 transferred from the SDS-PAGE gel onto a TransBlot Turbo minigel membrane using a
995 Trans-blot Turbo transfer system. Membranes were blocked with 3% milk suspension (*NNF1*
996 gene product blots) or 5% milk suspension (*MTW1* gene product blots) in PBS-T (Phosphate
997 buffered saline containing 0.2% Tween-20) for 30 min at 22 °C. Membranes were then probed
998 with the primary antibody detailed below overnight at 4 °C in PBS-T to detect the protein of
999 interest. To detect *MTW1-mAID*$_3$*-FLAG*$_5$and *NNF1-mAID*$_3$*-FLAG*$_5$ gene products, a 1:1000
1000 (volume/volume) dilution of anti-FLAG antibody (Cell Signalling, D6W5B) was used. To
1001 detect *NNF1-V5*$_3$ and *nnf1*$^{\Delta C}$*-V5*$_3$ or *MTW1-HA*$_3$ and *mtw1*$^{\Delta C}$ expressed from the ectopically
1002 integrated loci, 1:3333 dilutions of anti-V5 (Proteintech, 14440-1-AP) or anti-HA (Abcam,
1003 ab1424) antibodies, respectively, were used. To detect alpha tubulin as a loading control, anti-
1004 α-tubulin (Bio-Rad, MCA78G) antibody was used.

1005 Membranes were washed four times with PBS-T before incubation with a 1:3333
1006 (volume/volume) dilution of HRP-conjugated secondary antibody in PBS-T by rolling at 21
1007 °C for 1.5–2.5 h. Membranes were washed a further four times with PBS-T before
1008 visualisation of the secondary antibody using chemiluminescence using the ECL Prime
1009 Western blotting detection kit (Amersham) and imaging using a ChemiDoc imaging system
1010 (Bio-Rad).

1011 Multiple sequence alignment

1012 Multiple sequence alignments were performed with Clustal Omega using default settings and
1013 sequences full-length, wildtype protein sequences deposited in Uniprot unless otherwise
1014 indicated (Sievers et al., 2011). Sequence alignments were visualised using the Jalview
1015 workbench using a conservation score of 10 (Waterhouse et al., 2009).

1016 Crosslinking mass-spectrometry

1017 Protein cross linking reactions on the *S. cerevisiae* K$^{HB\text{-}RWD}$M complex (100 μL at 0.5
1018 mg/mL) were carried out with sulfo-SDA (2 mM concentration). Sulfo-SDA and the protein
1019 complex were mixed and incubated on ice for 5 min before being cross linked for 10 sec with
1020 365 nm UV radiation from a home build UV LED setup. Crosslinking reactions were

1021 quenched with the addition of ammonium bicarbonate to a final concentration of 50 mM. The
1022 quenched solution was reduced with 5 mM DTT and alkylated with 20 mM iodoacetamide.
1023 The SP3 protocol, as described (Batth et al., 2019; Hughes et al., 2019), was used to clean-up
1024 and buffer exchange the reduced and alkylated protein. In brief, for the SP3 protocol; proteins
1025 are washed with ethanol using magnetic beads for protein capture and binding. The proteins
1026 were resuspended in 100 mM NH_4HCO_3 and were digested with trypsin (Promega, UK) at an
1027 enzyme-to-substrate ratio of 1:20, and protease max 0.1% (Promega, UK). Digestion was
1028 carried out overnight at 37 °C. Clean-up of peptide digests was carried out with HyperSep
1029 SpinTip P-20 (Thermo Fisher Scientific) C18 columns, using 60% Acetonitrile as the elution
1030 solvent. Peptides were then evaporated to dryness *via* Speed Vac Plus (Savant, USA).

1031 Dried peptides were resuspended in 30% acetonitrile and were fractionated *via* SEC using a
1032 Superdex 30 Increase 3.2/300 column (Cytiva) at a flow rate of 20 µL/min using 30% (v/v)
1033 ACN 0.1 % (v/v) TFA as a mobile phase. Fractions are taken every 5 min, and the 2nd to 7th
1034 fractions containing cross linked peptides are collected. Dried peptides were suspended in 3%
1035 (v/v) acetonitrile and 0.1 % (v/v) formic acid and analysed by nano-scale capillary LC-
1036 MS/MS using an Ultimate U3000 HPLC to deliver a flow of 300 nL/min. Peptides were
1037 trapped on a C18 Acclaim PepMap100 5 µm, 0.3 µm x 5 mm cartridge (Thermo Fisher
1038 Scientific) before separation on Aurora Ultimate C18, 1.7 µm, 75 µm x 25 cm (Ionopticks,
1039 Melbourne). Peptides were eluted on optimised gradients of 90 min and interfaced *via* an
1040 EasySpray ionisation source to a tribrid quadrupole Orbitrap mass spectrometer (Orbitrap
1041 Eclipse, Thermo Fisher Scientific) equipped with FAIMS. MS data were acquired in data
1042 dependent mode with a Top-25 method, high resolution scans full mass scans were carried
1043 out (R = 120,000, *m/z* 400 – 1550) followed by higher energy collision dissociation (HCD)
1044 with stepped collision energy range 21, 30, 34 % normalised collision energy. The tandem
1045 mass spectra were recorded (R=60,000, isolation window *m/z* 1, dynamic exclusion 50 s).
1046 Mass spectrometry measurements were cycled for 3 s durations between FAIMS CV -45, and
1047 -60 V.

1048 <u>Crosslinking mass-spectrometry data analysis</u>

1049 Xcalibur raw files were converted to MGF files using ProteoWizard and cross links were
1050 analysed by XiSearch (Chambers et al., 2012; Mendes et al., 2019). Search conditions used 3
1051 maximum missed cleavages with a minimum peptide length of 5. Variable modifications used
1052 were carbmidomethylation of cysteine (57.02146 Da) and methionine oxidation (15.99491

Da). False discovery rate was set to 5%. Crosslinking mass-spectrometry data was visualised and analysed using XiVIEW (Combe et al., 2024).

Computational methods

The UCSF Chimera-X package was used to visualise cryo-EM density maps, AF2 structure predictions, previously deposited structures retrieved from the protein data bank, and crosslinking mass-spectrometry data superimposed onto the structural models (Goddard et al., 2018; Pettersen et al., 2021).

Data Deposition

Protein coordinates and cryo-EM maps were deposited at RCSB and EMDB, respectively (Supplementary Table S1). The mass spectrometry proteomics data have been deposited to the ProteomeXchange Consortium via the PRIDE (Perez-Riverol et al., 2025) partner repository with the dataset identifier PXD072662.

Acknowledgments.

We are grateful to the LMB EM Facility for help with the EM data collection; J. Grimmett, T. Darling and I. Clayson for scientific computing; J. Shi and K. Turton for help with insect cell expression; and to T. Dendooven, D. Kimanius and S. Yatskevich for discussions. For the purpose of open access, the authors have applied a CC BY public copyright license to any Author Accepted Manuscript version arising.

Funding.

UKRI/Medical Research Council MC_UP_1201/6 (D.B.)

Cancer Research UK C576/A25675 (D.B.)

Cancer Research UK C576/A14109 (D.B.): CR-UK PhD studentship (N.N.T).

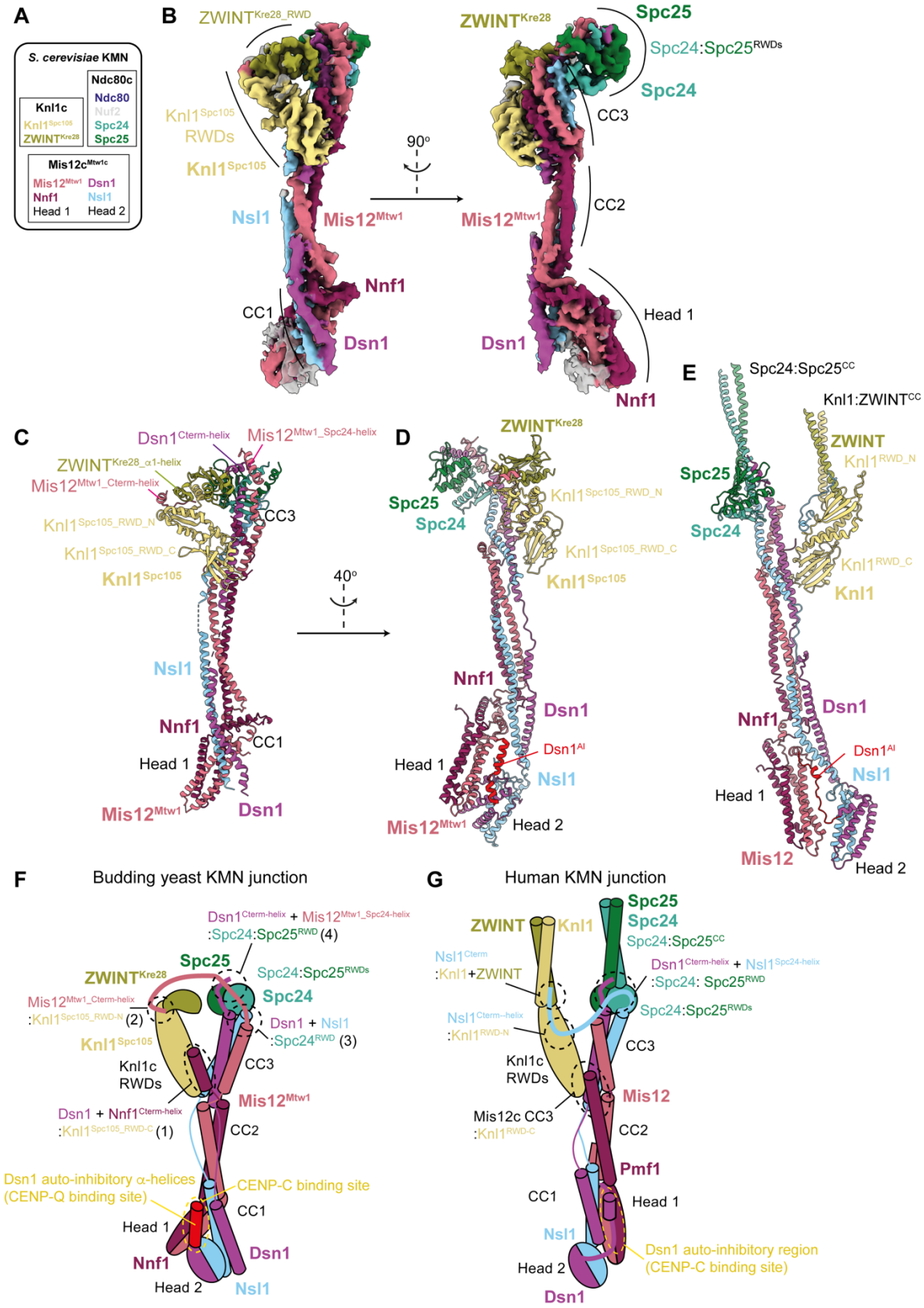

Figure 1: Overall organisation of the *S. cerevisiae* KMN junction complex

A) Subcomplex and subunit composition of the *S. cerevisiae* KMN complex. **B)** Composite cryo-EM density map of the *S. cerevisiae* KMN junction complex derived from docking the apex and base bodies (Figure S2Diii) into the consensus density map. **C)** Model of the KMN junction complex,

highlighting the motifs that mediate the interactions between Mis12c^{Mtw1c} and Knl1c or Ndc80c. **D**) and **E)** Comparison of cryo-EM structures of the inactive *S. cerevisiae* KMN junction complex with head 2 and Dsn1^{AI} defined (this study) (D) with the inactive human KMN junction complex (PDB: 8PPR) from (Yatskevich et al., 2024) (E). Structures shown in D and E were superimposed on the stalk segment (CC2, CC3) of the Mis12/Mis12^{Mtw1} chain. **F)** Cartoon schematic of the *S. cerevisiae* KMN junction complex, based on the structures determined in this study. The interactions between Mis12$^{Mtw1_Cterm\text{-}helix}$ and Knl1$^{Spc105_RWD\text{-}N}$; Nnf1^{Cterm_helix} and Knl1$^{Spc105_RWD\text{-}C}$; Dsn1$^{Cterm\text{-}helix}$ and Mtw1$^{Spc24\text{-}helix}$ and the Spc24 and 25 RWD domains, and Mis12c^{Mtw1c} and the two auto-inhibitory α-helices in Dsn^{AI}, and CENP-C^{Mif2} and CENP-Q^{Ame1} binding sites are highlighted. The four interfaces discussed in the text are numbered in parenthesis. **G)** Cartoon schematic of the human KMN junction complex, based on the structures determined in Yatskevich *et al*., 2024 (PDB: 8PPR). Interactions between Nsl1^{Cterm} and Knl1c; Mis12c stalk CC3 region and Knl1$^{RWD\text{-}C}$; Dsn1$^{Cterm\text{-}helix}$ and Nsl1$^{Spc24\text{-}helix}$ and the Spc24 and 25 RWD domains, and Mis12c head 1 and Dsn1^{AI}, CENP-C binding site are highlighted.

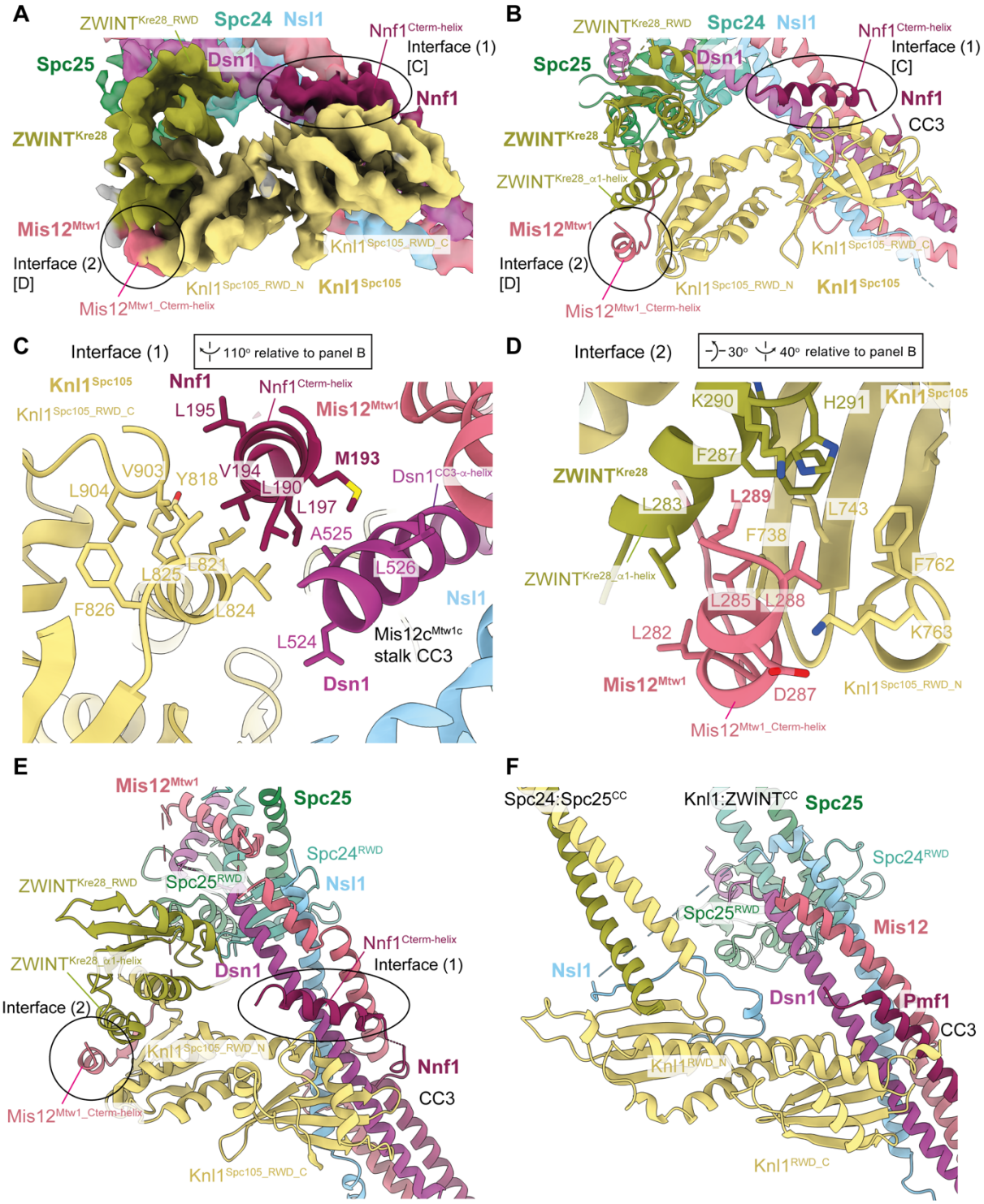

Figure 2: Structural details of the interactions between Mis12c^{Mtw1c} and Knl1c

Cryo-EM density map (Figure S2Diii) highlighting the interactions between Mis12c^{Mtw1c} and Knl1c. [C] and [D] highlight regions of the map that are shown close up in panels **C** and **D**, for interface 1 and interface 2, respectively. **B)** Model of Knl1c engaging in interactions with motifs from Mis12c^{Mtw1c}, highlighting the Mis12$^{Mtw1_Cterm\text{-}helix}$ and Nnf1$^{Cterm\text{-}helix}$ motifs from Mis12c^{Mtw1c} that interact with the Knl1$^{Spc105_RWD\text{-}N}$ and Knl1$^{Spc105_RWD\text{-}C}$ domains, respectively. The molecule is rotated 90° anti-clockwise related to Fig. 1C. **C)** Structural details of the interaction between the Nnf1$^{Cterm\text{-}helix}$

helix, the hydrophobic patch on the Knl1$^{Spc105_RWD\text{-}C}$ domain, and the Dsn1$^{CC3_\alpha\text{-}helix}$ at interface (1). **D)** Structural details of the interaction between the Mis12$^{Mtw1_Cterm\text{-}helix}$ and the interface formed by the ZWINT^{Kre28_RWD} and Knl1$^{Spc105_RWD\text{-}N}$ domains at interface (2). **E)** and **F)** Comparison of *S. cerevisiae* (E) and human (F) KMN junction complexes at the Mis12c interface with Knl1:Zwint. Human structure PDB: 8PPR from (Yatskevich et al., 2024). Structures were superimposed on the Knl1^{RWD} domains. The comparison highlights the interchangeable roles played by the C-termini of Mis12^{Mtw1} in *S. cerevisia*e and Nsl1 in human in contacting the Knl1$^{RWD\text{-}C}$ domain. Views in (E) and (F) similar to (B).

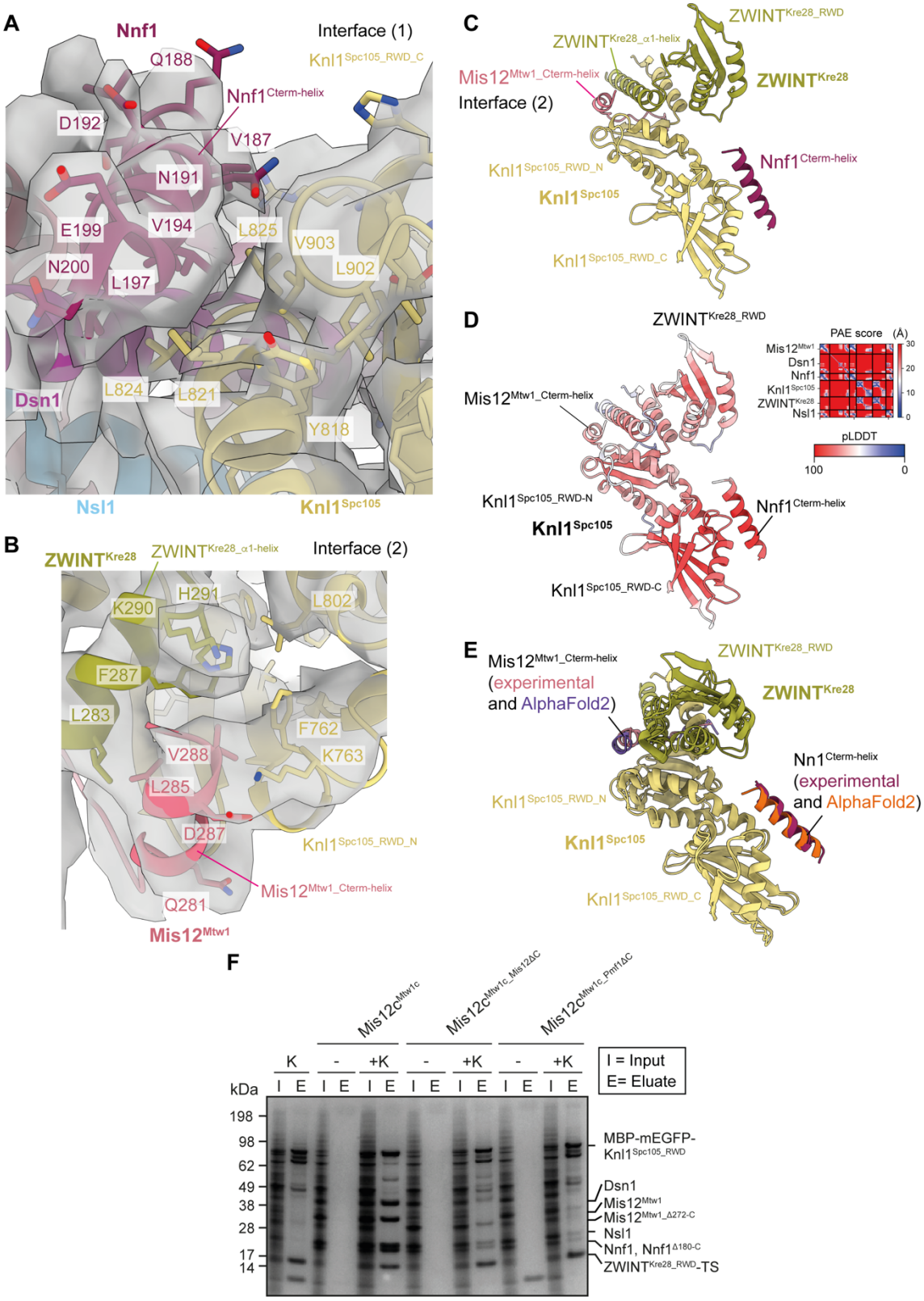

Figure 3: Modelling of interactions between Mis12c^{Mtw1c} and Knl1c

A) Molecular model of the interaction between Nnf1$^{Cterm\text{-}helix}$ and Knl1c docked into the cryo-EM density map, showing density for amino acid side chains relevant to the interaction. View similar to Fig. 3C. **B)** Molecular model of the interaction between Mis12$^{Mtw1_Cterm\text{-}helix}$ at interface (2) and Knl1c docked into the cryo-EM density map, showing density for amino acid side chains relevant to the

interaction. View similar to Fig. 3D. **C)** AF2 structure prediction of the Knl1c:Mis12c^{Mtw1c} interaction. The prediction was performed using full-length protein sequences apart from Knl1^{Spc105}, for which residues 1-444 were excluded. The structure prediction is coloured by chain. **D)** AF2 structure prediction presented in panel **C** with the model coloured by residue pLDDT score and with the predicted alignment error (PAE) score shown as an inset in the top right corner of the panel. **E)** Structural alignment of the Knl1c:Mis12c^{Mtw1c} AF2 model with the Mis12c^{Mtw1c} and Knl1c experimental molecular model generated in this study. The predicted and experimentally modelled Knl1^{Spc105} and ZWINT^{Kre28} subunits are coloured identically, whereas the Nnf1$^{Cterm\text{-}helix}$ and Mis12$^{Mtw1_Cterm\text{-}helix}$ are coloured distinctly according to whether they derive from the AF2 model or the experimental molecular model. **F)** Pulldown experiment to investigate the role of the Mis12$^{Mtw1_Cterm\text{-}helix}$ and Nnf1$^{Cterm\text{-}helix}$ helical motifs in mediating the interaction between Knl1c and Mis12c^{Mtw1c}. Knl1c composed of Knl1^{Spc105_RWD} and ZWINT^{Kre28_RWD} containing a C-terminal twin-strep-tag II (K^{RWD}) was coexpressed with Mis12c^{Mtw1c} in insect cells. I = input, E = eluate, K = K^{RWD} complex present, - = K^{RWD} complex absent, Mis12$^{Mtw1_\Delta C}$ = Mis12$^{Mtw1_\Delta 272\text{-}C}$, Nnf1$^{\Delta C}$ = Nnf1$^{\Delta 180\text{-}C}$. Experimental details are provided in Materials and methods. E, F Structures superimposed on Knl1^{RWD} domains.

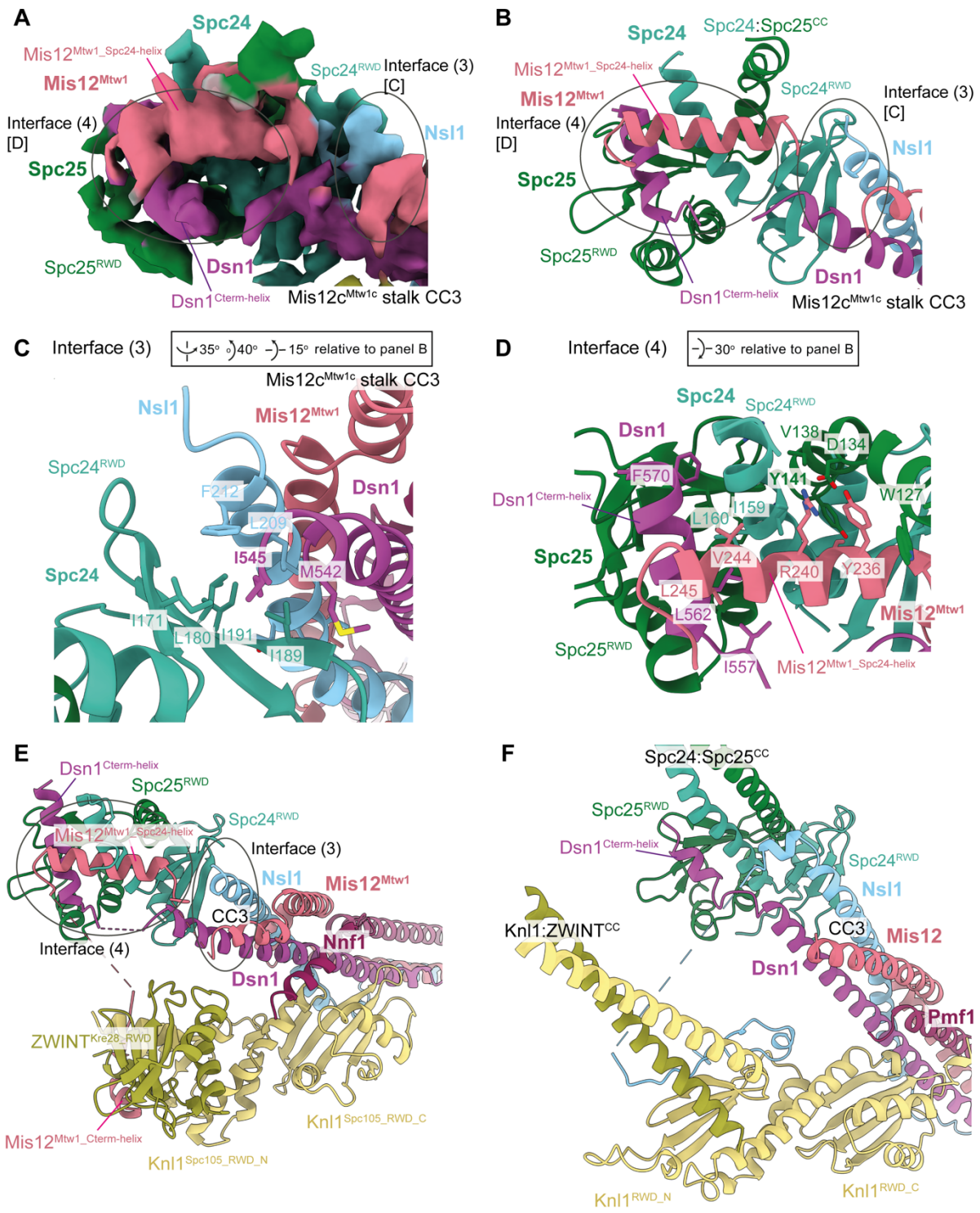

Figure 4: Structural details of interactions between Ndc80c and Mis12c^{Mtw1c}

A) Cryo-EM density map (Figure S2Diii) highlighting the interactions between Mis12c^{Mtw1c} and Spc24 and Spc25 RWD domains. [C] and [D] highlight regions of the map that are shown close-up in panels C and D for interface 3 and interface 4, respectively. **B)** Model of Spc24 and Spc25 RWD domains interacting with motifs from Mis12c^{Mtw1c} , highlighting the Mis12$^{Mtw1_Spc24\text{-}helix}$ and Dsn1$^{Cterm\text{-}helix}$ helical motifs from Mis12c^{Mtw1c} that interact with Spc24 and Spc25 RWD domains at interface (3). The interaction between the CC3 region of the Mis12c^{Mtw1c} stalk domain and the Spc24 RWD domain is also featured. **C)** Structural details of the interactions between the CC3 region of the Mis12c^{Mtw1c} stalk domain and the solvent exposed hydrophobic patch on the Spc24 RWD domain at interface (4).

D) Structural details of the interactions between Dsn1$^{\text{Cterm-helix}}$ and Mis12$^{\text{Mtw1_Spc24-helix}}$ motifs and the Spc24 and Spc25 RWD domains. **E)** and **F)** Comparison of *S. cerevisiae* (E) and human (F) KMN junction complexes at the Mis12c interface with Spc24:Spc25^{RWD} domains. In both *S. cerevisiae* and human KMN junction complexes the Dsn1$^{\text{Cterm-helix}}$ contacts Spc24:Spc25^{RWD} interface. The comparison highlights the interchangeable roles played by the C-termini of Mis12$^{\text{Mtw1}}$ in *S. cerevisiae* (Mis12$^{\text{Mtw1_Spc24 helix}}$) and Nsl1 in human in contacting the Spc24^{RWD}. In the *S. cerevisiae* KMN junction complex, the longer Mis12$^{\text{Mtw1_Spc24 helix}}$ contacts Dsn1$^{\text{Cterm-helix}}$. Structures superimposed on Spc24^{RWD} domain. Human KMN junction (PDB: 8PPR) from (Yatskevich et al., 2024). Views in (E) and (F) similar to (B).

1076

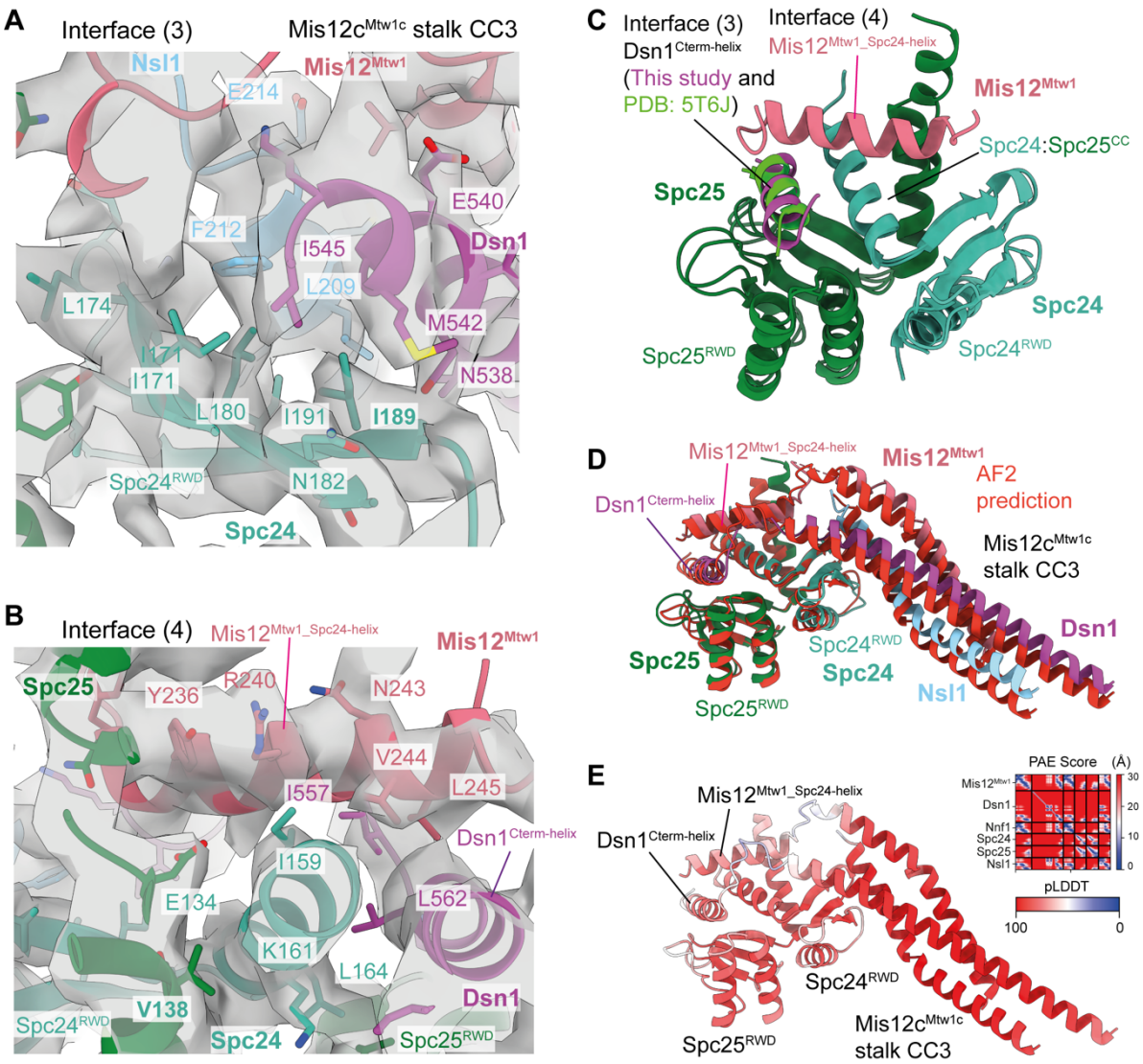

Figure 5: Modelling of interactions between Mis12c^{Mtw1c} and Ndc80c

A) Molecular model of the interactions between the CC3 region of the Mis12c^{Mtw1c} stalk domain and the Spc24 and Spc25 RWD domains at interface (3) docked into the cryo-EM density map, showing density for select amino acid side chains relevant to the interaction. View similar to Fig. 4C. **B)** Molecular model of the interactions between Mis12$^{Mtw1_Spc24\text{-}helix}$ and Dsn1$^{Cterm\text{-}helix}$ motifs with the Spc24 and Spc25 RWD domains at interface (4) docked into the cryo-EM density map, showing density for select amino acid side chains relevant to the interaction. View similar to Fig. 4D. **C)** Structural alignment of the crystal structure of Spc24 and Spc25 RWD domains bound to Dsn1$^{560\text{-}576}$ peptide (PDB: 5T6J) (Dimitrova et al., 2016) onto the Mis12c^{Mtw1c} and Spc24 and Spc25 experimental molecular models (this study). The Spc24 and Spc25 chains derived from 5T6J and this study are coloured identically, whilst Dsn1$^{Cterm\text{-}helix}$ is coloured distinctly according to whether it derives from 5T6J or this study. **D)** AF2 model of the interaction between Spc24, Spc25, and Mis12c^{Mtw1c} (coloured in red), structurally aligned against the Spc24, Spc25, and Mis12c^{Mtw1c} molecular models produced in this study (coloured by chain). The prediction was performed using full-length and wild-type protein sequences for Spc24, Spc25, and Mis12c^{Mtw1c} subunits. **E)** AF2 structure prediction presented in panel **D** coloured by residue pLDDT score, with the predicted alignment error (PAE) score plot shown in inset in the top right corner.

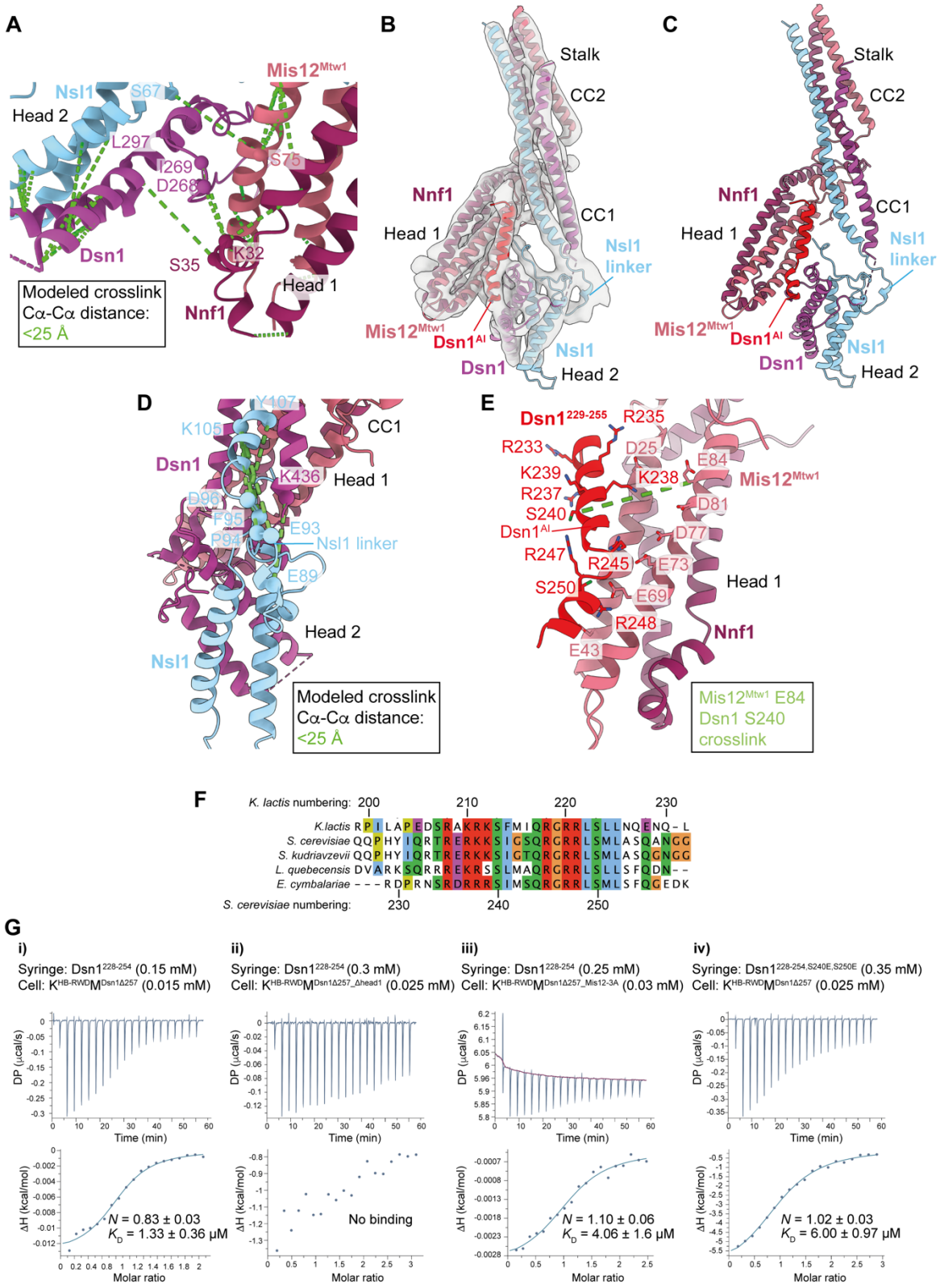

Figure 6: Interactions between the Mis12c^{Mtw1c} head 1 and head 2 domains

A) Observed CL-MS crosslinks on the K^{HB-RWD}M complex, visualised using the molecular model from Figure S5B**.** Inter-subunit crosslinks between residues in the Mis12c^{Mtw1c} head 1 and head 2 domains are highlighted, and relevant Cα atoms of crosslinked residues are shown as spheres. Crosslinks shown are between residues that satisfy the physical distance constraint of the chemical

crosslinker. Crosslinks between two residues are only displayed if both residues are visible in the panel. **B)** Cryo-EM density map with improved occupancy for the Mis12c^{Mtw1c} head 2 domain (Figure S4), interpreted and colour-coded according to experimental model of *Sc*Mis12c^{Mtw1c}. **C)** Experimental cryo-EM model of *Sc*Mis12c^{Mtw1c} head 1 and head 2 domains with Dsn1 auto-inhibitory region (Dsn1^{AI}) at the base of the *Sc*Mis12c^{Mtw1c} stalk domain. **D)** CL-MS cross-links from the *Sc*Mis12c^{Mtw1} dataset that satisfy the physical distance constraint of the chemical crosslinker, indicated in green, mapped onto *Sc*Mis12c^{Mtw1c} head 1, head 2 and stalk domains and Dsn1^{AI}. **E)** Molecular model showing the interaction between the *Sc*Mis12c^{Mtw1c} head 1 domain and Dsn1^{AI} (residues 229-255). *Sc*Mis12c^{Mtw1c} head 2 domain is hidden. **F)** Multiple sequence alignment of Dsn1 protein from distantly related budding yeast demonstrates that the *Kl*Dsn1$^{201-230}$ segment of the Dsn1 N-terminal intrinsically disordered region is conserved. **G)** Isothermal titration calorimetry experiments to determine the identity of the unassigned α-helical-like density. K_D and n values are an average from **i)** three experiments, or **ii)** from two experiments. **i)** Titration of Dsn1$^{228-254}$ peptide to Knl1c:Mis12c^{Mtw1c} complex (K^{HB-RWD}M$^{Dsn1\Delta257}$) with Knl1^{Spc105} residues 1-444 and Dsn1 residues 1-257 deleted. **ii)** Titration of Dsn1$^{228-254}$ peptide to a head 1 deleted Knl1c:Mis12c^{Mtw1c} complex (K^{HB-RWD}M$^{Dsn1\Delta257_\Delta head1}$): Knl1^{Spc105} residues 1-444, Dsn1 residues 1-257, Mis12^{Mtw1} residues 1-106, and Nnf1 residues 1-104 deleted. **iii)** Titration of Dsn1$^{228-254}$ peptide to K^{HB-RWD}M$^{Dsn1\Delta257}$ complex (K^{HB-RWD}M$^{Dsn1\Delta257_Mis12-3A}$) containing mutant Mis12^{Mtw1_E69A,E73A,E77A}. **iv)** Isothermal titration calorimetry data for phosphomimetic mutations at Aurora B sites in Dsn1$^{228-254}$. K_D and n values are an average from two experiments. Titration of Dsn1$^{228-254}$ peptide with S240E and S250E phosphomimetic mutations (Dsn1$^{228-254,S240E,S250E}$) to Knl1c:Mis12c^{Mtw1c} complex (K^{HB-RWD}M$^{Dsn1\Delta257}$) with Knl1^{Spc105} residues 1-444 and Dsn1 residues 1-257 deleted.

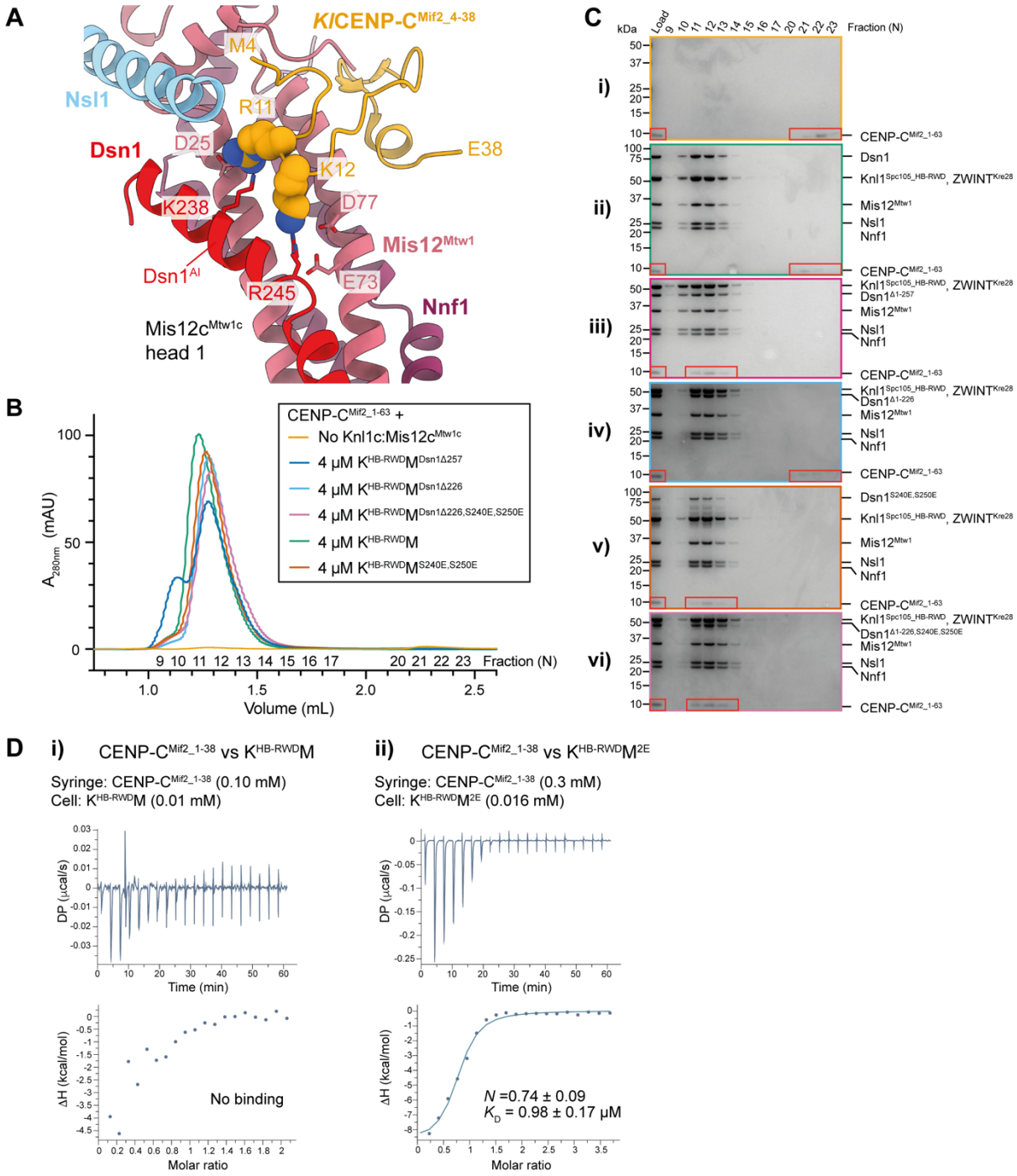

Figure 7: Regulation of Mis12c^{Mtw1c} auto-inhibition by Aurora B kinase and its effect on the interaction with CENP-C^{Mif2}

A) Structural alignment of the crystal structure of *Kluyveromyces lactis* CENP-C^{Mif2} residues 4-36 (*Kl*CENP-C$^{Mif2_4\text{-}36}$) as bound to the *Kl*Mis12c^{Mtw1c} head 1 domain (PDB 5T59) (Dimitrova et al., 2016) to the experimental model of *Sc*Mis12c^{Mtw1c} (this study). The models are coloured by chain; Mis12^{Mtw1} and Nnf1 are coloured identically in 5T59 and our experimentally determined model. *Kl*CENP-C$^{Mif2_4\text{-}36}$ is shown in space filling representation to highlight lack of steric clash, and overlapping binding site, with Dsn1^{AI}. Only *Kl*CENP-C$^{Mif2_4\text{-}36}$ is shown. **B)** SEC elution chromatograms of attempts to reconstitute the interaction between Knl1c:Mis12c^{Mtw1c} complexes containing different Dsn1 N-terminal truncation and/or phosphomimetic mutants and CENP-C^{Mif2} residues 1-63 (CENP-C$^{Mif2_1\text{-}63}$) indicated within red boxes **C)** Coomassie brilliant blue stained SDS-

PAGE gels of the chromatograms shown in panel **B**. **B-C)** $K^{HB\text{-}RWD}M$ = Full-length Dsn1. $K^{HB\text{-}RWD}M^{2E}$ = Full-length Dsn1 containing $Dsn1^{S240E}$ and $Dsn1^{S250E}$ phosphomimetic mutations. $K^{HB\text{-}RWD}M^{Dsn1\Delta257}$ = Dsn1 residues 1-257 are deleted ($Dsn1^{\Delta1\text{-}257}$). $K^{HB\text{-}RWD}M^{Dsn1\Delta226}$ = Dsn1 residues 1-226 are deleted ($Dsn1^{\Delta1\text{-}226}$). $K^{HB\text{-}RWD}M^{Dsn1\Delta226\text{-}2E}$ = Dsn1 residues 1-226 are deleted and $Dsn1^{S240E}$ and $Dsn1^{S250E}$ phosphomimetic mutations ($Dsn1^{\Delta1\text{-}226,S240E,S250E}$). CENP-$C^{Mif2_1\text{-}63}$ is indicated within a red box. **D)** Isothermal titration calorimetry (ITC) data for (**i**) CENP-$C^{Mif2_1\text{-}38}$ interactions with KM, and (**ii**) CENP-$C^{Mif2_1\text{-}38}$ interactions with KM^{2E}.

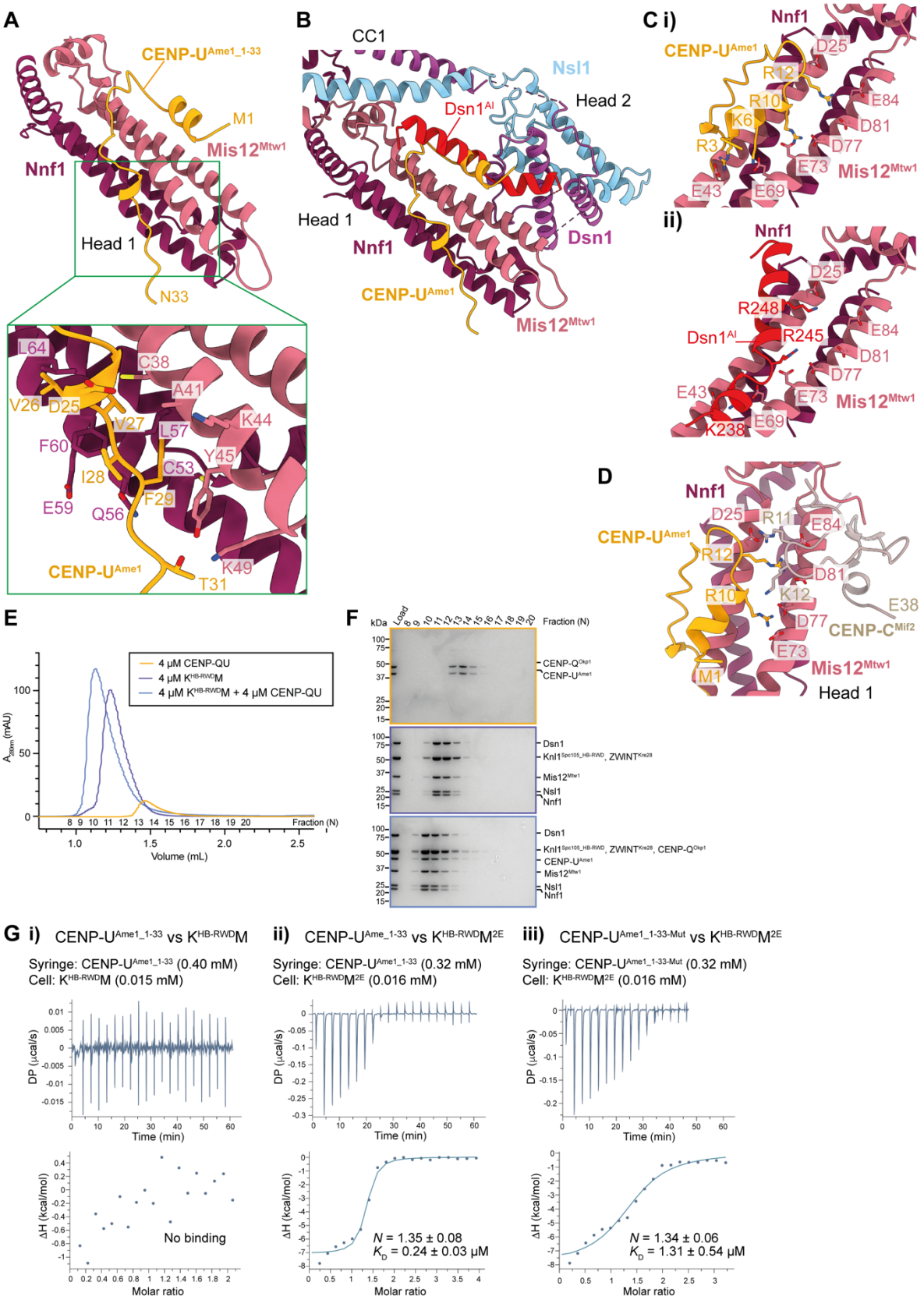

Figure 8: Effect of Mis12c^{Mtw1c} auto-inhibition on the interaction with CENP-U^{Ame1}

A) AF2 structure prediction of the interaction between *S. cerevisiae* Mis12c^{Mtw1c} and CENP-U^{Ame1} coloured by chain, showing only the Mis12c^{Mtw1c} head 1 domain and residues 1-33 of CENP-U^{Ame1} predicted to interact with Mis12c^{Mtw1c}. The structure prediction was performed using full-length and

wildtype proteins apart from Dsn1, from which Dsn1 residues 1-257 were excluded to avoid Mis12c^{Mtw1c} auto-inhibition. Top panel: Overview of complex. Lower panel: details of CENP-U^{Ame1} residues Asp25 to Thr31 interactions with head 1. Val26, Val27, Ile28 and Phe29 of CENP-U^{Ame1} engage a hydrophobic pocket on head 1, augmented by hydrogen bonds from Asp25 and Thr31. **B)** Superimposition of the AF2 model presented in Figure 8A onto the experimental model of *Sc*Mis12c^{Mtw1c} (this study). The subunits are coloured by chain; Mis12^{Mtw1} and Nnf1 are coloured identically in both the AF2 model and in the experimentally determined model. The apparent steric clash between CENP-U^{Ame1} residues 1-24 and Dsn1^{AI} is highlighted. **C)** Comparison of the AF2 model of CENP-U^{Ame1} bound to *Sc*Mis12c^{Mtw1c} (top panel) and Dsn1^{AI} of *Sc*Mis12c^{Mtw1c} (bottom panel). Both CENP-U^{Ame1} and Dsn1^{AI} form basic α-helices that engage the acid patch of head 1. **D)** CENP-C^{MIF2} and CENP-U^{Ame1}-binding sites overlap. **E)** SEC elution chromatograms of CENP-QU alone, Knl1c:Mis12c^{Mtw1c} complexes that lack residues 1-444 of Knl1^{Spc105} alone (K^{HB-RWD}M), or after reconstitution of the interaction between CENP-QU and K^{HB-RWD}M. **F)** Coomassie brilliant blue stained SDS-PAGE gels of the experiments of the experiments in panel **E**. **G)** Isothermal titration calorimetry (ITC) data for (**i**) CENP-U$^{Ame1_1-33}$ interactions with KM, (**ii**) CENP-U$^{Ame1_1-33}$ interactions with KM^{2E} and (**iii**) the CENP-U$^{Ame1_1-33}$ mutant with Ala substitutions of D25, V27, I28, F29, T31 predicted to interact with Mis12c^{Mtw1c} (Figure 8C, D) to KM^{2E}.

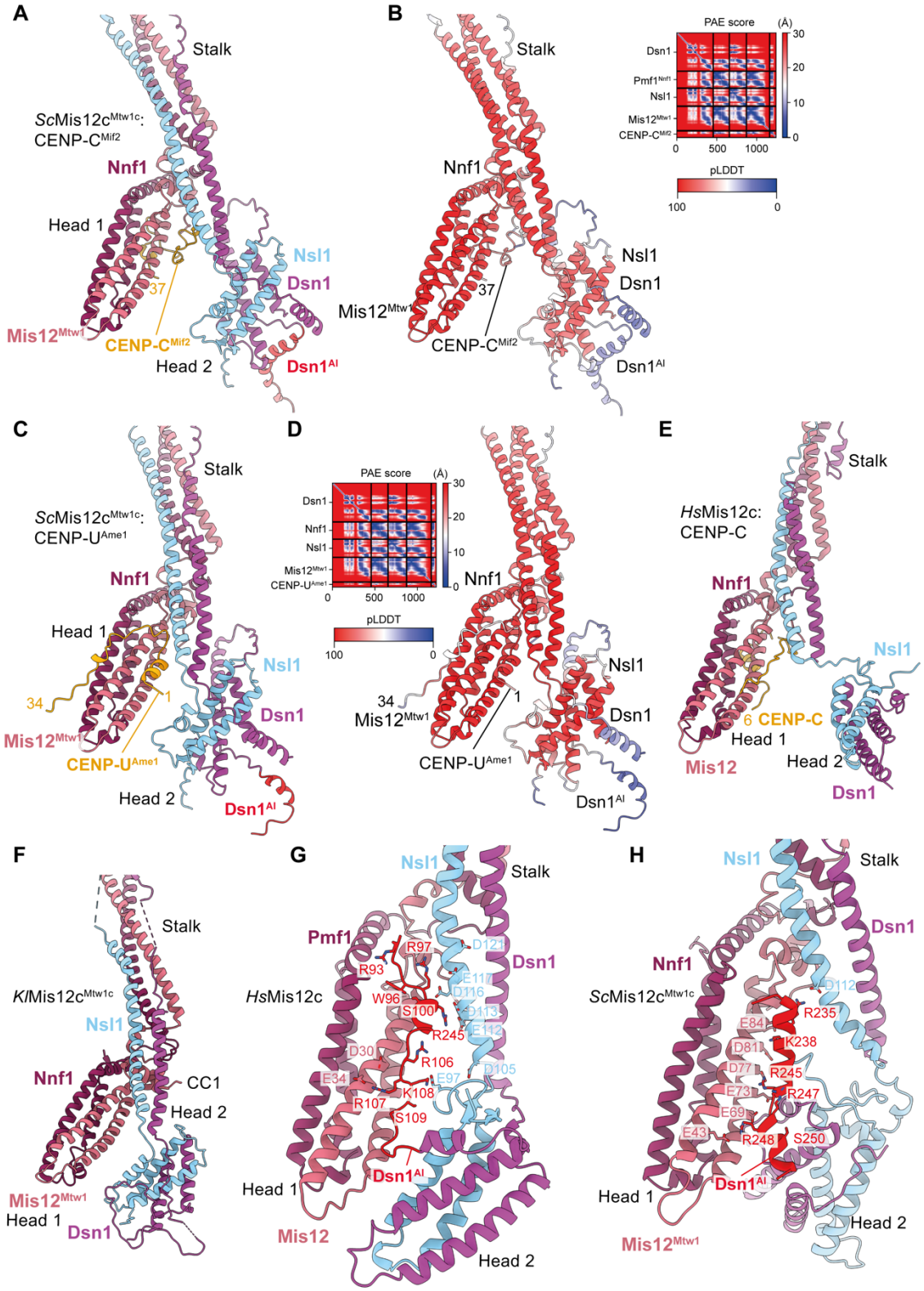

Figure 9: Comparison of cryo-EM structure of *Sc*Mis12c^{Mtw1c} with AF2 models of *Sc*Mis12c^{Mtw1c} in complex with CENP-C^{Mif2} and CENP-U^{Ame1} and *Kl*Mis12c and human Mis12c.

A) AF2 model of *Sc*Mis12c^{Mtw1c} in complex with CENP-C^{Mif2} (residues of 1-55). **B)** Model coloured by residue pLDDT score. The predicted alignment error (PAE) score plot is shown to the right. **C)** AF2 model of *Sc*Mis12c^{Mtw1c} in complex with CENP-U^{Ame1} (residues 1-34 of CENP-U^{Ame1} shown). **D)** Model coloured by residue pLDDT score. The predicted alignment error (PAE) score plot is shown to the right. In both AF2 models, head 2 is predicted to rotate by 180° about two orthogonal axes relative

to head 2 of the inactive *Sc*Mis12c^{Mtw1c} structure in Figure 6C. **E)** Crystal structure of the heads and stalk region of activated human Mis12c in complex with CENP-C (residues 1-48) (PDB: 5LSK) (Petrovic et al., 2016). **F)** Crystal structure of the heads and stalk region of *K. lactis* Mis12c^{Mtw1c} (PDB: 5T58) (Dimitrova et al., 2016). Head 2 adopts a similar conformation to head 2 of the AF2 model of *Sc*Mis12c^{Mtw1c} (Figure S5E). **G)** and **H)** Comparison of the cryo-EM structures of the heads and stalk region of human Mis12c in the inactive unphosphorylated conformation (PDB: 8PPR) (Yatskevich et al., 2024) (G) with the equivalent regions of *S. cerevisiae* Mis12c^{Mtw1c} (this study) (H). The structures shown in G and H were superimposed on the Mis12 chain of head 1.

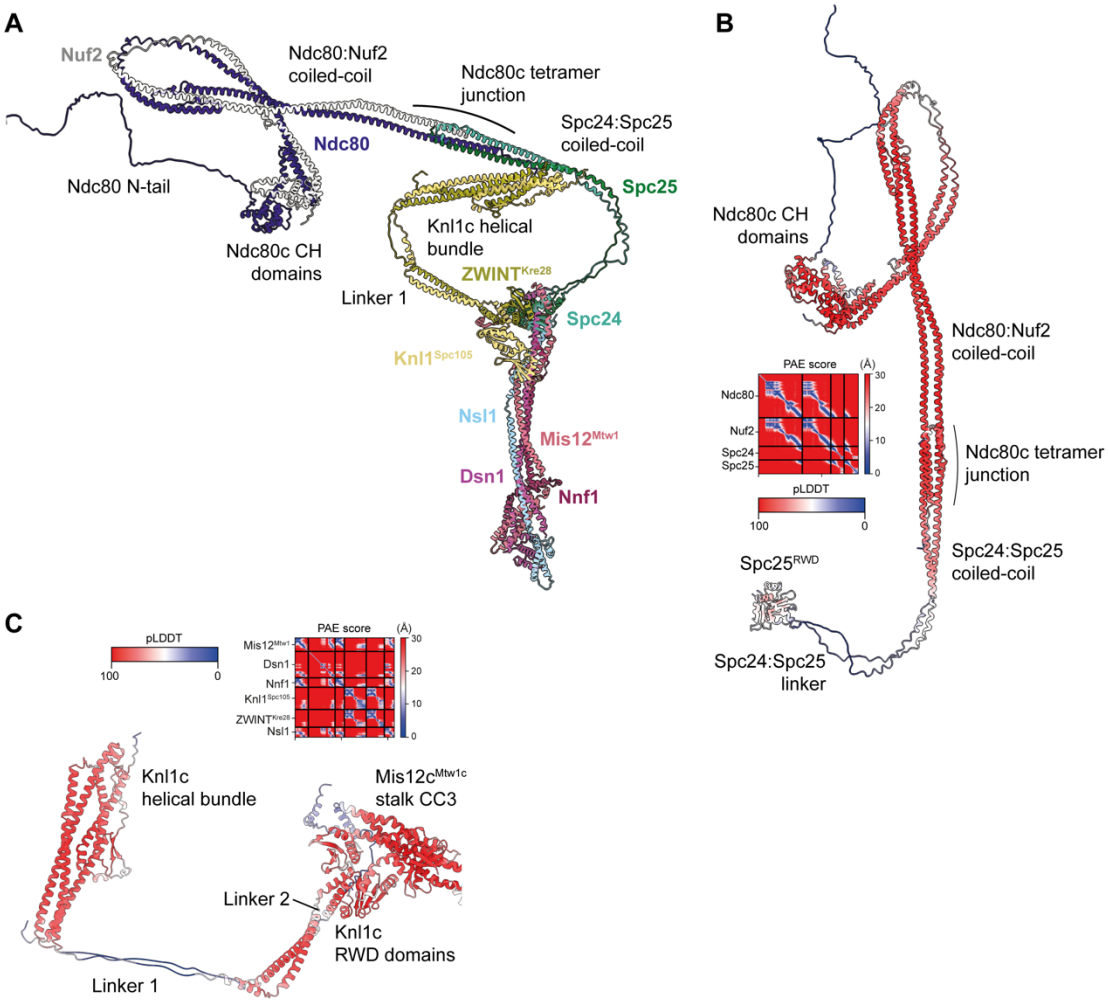

Figure 10: Hypothetical model of the entire *S. cerevisiae* KMN complex and comparison to humans

A) Model of the entire *S. cerevisiae* KMN complex based on the structures determined experimentally in this study and AF2 models of Knl1c and Ndc80c. Flexibility of Ndc80c has been previously demonstrated (Scarborough et al., 2019; Wang et al., 2008), and flexibility of the Knl1c helical bundle is inferred from AF2 models. CH: calponin homology. N-tail: N-terminal tail. **B)** AF2 structure prediction of Ndc80c, coloured by residue pLDDT score. The structure was predicted using full-length, wildtype protein sequences. The predicted alignment error (PAE) score plot of the AF2 Ndc80c model is shown on the left of the panel. **C)** AF2 structure prediction of Knl1c:Mis12c^{Mtw1c} showing the Knl1c helical bundle domain, Knl1c RWD domains, and Mis12c^{Mtw1c} stalk CC3 region. The structure was predicted using full-length, wildtype protein sequences coloured by residue pLDDT score with the predicted alignment error (PAE) score plot shown above.

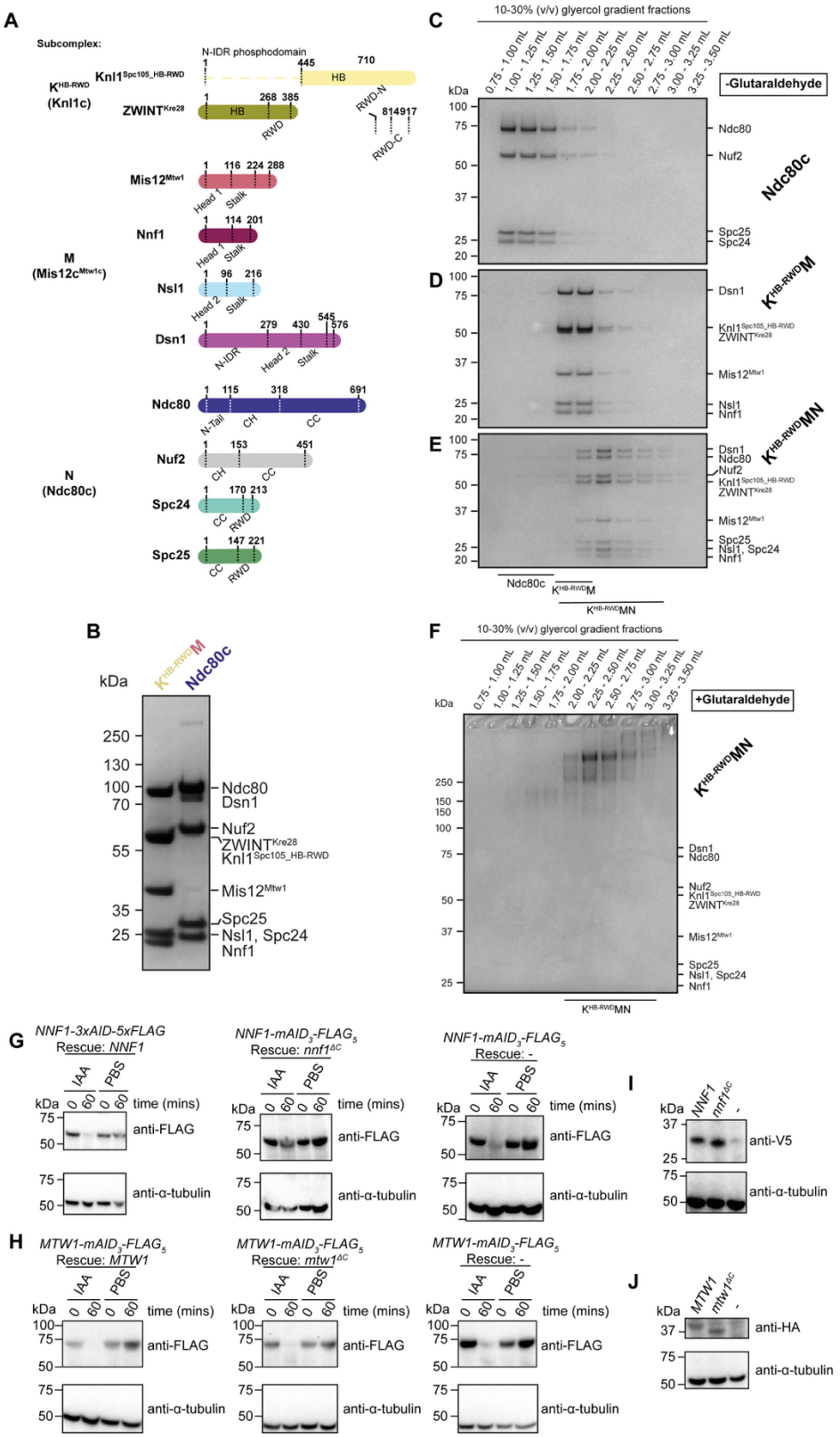

Figure S1: Preparation of *S. cerevisiae* KMN complex sample for Cryo-EM and Validation of *in vivo* protein depletion and *in vivo* rescue allele expression

A) Subcomplex and subunit domain organisation of the *S. cerevisiae* KMN complex proteins. Coiled-coil (CC), calponin homology (CH), helical bundle (HB), N-terminal intrinsically disordered region (N-IDR) and RING-WD40-DEAD box helicase (RWD) domains are highlighted. **B)** Coomassie brilliant blue stained SDS-PAGE gels of the purified KMN subcomplexes. **C-E)** Coomassie brilliant

blue stained SDS-PAGE gels of isolated **C)** N and **D)** $K^{HB\text{-}RWD}M$ subcomplexes, or **E)** reconstituted $K^{HB\text{-}RWD}MN$ complexes after separation using 10-30% glycerol gradients. **F)** Coomassie brilliant blue stained SDS-PAGE gels of the reconstituted $K^{HB\text{-}RWD}MN$ complex crosslinked with a 0.0–0.2% glutaraldehyde gradient over the course of a 10–30% glycerol gradient using the GraFix methodology (Stark, 2010). Crosslinking was repeated twice with identical results. Fractions corresponding to the glycerol gradient volume 2.00 – 2.75 mL were pooled for cryo-EM sample preparation. Fractions corresponding to the glycerol gradient volume 2.00 – 2.75 mL were pooled for cryo-EM sample preparation. **G)** Immunoblots of whole cell extracts (WCEs) of the indicated yeast strains treated for the indicated duration with PBS or 0.5 mM Indole-3-acetic acid (IAA). Membranes were blotted with anti-FLAG primary antibody to detect *NNF1-mAID$_3$-FLAG$_5$* gene products (top panel) or anti-α-tubulin primary antibody as a loading control (bottom panel). **H)** Immunoblots of WCEs of the indicated yeast strains treated for the indicated duration with PBS or 0.5 mM Indole-3-acetic acid (IAA). Membranes were blotted with anti-FLAG primary antibody to detect *MTW1-mAID$_3$-FLAG$_5$* gene products (top panel) or anti-α-tubulin primary antibody as a loading control (bottom panel). **I)** Immunoblots of WCEs of the indicated yeast strains. Membranes were blotted with anti-V5 primary antibodies to detect the gene products expressed from the *NNF1* or *nnf1$^{\Delta C}$* variant alleles (top panel), or with anti-α-tubulin primary antibody as a loading control (bottom panel). **J)** Immunoblots of WCEs of the indicated yeast strains. Membranes were blotted with anti-HA primary antibodies to detect the gene products expressed from the indicated *MTW1* or *mtw1$^{\Delta C}$* variant alleles (top panel), or with anti-α-tubulin primary antibody as a loading control (bottom panel).

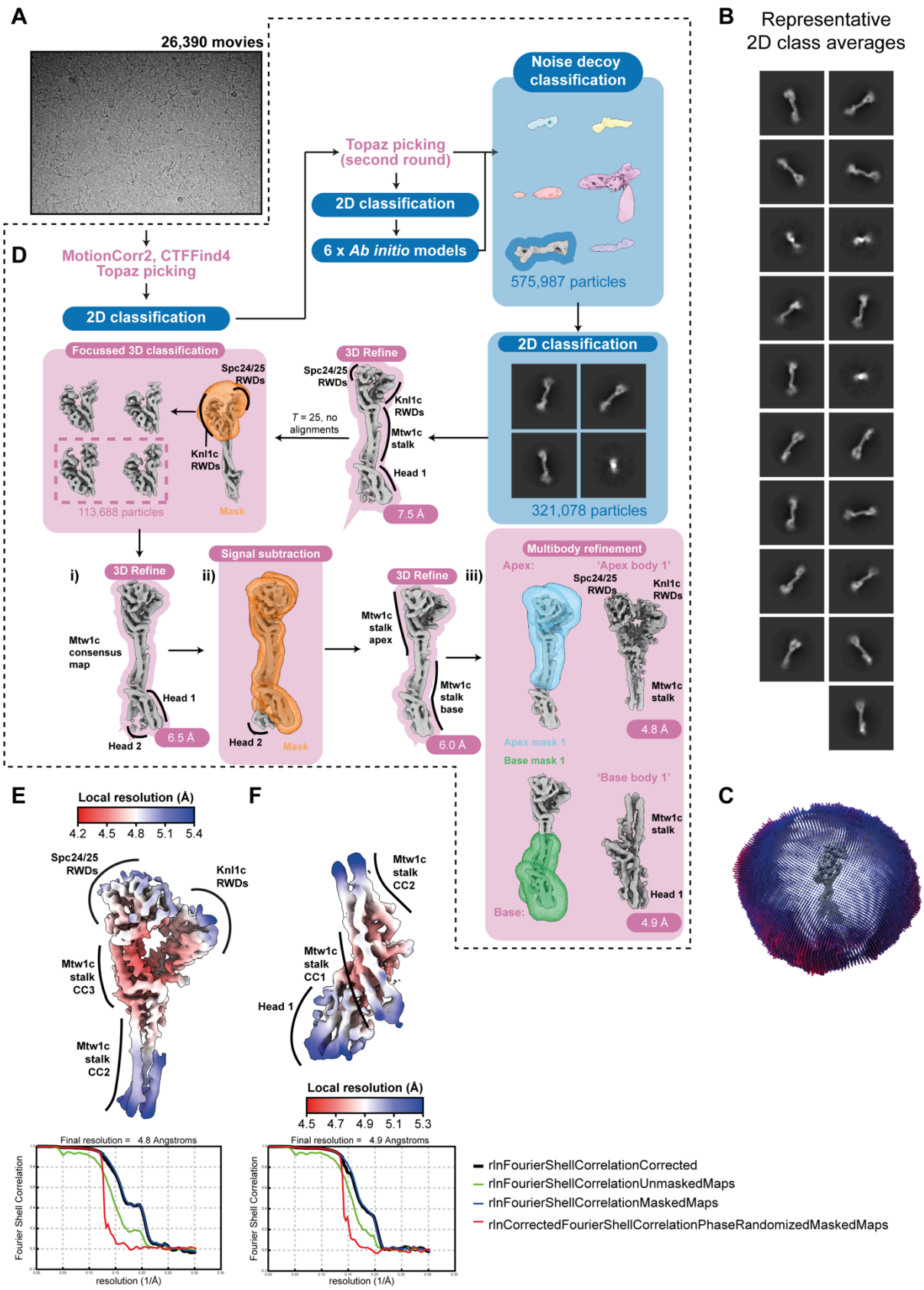

Figure S2: Cryo-EM data processing to reconstruct the KMN junction complex

A) Representative motion corrected cryo-EM movie obtained after data acquisition. A total of 26,390 cryo-EM movies were obtained after data acquisition. **B)** Representative 2D class averages generated using CryoSparc during the 2D classification step following noise decoy classification. **C)** Angular

distribution of views plot of the particles that contributed to the 'apex body 1' and 'base body 1' reconstructions. **D)** Cryo-EM data processing scheme used to reconstruct higher resolution cryo-EM density maps for the KMN junction complex, as described in the Materials and methods section. **E-F)** Cryo-EM density maps coloured according to local resolution of the **E)** 'apex body 1' and **F)** 'base body 1' multibody derived reconstructions that were used to build molecular models (top). Fourier shell correlation (FSC) plot of the **E)** 'apex body 1' and **F)** 'base body 1' multibody derived reconstructions that were used to build the model of the KMN junction complex (bottom).

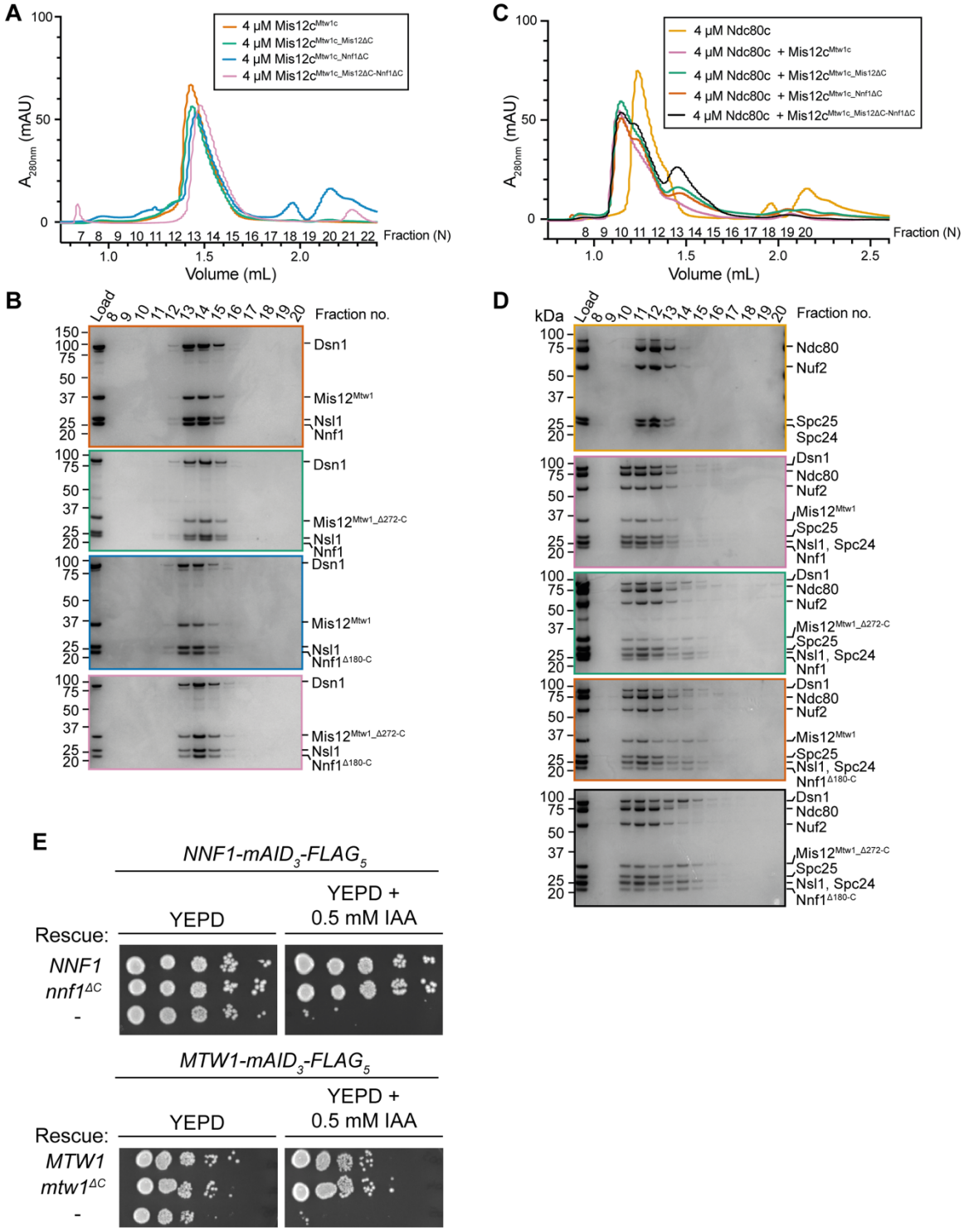

Figure S3: Biochemical analysis of Mis12$^{Mtw1_Cterm\text{-}helix}$ and Nnf1$^{Cterm\text{-}helix}$ function

A) SEC elution chromatograms of Mis12c^{Mtw1c} containing either full-length and wild-type proteins, or with full-length and wild-type proteins apart from deletion of Mis12^{Mtw1} residues 272-289 (Mis12$^{Mis12_\Delta272\text{-}C}$: Mis12c$^{Mtw1c_Mis12\Delta C}$), deletion of Nnf1 residues 180-201 (Nnf1$^{\Delta180\text{-}C}$: Mis12c$^{Mtw1c_Nnf1\Delta C}$), or deletion of both Mis12^{Mtw1} residues 272-289 and Nnf1 residues 180-201 (Mis12c$^{Mtw1c_Mis12\Delta C\text{-}Nnf1\Delta C}$). **B)** Coomassie brilliant blue stained SDS-PAGE gels of all of the experiments presented in panel **A**. **C)** SEC elution chromatograms of the Mtw1c:Ndc80c interaction reconstitutions. Attempts at reconstituting Mis12c^{Mtw1c} , Mis12c$^{Mtw1c_Mis12\Delta C}$, Mis12c$^{Mtw1c_Nnf1\Delta C}$, and Mis12c$^{Mtw1c_Mis12\Delta C\text{-}}$ Nnf1$^{\Delta C}$ with full-length, unmodified Ndc80c are presented alongside the elution

profile of Ndc80c alone. **D)** Coomassie brilliant blue stained SDS-PAGE gels of the experiments in panel **C**. **E)** Analysis of *mtw1*$^{\Delta C}$ and *nnf1*$^{\Delta C}$ mutants in yeast strain backgrounds with endogenous *MTW1* and *NNF1* gene products translationally fused to mAID$_3$-FLAG$_5$ tag. Cell growth was investigated by plating 1:9 serial dilutions onto either YEPD plates or YEPD plates supplemented with 0.5 mM Indole-3-acetic acid (IAA). - = no rescue allele was expressed. mAID = monomeric auxin inducible degron.

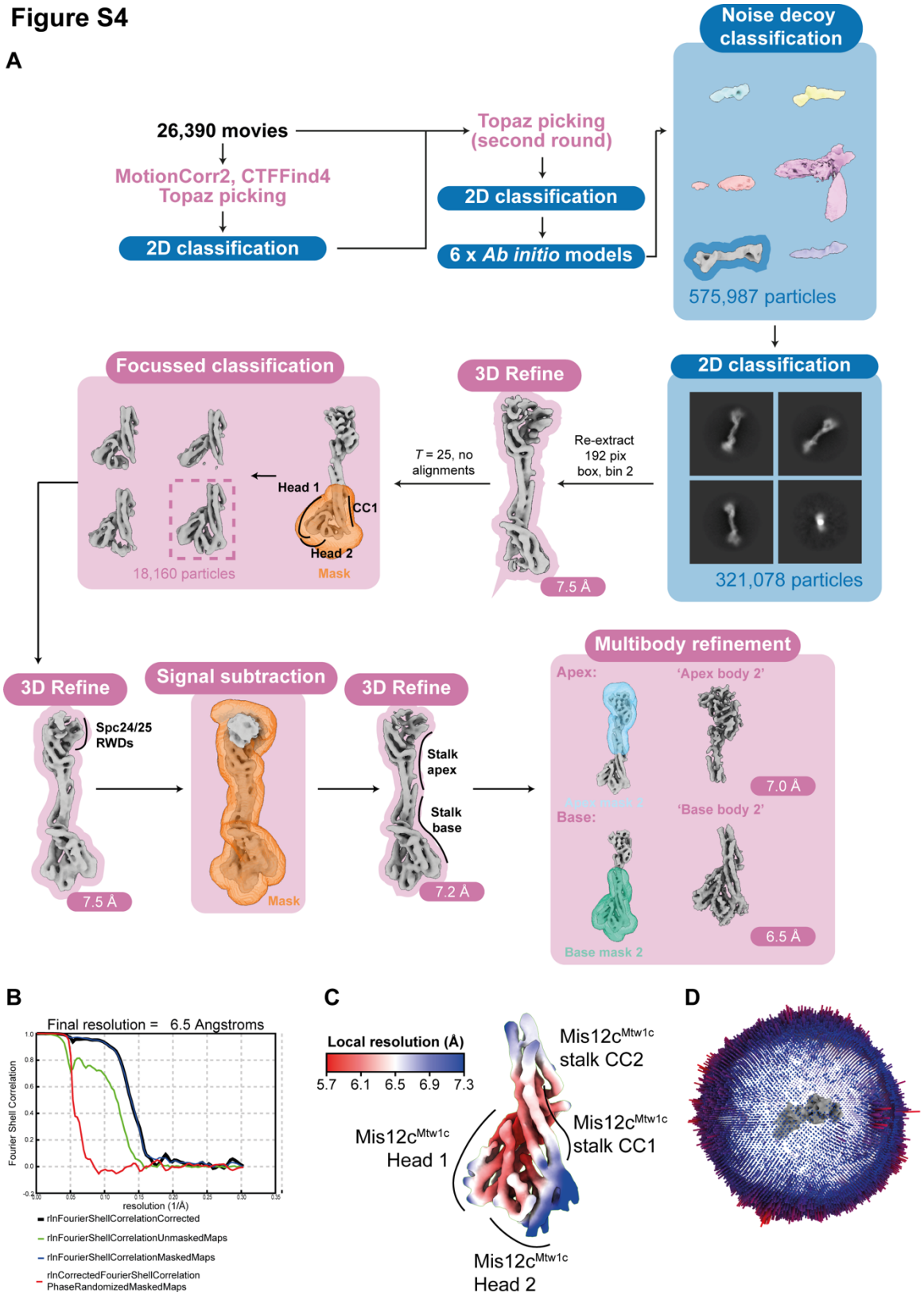

Figure S4: Cryo-EM data processing to reconstruct Mis12c^{Mtw1c} head 2 domain

A) Cryo-EM data processing scheme used to reconstruct cryo-EM density maps containing continuous density for the Mis12c^{Mtw1c} head 2 domain, as described in the Materials and methods section. **B)** Fourier shell correlation (FSC) plot for 'base body 2'. **C)** Cryo-EM density map for 'base

body 2' that was used to model the Mis12c^{Mtw1c} head 2 domain coloured according to local resolution. **D)** Angular distribution of views plot for the particles that contributed to the reconstruction of 'base body 2'.

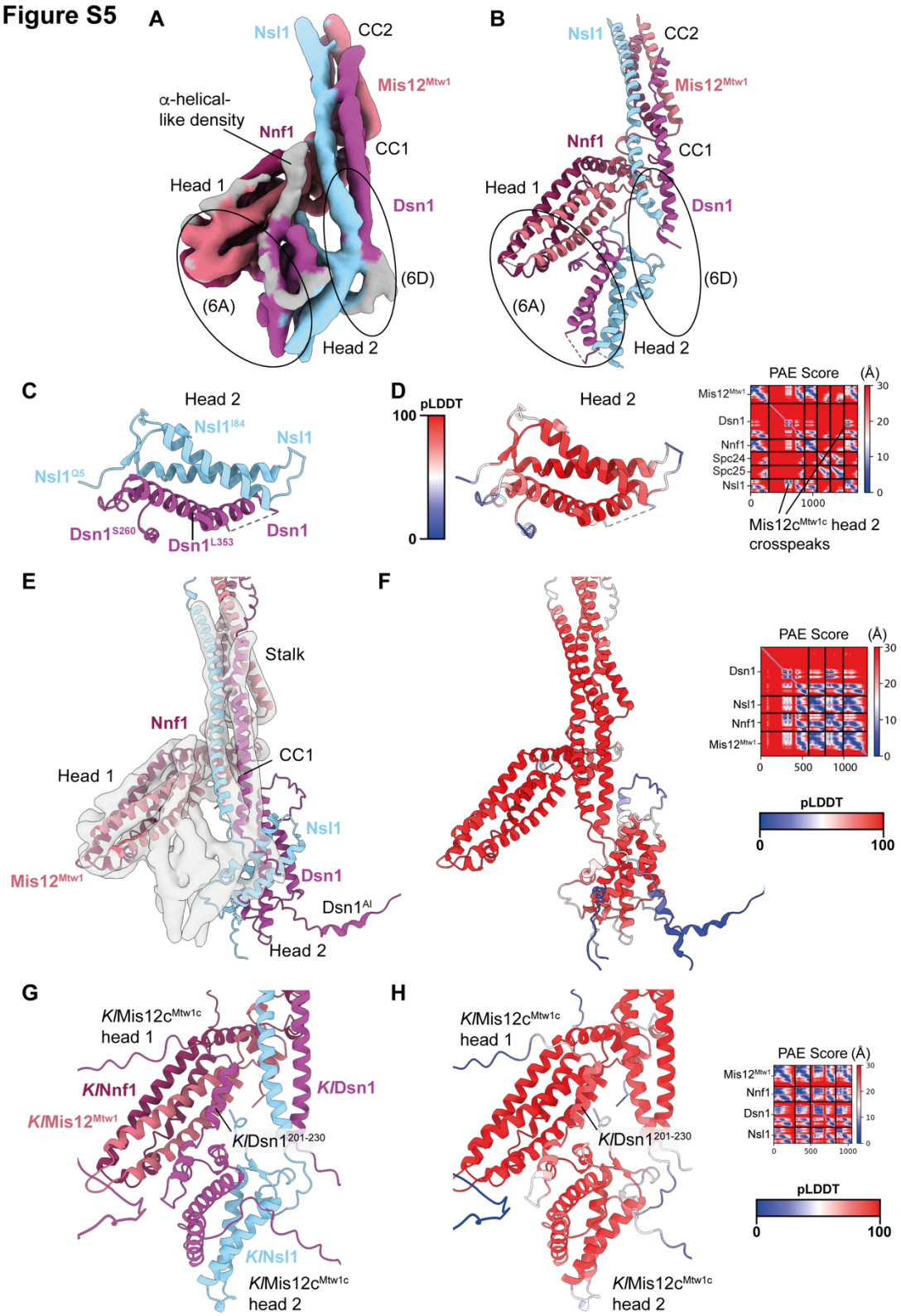

Figure S5: Modelling of contacts between Mis12c^{Mtw1c} head 1, head 2 and Dsn1$^{N\text{-}IDR}$ domains

A) Cryo-EM density map with improved occupancy for the Mis12c^{Mtw1c} head 2 domain (Figure S4) interpreted using the model of Mis12c^{Mtw1c} stalk and head 1 domains built in this study and the AF2 model of *S. cerevisiae* head 2 presented in panels **C** and **D**. (6A) and (6D) highlight regions of the map that are shown in close up in Figures 6A and 6D, respectively. **B)** Experimental model of *S. cerevisiae* Mis12c^{Mtw1c} head 1 and head 2 domains interacting at the base of the *S. cerevisiae*

Mis12c^{Mtw1c} stalk domain. **C)** AF2 structure prediction of the *S. cerevisiae* Mis12c^{Mtw1c} head 2 domain from the Mis12c^{Mtw1c}:Spc24:Spc25 prediction coloured by chain. Mis12c^{Mtw1c} head 1 and stalk domains, and Spc24:Spc25 are not shown. **D)** AF2 model presented in panel **C** coloured by residue pLDDT score. The predicted alignment error (PAE) score plot is shown on the right of the panel. **E)** AF2 structure prediction of *S. cerevisiae* Mis12c^{Mtw1c} (*Sc*Mis12c^{Mtw1c}) coloured by chain docked into the cryo-EM map. The prediction of the head 2 position and orientation does not fit the cryo-EM density. **F)** AF2 model presented in panel **E** coloured by residue pLDDT score. The predicted alignment error (PAE) score plot is shown on the right of the panel. **G)** AF2 structure prediction of the *K. lactis* Mis12c^{Mtw1c} (*Kl*Mis12c^{Mtw1c}) coloured by chain. The prediction was performed using all full-length and wild-type protein sequences apart from *K. lactis* Dsn1 (*Kl*Dsn1), for which residues 1-149 were excluded to obtain predictions for the interaction between *Kl*Dsn1$^{201-230}$ and *Kl*Mis12c^{Mtw1c} head 1 domain. **H)** AF2 model presented in panel **G** coloured by residue pLDDT score. The predicted alignment error (PAE) score plot is shown on the right of the panel.

Data collection and processing						
Microscope	FEI Titan Krios 1					
Voltage (keV)	300					
Magnification	105,000					
Detector	Gatan K3					
Electron dose (e^-/Å^2)	40					
Pixel size (Å/pixel)	0.825					
Exposure rate (e^-/pixel/s)	15.6					
Frames/micrograph (N)	40					
Automation software	EPU					
Micrographs collected (N)	26,390					
Micrographs used (N)	26,390					
Defocus (µm)	-1.4 to -3.0					
Magnification	105,000					
Total extracted particles (N)	2,592,458					
Cryo-EM reconstructions						
	KMN junction consensus map	KMN junction composite map	KMN junction apex body 1	KMN junction base body 1	KMN junction consensus map (head 2)	KMN junction base body 2
Figure	S2Dii	S2Dii	S2E	S2F	S4A	S4C
Accession codes	EMD-54576 PDB N/A	EMD-54579 PDB 9S4Q	EMD-54578 PDB N/A	EMD-54577 PDB N/A	EMD-54602 PDB 9S5N	EMD-54586 PDB 9S53
Final particles (N)	113,688	113,688	113,688	113,688	18,160	18,160
Point group	C1	C1	C1	C1	C1	C1
Resolution global (Å)	6.0	4.8-4.9	4.8	4.9	7.2	6.5
Resolution range local (Å)	ND	ND	4.2-5.4	4.7-5.3	ND	5.7-7.3
FSC threshold	0.143	0.143	0.143	0.143	0.143	0.143
Map sharpening method	RELION					
Refinement						
Software	Phenix					
Resolution limit (Å)	N/A	4.9	N/A	N/A	7.2	6.5
Protein atoms (N)		19,480			21,005	8,388
RMSD bond length (Å)		0.019			0.018	0.027
RMSD bond angle (°)		0.567			0.446	0.596
Model to map fit						
CC mask	N/A	0.6770	N/A	N/A	0.8221	0.8419
CC volume		0.6899			0.8186	0.8423
Validation						
All-atom clash score	N/A	9.81	N/A		15.77	34.52
Ramachandran plot						
Preferred (%)	N/A	95.04	N/A	N/A	96.02	95.66
Allowed (%)		4.88			3.91	4.17
Outliers (%)		0.09			0.07	0.17

Table S1: Cryo-EM data collection, refinement and validation statistics

Strain	Genotype
BY26972 (The Yeast Resource Genetic Resource Center, Japan)	*MAT **a** ade2-1 his3-11,15 trp1-1 leu2-3,112 can1-100 ura3-1::ADH1 OsTIR1(Pmk200, URA3)*
Ynnt001	*MAT **a** ade2-1 his3-11,15 trp1-1 leu2-3,112 can1-100 ura3-1::ADH1 OsTIR1(Pmk200, URA3) MTW1-mAID$_3$-FLAG$_5$::G418*
Ynnt002	*MAT **a** ade2-1 his3-11,15 trp1-1 leu2-3,112 can1-100 ura3-1::ADH1 OsTIR1(Pmk200, URA3) NNF1-mAID$_3$-FLAG$_5$*
MTW1	*MAT **a** ade2-1 his3-11,15 trp1-1 leu2-3,112 can1-100 ura3-1::ADH1 OsTIR1(Pmk200, URA3), MTW1-mAID$_3$-FLAG$_5$, HA$_3$-MTW1::LEU2*
Mtw1$^{\Delta C}$	*MAT **a** ade2-1 his3-11,15 trp1-1 leu2-3,112 can1-100 ura3-1::ADH1 OsTIR1(Pmk200, URA3), MTW1-mAID$_3$-FLAG$_5$, HA$_3$-MTW1(Δ272-C)::LEU2*
Empty vector (LEU2)	*MAT **a** ade2-1 his3-11,15 trp1-1 leu2-3,112 can1-100 ura3-1::ADH1 OsTIR1(Pmk200, URA3) MTW1-mAID$_3$-FLAG$_5$, Pleu2::LEU2*
NNF1	*MAT **a** ade2-1 his3-11,15 trp1-1 leu2-3,112 can1-100 ura3-1::ADH1 OsTIR1(Pmk200, URA3), NNF1-mAID$_3$-FLAG$_5$, V5$_3$-NNF1::TRP1*
Nnf1$^{\Delta C}$	*MAT **a** ade2-1 his3-11,15 trp1-1 leu2-3,112 can1-100 ura3-1::ADH1 OsTIR1(Pmk200, URA3), NNF1-mAID$_3$-FLAG$_5$, V5$_3$-NNF1(Δ180-C)::TRP1*
Empty vector (TRP1)	*MAT **a** ade2-1 his3-11,15 trp1-1 leu2-3,112 can1-100 ura3-1::ADH1 OsTIR1(Pmk200, URA3), NNF1-mAID$_3$-FLAG$_5$, Ptrp1::TRP1*

Table S2: Genotypes of *S. cerevisiae* strains used within this study.

1077 **Supplementary Video Captions**

1078 **Video S1. Overview of the *S. cerevisiae* KMN junction complex.**

1079 Video shows the molecular details of the *S. cerevisiae* KMN junction complex as shown in
1080 Figures 1-3, detailing the overall architecture of the complex (Figure 1); details of the
1081 Mis12c^{Mtw1c} interface with Knl1c^{Spc105c} (Figure 2); and details of the Mis12c^{Mtw1c} interface
1082 with Ndc80c (Figure 3).

1083 **Video S2. Predicted conformational change of Dsn1^{AI} and head 2 accompanying**
1084 ***Sc*Mis12c^{Mtw1c} activation by Dsn1^{AI} phosphorylation.**

1085 Video shows proposed conformational change of Dsn1^{AI} and head 2 caused by Aurora B^{Ipl1}-
1086 phosphorylation of Ser240 and Ser250 (Figure 7). Phospho-Ser240 would cause electrostatic
1087 repulsion with the negatively-charged surface of Mis12c^{Mtw1c} head 1 as well as steric clashes
1088 with Nsl1 of head 2. Displacement of Dsn1^{AI} and head 2 releases the CENP-C^{Mif2}-binding
1089 site on Mis12c^{Mtw1c} mainly mediated through head 1. The Mis12c^{Mtw1c}-CENP-C ^{Mif2} complex
1090 is based on an AF2 model.

References

Akiyoshi, B., C.R. Nelson, and S. Biggins. 2013. The Aurora B Kinase Promotes Inner and Outer Kinetochore Interactions in Budding Yeast. *Genetics*. 194:785-789.

Akiyoshi, B., K.K. Sarangapani, A.F. Powers, C.R. Nelson, S.L. Reichow, H. Arellano-Santoyo, T. Gonen, J.A. Ranish, C.L. Asbury, and S. Biggins. 2010. Tension directly stabilizes reconstituted kinetochore-microtubule attachments. *Nature*. 468:576-579.

Alushin, G.M., V. Musinipally, D. Matson, J. Tooley, P.T. Stukenberg, and E. Nogales. 2012. Multimodal microtubule binding by the Ndc80 kinetochore complex. *Nature Structural & Molecular Biology*. 19:1161-1167.

Alushin, G.M., V.H. Ramey, S. Pasqualato, D.A. Ball, N. Grigorieff, A. Musacchio, and E. Nogales. 2010. The Ndc80 kinetochore complex forms oligomeric arrays along microtubules. *Nature*. 467:805-810.

Aravamudhan, P., I. Felzer-Kim, K. Gurunathan, and A.P. Joglekar. 2014. Assembling the Protein Architecture of the Budding Yeast Kinetochore-Microtubule Attachment using FRET. *Current Biology*. 24:1437-1446.

Ariyoshi, M., and T. Fukagawa. 2023. An updated view of the kinetochore architecture. *Trends in Genetics*. 39:941-953.

Ariyoshi, M., F. Makino, R. Watanabe, R. Nakagawa, T. Kato, K. Namba, Y. Arimura, R. Fujita, H. Kurumizaka, E.I. Okumura, M. Hara, and T. Fukagawa. 2021. Cryo-EM structure of the CENP-A nucleosome in complex with phosphorylated CENP-C. *The EMBO Journal*. 40. 40(5):e105671. doi: 10.15252/embj.2020105671

Batth, T.S., M.X. Tollenaere, P. Rüther, A. Gonzalez-Franquesa, B.S. Prabhakar, S. Bekker-Jensen, A.S. Deshmukh, and J.V. Olsen. 2019. Protein Aggregation Capture on Microparticles Enables Multipurpose Proteomics Sample Preparation*. *Molecular & Cellular Proteomics*. 18:1027a-1035.

Bepler, T., A. Morin, M. Rapp, J. Brasch, L. Shapiro, A.J. Noble, and B. Berger. 2019. Positive-unlabeled convolutional neural networks for particle picking in cryo-electron micrographs. *Nature Methods*. 16:1153-1160.

Buvelot, S.P., S.Y. Tatsutani, D. Vermaak, and S. Biggins. 2003. The budding yeast Ipl1/Aurora protein kinase regulates mitotic spindle disassembly. *The Journal of Cell Biology*. 160:329-339.

Campbell, C.S., and A. Desai. 2013. Tension sensing by Aurora B kinase is independent of survivin-based centromere localization. *Nature*. 497:118-121.

Chambers, M.C., B. Maclean, R. Burke, D. Amodei, D.L. Ruderman, S. Neumann, L. Gatto, B. Fischer, B. Pratt, J. Egertson, K. Hoff, D. Kessner, N. Tasman, N. Shulman, B. Frewen, T.A. Baker, M.-Y. Brusniak, C. Paulse, D. Creasy, L. Flashner, K. Kani, C. Moulding, S.L. Seymour, L.M. Nuwaysir, B. Lefebvre, F. Kuhlmann, J. Roark, P. Rainer, S. Detlev, T. Hemenway, A. Huhmer, J. Langridge, B. Connolly, T. Chadick, K. Holly, J. Eckels, E.W. Deutsch, R.L. Moritz, J.E. Katz, D.B. Agus, M. Maccoss, D.L. Tabb, and P. Mallick. 2012. A cross-platform toolkit for mass spectrometry and proteomics. *Nature Biotechnology*. 30:918-920.

Cheeseman, I.M., J.S. Chappie, E.M. Wilson-Kubalek, and A. Desai. 2006. The Conserved KMN Network Constitutes the Core Microtubule-Binding Site of the Kinetochore. *Cell*. 127:983-997.

Cieslinski, K., Y.-L. Wu, L. Nechyporenko, S.J. Hörner, D. Conti, M. Skruzny, and J. Ries. 2023. Nanoscale structural organization and stoichiometry of the budding yeast kinetochore. *Journal of Cell Biology*. 222.

Ciferri, C., J. De Luca, S. Monzani, K.J. Ferrari, D. Ristic, C. Wyman, H. Stark, J. Kilmartin, E.D. Salmon, and A. Musacchio. 2005. Architecture of the Human Ndc80-Hec1

Complex, a Critical Constituent of the Outer Kinetochore. *Journal of Biological Chemistry*. 280:29088-29095.

Ciferri, C., S. Pasqualato, E. Screpanti, G. Varetti, S. Santaguida, G. Dos Reis, A. Maiolica, J. Polka, J.G. De Luca, P. De Wulf, M. Salek, J. Rappsilber, C.A. Moores, E.D. Salmon, and A. Musacchio. 2008. Implications for Kinetochore-Microtubule Attachment from the Structure of an Engineered Ndc80 Complex. *Cell*. 133:427-439.

Clarke, L., and J. Carbon. 1980. Isolation of a yeast centromere and construction of functional small circular chromosomes. *Nature*. 287:504-509.

Clarke, L., and J. Carbon. 1983. Genomic substitutions of centromeres in Saccharomyces cerevisiae. *Nature*. 305:23-28.

Combe, C.W., M. Graham, L. Kolbowski, L. Fischer, and J. Rappsilber. 2024. xiVIEW: Visualisation of Crosslinking Mass Spectrometry Data. *Journal of Molecular Biology*. 436:168656.

Croll, T.I. 2018. *ISOLDE*: a physically realistic environment for model building into low-resolution electron-density maps. *Acta Crystallographica Section D Structural Biology*. 74:519-530.

Deluca, J.G., W.E. Gall, C. Ciferri, D. Cimini, A. Musacchio, and E.D. Salmon. 2006. Kinetochore Microtubule Dynamics and Attachment Stability Are Regulated by Hec1. *Cell*. 127:969-982.

Dendooven, T., Z. Zhang, J. Yang, S.H. McLaughlin, J. Schwab, S.H.W. Scheres, S. Yatskevich, and D. Barford. 2023. Cryo-EM structure of the complete inner kinetochore of the budding yeast point centromere. *Science Advances*. 9.

Dhatchinamoorthy, K., M. Shivaraju, J.J. Lange, B. Rubinstein, J.R. Unruh, B.D. Slaughter, and J.L. Gerton. 2017. Structural plasticity of the living kinetochore. *Journal of Cell Biology*. 216:3551-3570.

Dimitrova, Y.N., S. Jenni, R. Valverde, Y. Khin, and S.C. Harrison. 2016. Structure of the MIND Complex Defines a Regulatory Focus for Yeast Kinetochore Assembly. *Cell*. 167:1014-1027.e1012.

Dudziak, A., J. Schmidt, F. Hamm, S. Tendulkar, K. Jänen, I.R. Vetter, S. Singh, J. Fischböck, F. Herzog, and S. Westermann. 2024. The Spc105^{Knl1}/Kre28^{Zwint} complex promotes mitotic error correction by outer kinetochore recruitment of the Ipl1$^{Aurora\ B}$ kinase. EMBO J. 2025 Apr 25. doi: 10.1038/s44318-025-00437-w. Online ahead of print.

Edgerton, H.D., S. Mukherjee, M. Johansson, J. Bachant, M.K. Gardner, and D.J. Clarke. 2023. Low tension recruits the yeast Aurora B protein Ipl1 to centromeres in metaphase. *Journal of Cell Science*. 136.

Emanuele, M.J., W. Lan, M. Jwa, S.A. Miller, C.S.M. Chan, and P.T. Stukenberg. 2008. Aurora B kinase and protein phosphatase 1 have opposing roles in modulating kinetochore assembly. *The Journal of Cell Biology*. 181:241-254.

Emsley, P., B. Lohkamp, W.G. Scott, and K. Cowtan. 2010. Features and development of *Coot*. *Acta Crystallographica Section D Biological Crystallography*. 66:486-501.

Euskirchen, G.M. 2002. Nnf1p, Dsn1p, Mtw1p, and Nsl1p: a New Group of Proteins Important for Chromosome Segregation in *Saccharomyces cerevisiae*. *Eukaryotic Cell*. 1:229-240.

Fischböck-Halwachs, J., S. Singh, M. Potocnjak, G. Hagemann, V. Solis-Mezarino, S. Woike, M. Ghodgaonkar-Steger, F. Weissmann, L.D. Gallego, J. Rojas, J. Andreani, A. Köhler, and F. Herzog. 2019. The COMA complex interacts with Cse4 and positions Sli15/Ipl1 at the budding yeast inner kinetochore. *eLife*. 8.

Fischer, E.S. 2023. Kinetochore-catalyzed MCC formation: A structural perspective. *IUBMB Life*. 75:289-310.

Fitzgerald-Hayes, M., L. Clarke, and J. Carbon. 1982. Nucleotide sequence comparisons and functional analysis of yeast centromere DNAs. *Cell*. 29:235-244.

Frigola, J., D. Remus, A. Mehanna, and J.F.X. Diffley. 2013. ATPase-dependent quality control of DNA replication origin licensing. *Nature*. 495:339-343.

García-Rodríguez, L.J., T. Kasciukovic, V. Denninger, and T.U. Tanaka. 2019. Aurora B-INCENP Localization at Centromeres/Inner Kinetochores Is Required for Chromosome Bi-orientation in Budding Yeast. *Current Biology*. 29:1536-1544.e1534.

Ghodgaonkar-Steger, M., M. Potocnjak, T. Zimniak, J. Fischböck-Halwachs, V. Solis-Mezarino, S. Singh, T. Speljko, G. Hagemann, D.J. Drexler, G. Witte, and F. Herzog. 2020. C-Terminal Motifs of the MTW1 Complex Cooperatively Stabilize Outer Kinetochore Assembly in Budding Yeast. *Cell Reports*. 32:108190.

Gietz, R.D., and R.H. Schiestl. 2007. High-efficiency yeast transformation using the LiAc/SS carrier DNA/PEG method. *Nature Protocols*. 2:31-34.

Goddard, T.D., C.C. Huang, E.C. Meng, E.F. Pettersen, G.S. Couch, J.H. Morris, and T.E. Ferrin. 2018. UCSF ChimeraX: Meeting modern challenges in visualization and analysis. *Protein Science*. 27:14-25.

Helgeson, L.A., A. Zelter, M. Riffle, M.J. Maccoss, C.L. Asbury, and T.N. Davis. 2018. Human Ska complex and Ndc80 complex interact to form a load-bearing assembly that strengthens kinetochore–microtubule attachments. *Proceedings of the National Academy of Sciences*. 115:2740-2745.

Hornung, P., M. Maier, G.M. Alushin, G.C. Lander, E. Nogales, and S. Westermann. 2011. Molecular Architecture and Connectivity of the Budding Yeast Mtw1 Kinetochore Complex. *Journal of Molecular Biology*. 405:548-559.

Hornung, P., P. Troc, F. Malvezzi, M. Maier, Z. Demianova, T. Zimniak, G. Litos, F. Lampert, A. Schleiffer, M. Brunner, K. Mechtler, F. Herzog, T.C. Marlovits, and S. Westermann. 2014. A cooperative mechanism drives budding yeast kinetochore assembly downstream of CENP-A. *Journal of Cell Biology*. 206:509-524.

Hughes, C.S., S. Moggridge, T. Müller, P.H. Sorensen, G.B. Morin, and J. Krijgsveld. 2019. Single-pot, solid-phase-enhanced sample preparation for proteomics experiments. *Nature Protocols*. 14:68-85.

Huis In 'T Veld, P.J., S. Jeganathan, A. Petrovic, P. Singh, J. John, V. Krenn, F. Weissmann, T. Bange, and A. Musacchio. 2016. Molecular basis of outer kinetochore assembly on CENP-T. *eLife*. 5.

Huis In 'T Veld, P.J., V.A. Volkov, I.D. Stender, A. Musacchio, and M. Dogterom. 2019. Molecular determinants of the Ska-Ndc80 interaction and their influence on microtubule tracking and force-coupling. *eLife*. 8.

Hyman, A.A., and P.K. Sorger. 1995. Structure and Function of Kinetochores in Budding Yeast. *Annual Review of Cell and Developmental Biology*. 11:471-495.

Joglekar, A.P., D.C. Bouck, J.N. Molk, K.S. Bloom, and E.D. Salmon. 2006. Molecular architecture of a kinetochore–microtubule attachment site. *Nature Cell Biology*. 8:581-585.

Johnston, K., A. Joglekar, T. Hori, A. Suzuki, T. Fukagawa, and E.D. Salmon. 2010. Vertebrate kinetochore protein architecture: protein copy number. *Journal of Cell Biology*. 189:937-943.

Jumper, J., R. Evans, A. Pritzel, T. Green, M. Figurnov, O. Ronneberger, K. Tunyasuvunakool, R. Bates, A. Žídek, A. Potapenko, A. Bridgland, C. Meyer, S.A.A. Kohl, A.J. Ballard, A. Cowie, B. Romera-Paredes, S. Nikolov, R. Jain, J. Adler, T. Back, S. Petersen, D. Reiman, E. Clancy, M. Zielinski, M. Steinegger, M. Pacholska, T. Berghammer, S. Bodenstein, D. Silver, O. Vinyals, A.W. Senior, K. Kavukcuoglu,

P. Kohli, and D. Hassabis. 2021. Highly accurate protein structure prediction with AlphaFold. *Nature*. 596:583-589.

Kastner, B., N. Fischer, M.M. Golas, B. Sander, P. Dube, D. Boehringer, K. Hartmuth, J. Deckert, F. Hauer, E. Wolf, H. Uchtenhagen, H. Urlaub, F. Herzog, J.M. Peters, D. Poerschke, R. Luhrmann, and H. Stark. 2008. GraFix: sample preparation for single-particle electron cryomicroscopy. *Nat Methods*. 5:53–55.

Kato, H., J. Jiang, B.-R. Zhou, M. Rozendaal, H. Feng, R. Ghirlando, T.S. Xiao, A.F. Straight, and Y. Bai. 2013. A Conserved Mechanism for Centromeric Nucleosome Recognition by Centromere Protein CENP-C. *Science*. 340:1110-1113.

Kern, D.M., J.K. Monda, K.-C. Su, E.M. Wilson-Kubalek, and I.M. Cheeseman. 2017. Astrin-SKAP complex reconstitution reveals its kinetochore interaction with microtubule-bound Ndc80. *eLife*. 6.

Killinger, K., M. Böhm, P. Steinbach, G. Hagemann, M. Blüggel, K. Jänen, S. Hohoff, P. Bayer, F. Herzog, and S. Westermann. 2020. Auto-inhibition of Mif2/CENP-C ensures centromere-dependent kinetochore assembly in budding yeast. *The EMBO Journal*. 39.

Kim, S., and H. Yu. 2015. Multiple assembly mechanisms anchor the KMN spindle checkpoint platform at human mitotic kinetochores. *Journal of Cell Biology*. 208:181-196.

Kimanius, D., L. Dong, G. Sharov, T. Nakane, and S.H.W. Scheres. 2021. New tools for automated cryo-EM single-particle analysis in RELION-4.0. *Biochemical Journal*. 478:4169-4185.

Kimanius, D., K. Jamali, M.E. Wilkinson, S. Lövestam, V. Velazhahan, T. Nakane, and S.H.W. Scheres. 2024. Data-driven regularization lowers the size barrier of cryo-EM structure determination. *Nature Methods*. 21:1216-1221.

Kitamura, E., K. Tanaka, Y. Kitamura, and T.U. Tanaka. 2007. Kinetochore–microtubule interaction during S phase in *Saccharomyces cerevisiae*. *Genes & Development*. 21:3319-3330.

Kiyomitsu, T., C. Obuse, and M. Yanagida. 2007. Human Blinkin/AF15q14 Is Required for Chromosome Alignment and the Mitotic Checkpoint through Direct Interaction with Bub1 and BubR1. *Developmental Cell*. 13:663-676.

Lampert, F., P. Hornung, and S. Westermann. 2010. The Dam1 complex confers microtubule plus end–tracking activity to the Ndc80 kinetochore complex. *Journal of Cell Biology*. 189:641-649.

Lampert, F., C. Mieck, G.M. Alushin, E. Nogales, and S. Westermann. 2013. Molecular requirements for the formation of a kinetochore–microtubule interface by Dam1 and Ndc80 complexes. *Journal of Cell Biology*. 200:21-30.

Lang, J., A. Barber, and S. Biggins. 2018. An assay for de novo kinetochore assembly reveals a key role for the CENP-T pathway in budding yeast. *eLife*. 7.

Lanz, M.C., K. Yugandhar, S. Gupta, E.J. Sanford, V.M. Faca, S. Vega, A.M.N. Joiner, J.C. Fromme, H. Yu, and M.B. Smolka. 2021. In-depth and 3-dimensional exploration of the budding yeast phosphoproteome. *EMBO reports*. 22:e51121.

Li, S., L.J. Garcia-Rodriguez, and T.U. Tanaka. 2023. Chromosome biorientation requires Aurora B's spatial separation from its outer kinetochore substrates, but not its turnover at kinetochores. *Current Biology*. 33:4557-4569.e4553.

Li, Y., J. Bachant, A.A. Alcasabas, Y. Wang, J. Qin, and S.J. Elledge. 2002. The mitotic spindle is required for loading of the DASH complex onto the kinetochore. *Genes & Development*. 16:183-197.

Liebschner, D., P.V. Afonine, M.L. Baker, G. Bunkóczi, V.B. Chen, T.I. Croll, B. Hintze, L.-W. Hung, S. Jain, A.J. McCoy, N.W. Moriarty, R.D. Oeffner, B.K. Poon, M.G. Prisant, R.J. Read, J.S. Richardson, D.C. Richardson, M.D. Sammito, O.V. Sobolev, D.H. Stockwell, T.C. Terwilliger, A.G. Urzhumtsev, L.L. Videau, C.J. Williams, and P.D. Adams. 2019. Macromolecular structure determination using X-rays, neutrons and electrons: recent developments in *Phenix*. *Acta Crystallographica Section D Structural Biology*. 75:861-877.

Malvezzi, F., G. Litos, A. Schleiffer, A. Heuck, K. Mechtler, T. Clausen, and S. Westermann. 2013. A structural basis for kinetochore recruitment of the Ndc80 complex via two distinct centromere receptors. *The EMBO Journal*. 32:409-423.

Maskell, D.P., X.-W. Hu, and M.R. Singleton. 2010. Molecular architecture and assembly of the yeast kinetochore MIND complex. *Journal of Cell Biology*. 190:823-834.

McAinsh, A.D., and G.J.P.L. Kops. 2023. Principles and dynamics of spindle assembly checkpoint signalling. *Nature Reviews Molecular Cell Biology*. 24:543-559.

McAinsh, A.D., and A.L. Marston. 2022. The Four Causes: The Functional Architecture of Centromeres and Kinetochores. *Annual Review of Genetics*. 56:279-314.

Mendes, M.L., L. Fischer, Z.A. Chen, M. Barbon, F.J. O'Reilly, S.H. Giese, M. Bohlke-Schneider, A. Belsom, T. Dau, C.W. Combe, M. Graham, M.R. Eisele, W. Baumeister, C. Speck, and J. Rappsilber. 2019. An integrated workflow for crosslinking mass spectrometry. *Molecular Systems Biology*. 15.

Mirdita, M., K. Schütze, Y. Moriwaki, L. Heo, S. Ovchinnikov, and M. Steinegger. 2022. ColabFold: making protein folding accessible to all. *Nature Methods*. 19:679-682.

Muir, K.W., C. Batters, T. Dendooven, J. Yang, Z. Zhang, A. Burt, and D. Barford. 2023. Structural mechanism of outer kinetochore Dam1-Ndc80 complex assembly on microtubules. *Science*. 382:1184-1190.

Musacchio, A., and A. Desai. 2017. A Molecular View of Kinetochore Assembly and Function. *Biology*. 6:5.

Nekrasov, V.S., M.A. Smith, S. Peak-Chew, and J.V. Kilmartin. 2003. Interactions between Centromere Complexes in *Saccharomyces cerevisiae*. *Molecular Biology of the Cell*. 14:4931-4946.

Nerusheva, O.O., S. Galander, J. Fernius, D. Kelly, and A.L. Marston. 2014. Tension-dependent removal of pericentromeric shugoshin is an indicator of sister chromosome biorientation. *Genes & Development*. 28:1291-1309.

Nishino, T., F. Rago, T. Hori, K. Tomii, I.M. Cheeseman, and T. Fukagawa. 2013. CENP-T provides a structural platform for outer kinetochore assembly. *The EMBO Journal*. 32:424-436.

Pagliuca, C., V.M. Draviam, E. Marco, P.K. Sorger, and P. De Wulf. 2009. Roles for the Conserved Spc105p/Kre28p Complex in Kinetochore-Microtubule Binding and the Spindle Assembly Checkpoint. *PLoS ONE*. 4:e7640.

Parnell, E.J., E.E. Jenson, and M.P. Miller. 2024. A conserved site on Ndc80 complex facilitates dynamic recruitment of Mps1 to yeast kinetochores to promote accurate chromosome segregation. *Current Biology*. 34:2294-2307.e2294.

Perez-Riverol Y, Bandla C, Kundu DJ, Kamatchinathan S, Bai J, Hewapathirana S, John NS, Prakash A, Walzer M, Wang S, Vizcaíno JA. 2025. The PRIDE database at 20 years: 2025 update. Nucleic Acids Res. 53(D1):D543-D553. doi: 10.1093/nar/gkae1011

Petrovic, A., J. Keller, Y. Liu, K. Overlack, J. John, Y.N. Dimitrova, S. Jenni, S. Van Gerwen, P. Stege, S. Wohlgemuth, P. Rombaut, F. Herzog, S.C. Harrison, I.R. Vetter, and A. Musacchio. 2016. Structure of the MIS12 Complex and Molecular Basis of Its Interaction with CENP-C at Human Kinetochores. *Cell*. 167:1028-1040.e1015.

Petrovic, A., S. Mosalaganti, J. Keller, M. Mattiuzzo, K. Overlack, V. Krenn, Anna, S. Wohlgemuth, V. Cecatiello, S. Pasqualato, S. Raunser, and A. Musacchio. 2014. Modular Assembly of RWD Domains on the Mis12 Complex Underlies Outer Kinetochore Organization. *Molecular Cell*. 53:591-605.

Petrovic, A., S. Pasqualato, P. Dube, V. Krenn, S. Santaguida, D. Cittaro, S. Monzani, L. Massimiliano, J. Keller, A. Tarricone, A. Maiolica, H. Stark, and A. Musacchio. 2010. The MIS12 complex is a protein interaction hub for outer kinetochore assembly. *Journal of Cell Biology*. 190:835-852.

Pettersen, E.F., T.D. Goddard, C.C. Huang, E.C. Meng, G.S. Couch, T.I. Croll, J.H. Morris, and T.E. Ferrin. 2021. UCSF ChimeraX: Structure visualization for researchers, educators, and developers. *Protein Science*. 30:70-82.

Pleuger, R., C. Cozma, S. Hohoff, C. Denkhaus, A. Dudziak, F. Kaschani, M. Kaiser, A. Musacchio, I.R. Vetter, and S. Westermann. 2024. Microtubule end-on attachment maturation regulates Mps1 association with its kinetochore receptor. *Current Biology*. 34:2279-2293.e2276.

Polley, S., T. Raisch, S. Ghetti, M. Körner, M. Terbeck, F. Gräter, S. Raunser, C. Aponte-Santamaría, I.R. Vetter, and A. Musacchio. 2024. Structure of the human KMN complex and implications for regulation of its assembly. *Nature Structural & Molecular Biology*. 31:861-873.

Przewloka, M.R., Z. Venkei, V.M. Bolanos-Garcia, J. Debski, M. Dadlez, and D.M. Glover. 2011. CENP-C Is a Structural Platform for Kinetochore Assembly. *Current Biology*. 21:399-405.

Punjani, A., J.L. Rubinstein, D.J. Fleet, and M.A. Brubaker. 2017. cryoSPARC: algorithms for rapid unsupervised cryo-EM structure determination. *Nature Methods*. 14:290-296.

Rago, F., K.E. Gascoigne, and I.M. Cheeseman. 2015. Distinct Organization and Regulation of the Outer Kinetochore KMN Network Downstream of CENP-C and CENP-T. *Current Biology*. 25:671-677.

Rieder, C.L., R.W. Cole, A. Khodjakov, and G. Sluder. 1995. The checkpoint delaying anaphase in response to chromosome monoorientation is mediated by an inhibitory signal produced by unattached kinetochores. *The Journal of Cell Biology*. 130:941-948.

Rohou, A., and N. Grigorieff. 2015. CTFFIND4: Fast and accurate defocus estimation from electron micrographs. *Journal of Structural Biology*. 192:216-221.

Roy, B., J. Sim, S.J.Y. Han, and A.P. Joglekar. 2022. Kre28–Spc105 interaction is essential for Spc105 loading at the kinetochore. *Open Biology*. 12.

Scarborough, E.A., T.N. Davis, and C.L. Asbury. 2019. Tight bending of the Ndc80 complex provides intrinsic regulation of its binding to microtubules. *eLife*. 8.

Schmitzberger, F., M.M. Richter, Y. Gordiyenko, C.V. Robinson, M. Dadlez, and S. Westermann. 2017. Molecular basis for inner kinetochore configuration through RWD domain-peptide interactions. *The EMBO journal*. 36:3458–3482.

Screpanti, E., A. De Antoni, G.M. Alushin, A. Petrovic, T. Melis, E. Nogales, and A. Musacchio. 2011. Direct Binding of Cenp-C to the Mis12 Complex Joins the Inner and Outer Kinetochore. *Current Biology*. 21:391-398.

Shimogawa, M.M., P.O. Widlund, M. Riffle, M. Ess, and T.N. Davis. 2009. Bir1 Is Required for the Tension Checkpoint. *Molecular Biology of the Cell*. 20:915-923.

Sievers, F., A. Wilm, D. Dineen, T.J. Gibson, K. Karplus, W. Li, R. Lopez, H. McWilliam, M. Remmert, J. Söding, J.D. Thompson, and D.G. Higgins. 2011. Fast, scalable

generation of high-quality protein multiple sequence alignments using Clustal Omega. *Molecular Systems Biology*. 7:539.

Stark, H. 2010. GraFix: Stabilization of Fragile Macromolecular Complexes for Single Particle Cryo-EM. *Methods in Enzymology*. 481:109-126.

Takenoshita, Y., M. Hara, R. Nakagawa, M. Ariyoshi, and T. Fukagawa. 2024. Molecular details and phosphoregulation of the CENP-T-Mis12 complex interaction during mitosis in DT40 cells. *iScience*. 27:111295.

Tanaka, K., E. Kitamura, Y. Kitamura, and T.U. Tanaka. 2007. Molecular mechanisms of microtubule-dependent kinetochore transport toward spindle poles. *The Journal of Cell Biology*. 178:269-281.

Tanaka, K., N. Mukae, H. Dewar, M. Van Breugel, E.K. James, A.R. Prescott, C. Antony, and T.U. Tanaka. 2005. Molecular mechanisms of kinetochore capture by spindle microtubules. *Nature*. 434:987-994.

Tanaka, S., M. Miyazawa-Onami, T. Iida, and H. Araki. 2015. iAID: an improved auxin-inducible degron system for the construction of a 'tight' conditional mutant in the budding yeast *Saccharomyces cerevisiae*. *Yeast*. 32:567-581.

Tien, J.F., N.T. Umbreit, D.R. Gestaut, A.D. Franck, J. Cooper, L. Wordeman, T. Gonen, C.L. Asbury, and T.N. Davis. 2010. Cooperation of the Dam1 and Ndc80 kinetochore complexes enhances microtubule coupling and is regulated by aurora B. *Journal of Cell Biology*. 189:713-723.

Tromer, E.C., J.J.E. Van Hooff, G.J.P.L. Kops, and B. Snel. 2019. Mosaic origin of the eukaryotic kinetochore. *Proceedings of the National Academy of Sciences*. 116:12873-12882.

Valverde, R., J. Ingram, and S.C. Harrison. 2016. Conserved Tetramer Junction in the Kinetochore Ndc80 Complex. *Cell Reports*. 17:1915-1922.

Van Hooff, J.J.E., B. Snel, and G.J.P.L. Kops. 2017. Unique Phylogenetic Distributions of the Ska and Dam1 Complexes Support Functional Analogy and Suggest Multiple Parallel Displacements of Ska by Dam1. *Genome Biology and Evolution*. 9:1295-1303.

Walstein, K., A. Petrovic, D. Pan, B. Hagemeier, D. Vogt, I.R. Vetter, and A. Musacchio. 2021. Assembly principles and stoichiometry of a complete human kinetochore module. *Science Advances*. 7:eabg1037.

Wang, H.-W., S. Long, C. Ciferri, S. Westermann, D. Drubin, G. Barnes, and E. Nogales. 2008. Architecture and Flexibility of the Yeast Ndc80 Kinetochore Complex. *Journal of Molecular Biology*. 383:894-903.

Waterhouse, A.M., J.B. Procter, D.M.A. Martin, M. Clamp, and G.J. Barton. 2009. Jalview Version 2—a multiple sequence alignment editor and analysis workbench. *Bioinformatics*. 25:1189-1191.

Wei, R.R., J. Al-Bassam, and S.C. Harrison. 2007. The Ndc80/HEC1 complex is a contact point for kinetochore-microtubule attachment. *Nature Structural & Molecular Biology*. 14:54-59.

Wei, R.R., J.R. Schnell, N.A. Larsen, P.K. Sorger, J.J. Chou, and S.C. Harrison. 2006. Structure of a Central Component of the Yeast Kinetochore: The Spc24p/Spc25p Globular Domain. *Structure*. 14:1003-1009.

Wei, R.R., P.K. Sorger, and S.C. Harrison. 2005. Molecular organization of the Ndc80 complex, an essential kinetochore component. *Proceedings of the National Academy of Sciences*. 102:5363-5367.

Wells, W.A., and A.W. Murray. 1996. Aberrantly segregating centromeres activate the spindle assembly checkpoint in budding yeast. *The Journal of Cell Biology*. 133:75-84.

Westermann, S., I.M. Cheeseman, S. Anderson, J.R. Yates, D.G. Drubin, and G. Barnes. 2003. Architecture of the budding yeast kinetochore reveals a conserved molecular core. *The Journal of Cell Biology*. 163:215-222.

Wigge, P.A., O.N. Jensen, S. Holmes, S. Souès, M. Mann, and J.V. Kilmartin. 1998. Analysis of the *Saccharomyces* Spindle Pole by Matrix-assisted Laser Desorption/Ionization (MALDI) Mass Spectrometry. *The Journal of Cell Biology*. 141:967-977.

Xiao, H., F. Wang, J. Wisniewski, A.K. Shaytan, R. Ghirlando, P.C. Fitzgerald, Y. Huang, D. Wei, S. Li, D. Landsman, A.R. Panchenko, and C. Wu. 2017. Molecular basis of CENP-C association with the CENP-A nucleosome at yeast centromeres. *Genes & Development*. 31:1958-1972.

Yan, K., J. Yang, Z. Zhang, S.H. McLaughlin, L. Chang, D. Fasci, A.E. Ehrenhofer-Murray, A.J.R. Heck, and D. Barford. 2019. Structure of the inner kinetochore CCAN complex assembled onto a centromeric nucleosome. *Nature*. 574:278-282.

Yang, Y., F. Wu, T. Ward, F. Yan, Q. Wu, Z. Wang, T. McGlothen, W. Peng, T. You, M. Sun, T. Cui, R. Hu, Z. Dou, J. Zhu, W. Xie, Z. Rao, X. Ding, and X. Yao. 2008. Phosphorylation of HsMis13 by Aurora B Kinase Is Essential for Assembly of Functional Kinetochore. *Journal of Biological Chemistry*. 283:26726-26736.

Yatskevich, S., K.W. Muir, D. Bellini, Z. Zhang, J. Yang, T. Tischer, M. Predin, T. Dendooven, S.H. McLaughlin, and D. Barford. 2022. Structure of the human inner kinetochore bound to a centromeric CENP-A nucleosome. *Science*. 376:844-852.

Yatskevich, S., J. Yang, D. Bellini, Z. Zhang, and D. Barford. 2024. Structure of the human outer kinetochore KMN network complex. *Nature Structural & Molecular Biology*. 31:874-883.

Zahm, J.A., and S.C. Harrison. 2024. A communication hub for phosphoregulation of kinetochore-microtubule attachment. *Current Biology*. 34:2308-2318.e2306.

Zhang, Z., J. Yang, and D. Barford. 2016. Recombinant expression and reconstitution of multiprotein complexes by the USER cloning method in the insect cell-baculovirus expression system. *Methods*. 95:13-25.

Zheng, S.Q., E. Palovcak, J.-P. Armache, K.A. Verba, Y. Cheng, and D.A. Agard. 2017. MotionCor2: anisotropic correction of beam-induced motion for improved cryo-electron microscopy. *Nature Methods*. 14:331-332.